The physics of heart rhythm disorders

Wouter-Jan Rappel

Department of Physics, University of California San Diego, La Jolla, CA 92037

Abstract

The global burden caused by cardiovascular disease is substantial, with heart disease representing the most common cause of death around the world. There remains a need to develop better mechanistic models of cardiac function in order to combat this health concern. Heart rhythm disorders, or arrhythmias, are one particular type of disease which has been amenable to quantitative investigation. Here we review the application of quantitative methodologies to explore dynamical questions pertaining to arrhythmias. We begin by describing single-cell models of cardiac myocytes, from which two and three dimensional models can be constructed. Special focus is placed on results relating to pattern formation across these spatially-distributed systems, especially the formation of spiral waves of activation. Next, we discuss mechanisms which can lead to the initiation of arrhythmias, focusing on the dynamical state of spatially discordant alternans, and outline proposed mechanisms perpetuating arrhythmias such as fibrillation. We then review experimental and clinical results related to the spatio-temporal mapping of heart rhythm disorders. Finally, we describe treatment options for heart rhythm disorders and demonstrate how statistical physics tools can provide insights into the dynamics of heart rhythm disorders.

Keywords

Heart rhythm disorders; Arrhythmias; Fibrillation; Modeling

1. Introduction

What is the heart? The heart has historically been thought of as the central and most important organ in the human body. The Greek philosopher Aristotle, for example, believed that the heart was the source of heat for the body and was therefore also responsible for the "sensory soul": the part of our soul that allows us to understand the world around us. This cardiocentric view is also evident from the numerous idioms and expressions in which the heart plays a central role. After all, one gets to the heart of the matter, has a heart of gold, and can have a broken heart. Over time, of course, this historic view of the heart has changed and its main function, essential to the survival of an individual, has become clear: to circulate oxygenated blood throughout the body. To accomplish this, it has to contract in a period fashion, roughly once per second. This rhythm can, of course, be modulated by exercise or stress but assuming this rate, the heart will have contracted approximately 2×10^9 times (!) once a person has reached 80 years of age.

As with other organs in the body, problems can arise. In fact, heart disease is the leading cause of death, not only in high-income countries such as the United States [1], but also

globally, accounting for 16% of the worlds total deaths [2]. There are several types of heart disease, with coronary heart disease being the most common one. During coronary heart disease, the arteries of the heart cannot deliver enough oxygen-rich blood to the heart muscle, resulting in the death of the muscle and a heart attack. It is estimated that in the United States alone, a heart attack (or myocardial infarction) occurs approximately every 40 seconds [3].

A different type of heart disease, and the focus of this review, involves the malfunctioning of the heart's electrical system, resulting in irregular contractions. These irregularities, called arrhythmias or rhythm disorders, can have severe consequences. Ventricular fibrillation, for example, during which the electrical activity of the large chambers of the heart is incoherent, will result in sudden cardiac death unless prompt medical attention is nearby. Up to 300,000 people die from sudden cardiac arrest each year in the United States [4]. Its counterpart in the small chambers, atrial fibrillation, is not acutely lethal but leads to an increase in stroke, heart failure and mortality rates and currently affects more than 5 million people in the United States.

For a physicist or a modeler, the heart is a complex, excitable, coupled, nonlinear, spatially extended, electro-mechanical object that lends itself to quantitative modeling and analysis. In fact, the heart has been the subject of numerous modeling efforts that address both the electrical and the mechanical aspects of its workings and can been argued to be the most modeled physiological system. These efforts have rapidly increased in complexity and scale from single cell models to models that incorporate patient-specific geometries. Importantly, these models have resulted in significant new insights into the initiation and maintenance of cardiac arrhythmias, which, in turn, have resulted in novel therapeutic approaches.

In this review, we will focus on the heart from a modelers perspective, touching on most of the aforementioned adjectives used to describe the heart. Furthermore, we will emphasize cardiac arrhythmias, since these rhythm disorders have a large impact on public health. Where possible, we will attempt to make connections with experimental and clinical work, showing how insights from mathematical and physical studies can result in a better understanding of these arrhythmias and may guide the search for treatment options.

This review is organized as follows: We will begin by briefly describing the basic anatomy of the heart, followed by an overview of the most common and most dangerous cardiac arrhythmias. We will then describe in some detail the electrophysiology of single cells and of strands and sheets of tissue. We will review how the properties of cardiac cells can be cast into mathematical equations and will describe how one can simulate these equations. We will then focus on the initiation of arrhythmias and detail the role of spiral waves in arrhythmias. Next, we will discuss experimental and clinical observations of arrhythmias, followed by an overview of currently available treatments of cardiac arrhythmias. We will conclude with an outlook, in which we discuss possible new avenues for research.

2. Anatomy and electrophysiology of the heart

In this section, we will describe the basic anatomy of the heart and the electrophysiological function of heart cells. We will start with a single cell and describe how ion channels and exchanges regulate the membrane potential and will discuss how a 1D cable of heart cells is able to propagate a cardiac activation front. Finally, we will discuss how cells withing 2D and 3D tissues are coupled together and will describe the electrophysiology within human atria and ventricles. This overview is brief, as a large number of excellent reviews and textbooks are available to the interested reader (e.g., [5, 6, 7]).

2.1. Basic anatomy and activation sequence

The anatomy of the heart is schematically shown in Fig. 1A and is described in great detail in numerous textbooks (see, e.g., [5]). Briefly, it consists of two small chambers, the atria, and two larger ones, the ventricles. The walls of these chambers are comprised of different cells, including cardiac myocytes, a special type of muscle cells that allow these chambers to contract and pump blood. The blood flow in the body is described in detail in the literature and will not be the focus of this review [8]. Suffices to say that deoxygenated blood flows from the body to the right atrium (RA; commonly used abbreviations are listed in Table 1), after which it is pumped into the right ventricle (RV). Contraction of this ventricle pumps the blood to the lungs where it is oxygenated and, subsequently, returned to the left atrium, which transports it to the left ventricle. Left ventricle contraction allows this oxygen-rich blood to flow to the rest of the body. Finally, valves between the different chambers ensures unidirectional blood flow.

Clearly, the contraction of these chambers needs to be carefully orchestrated, as a disruption of the blood flow will result in inadequate oxygen supply to the body. This coordination is made possible by an electrical wave that coherently and periodically sweeps through the tissue of the heart and that, ultimately, results in cell contraction. During the resting phase of the heart, called diastole, cardiac cells are hyperpolarized, with a resting potential of around −85 mV. Just as muscle cells and neurons, however, myocytes can depolarize and, due to inter-cellular coupling, an electrical wave can propagate through the tissue.

This wave propagates through the electrical conduction system, schematically shown in Fig. 1B. It is initiated by a group of cells within the right atrium, called the sino-atrial node [9], which shows oscillatory behavior and spontaneously depolarize in a periodic fashion. This group of cells regulates the frequency of one's heartbeat, which is a function of the person's physical and mental state: physical exercise, fear, nervousness, and other conditions all lead to an increase in the frequency of sino-atrial firing while relaxation and calming exercises can lead to a decrease [10].

Once fired, the electrical activation propagates through the neighboring cells, made possible by the electrical coupling of the cells and the excitable nature of the cells, further explained in Section 2.2 [11]. This coupling is mediated by gap junctions, assemblies of channel proteins that allow rapid exchange of ions between cells [12]. The electrical wave sweeps through the right atrium and, immediately following that, the left atrium. The speed of propagation in normal atrial tissue is about 100 cm/s which, together with a typical size of

the atria, results in atrial depolarization within less than 90 ms. These useful numbers of the heart, along with others, are listed in Table 2. As a consequence of the cells depolarization, a large amount of calcium (Ca^{2+}) rushes into the cell. These calcium ions bind to troponin which, ultimately, leads to cell contraction [13].

The contraction of the atria is slightly earlier than the contraction of the ventricles, which ensures effective pumping of the blood from the small to the large chambers. This is possible since the electrical wave in the atria does not immediately propagate further into the ventricles. In fact, the atria are electrically isolated from the ventricles by a non-conducting barrier, except for a specialized region of cells called the atrioventricular (AV) node (see Fig. 1B). Conduction velocity within the AV node is only 5 cm/s, resulting in a delay of propagation. This delay results in complete atrial depolarization and contraction before the ventricles are activated. Following activation of the AV node, the electrical signal propagates through specialized sets of fibers (bundle of His and the Purkinje fibers) that run from the atria to the endocardial surface of the ventricles and conduct the activation from the atria with minimal time delay. The resulting ventricular depolarization starts at the inner surface and the base of the heart, followed by transmural and base-apex propagation with a conduction velocity around 50 cm/s. The entire heart mass is depolarized within approximately 250 ms, after which the cells slowly return to their resting potential.

2.2. Single cell anatomy and electrophysiology

A single cardiac myocyte is roughly cylindrical in shape, with a length of approximately 120 μm and a diameter of 25 μm. Ventricular cells contain transverse tubules, or T-tubules, narrow invaginations of the sarcolemma that occur at so-called Z-lines and are regularly spaced (~ 1.8μm) [18]. This striation can be clearly seen in the confocal micrograph of a human cardiac myocyte in Fig. 2A, where α-actinin, a protein that anchors actin filaments to the Z-lines, is labeled in green. Many of the proteins responsible for Ca^{2+} handling, and thus contraction, are concentrated within these tubules [13]. It is of note, however, that atrial cells do not have T-tubules [18]. Embedded with the membrane of the myocyte are a large number of ion channels, as schematically shown in Fig. 2B. These channels consist of specialized proteins that are selectively permeable to certain ions. For example, the potassium channel has a conductivity for K^+ that is much larger than for the similarly sized sodium ion Na^+. How this is achieved can be addressed by detailed molecular dynamics simulations, reviewed in [19]. The precise working of these channels have been reviewed before and we will only briefly describe their function [20, 21].

At rest, the membrane potential V of cardiac cells is roughly −85 mV, close to the Nernst potential for potassium. At this potential, the net flux of potassium ions is zero and the chemical and electrical forces are in balance [22]. Almost all cardiac cells are excitable. This means that when the membrane potential is raised above a critical value, the potential rapidly increases, followed by a gradual return to equilibrium. In other words, a small stimulus can result in a large response. As a consequence of this excitability, cardiac cells also exhibit a refractory period. That is to say, a cell cannot be excited again unless it has recovered sufficiently. In Section 4 we will see that this refractory period plays an important role in the initiation of arrhythmias. Of course, cardiac cells are not only the only excitable

cells in the human body. Neurons are also excitable and display a similar threshold and refractoriness. A significant difference between cardiac cells and neurons, however, is the APD. For neurons, this AP is of the order of 1 ms [23] while in cardiac cells the AP can take on values of 100-300 ms.

In cardiac cells, an increase in the potential results in the opening of sodium channels, which are controlled by the voltage, and sodium ions rush in (I_{Na} in Fig. 2C). As a result, the potential of the cell increases rapidly, leading to a large and fast upstroke. After several milliseconds, the potential reaches its maximum, after which it remains at a plateau for 50-200 ms during which the influx of calcium ions (blue curve in Fig. 2C) is electrically balanced by the efflux of potassium ions. Once the Ca^{2+} channels close, the potassium currents (I_K in Fig. 2C) return the potential back to its resting state. The ensuing dynamics of the voltage is called the action potential (AP) while the action potential duration (APD) is defined as the time spent by the cell above a certain percentage value of repolarization (often taken to be 90%).

As already mentioned, Ca^{2+} is essential in the coupling between electrical excitation and mechanical contraction, carried out by the motor protein myosin that pulls actin filaments in a ratcheted fashion [13]. Before depolarization, the intracellular (cytosolic) Ca^{2+} concentration is very low, only roughly 100 nM. As a result, the myosin binding site on actin is blocked, preventing contraction. During repolarization, the cytosolic Ca^{2+} concentration increases sharply, and Ca^{2+} binds to the regulatory protein troponin, which exposes the myosin binding site on actin [26]. The subsequent binding of myosin to actin, combined with the energy released from ATP hydrolysis, creates a power stroke, which provides the mechanical force required for muscle contraction [27].

The sharp increase in Ca^{2+} required for contraction is achieved through a positive feedback mechanism called Calcium Induced Calcium Release (CICR) [28]. During depolarization, calcium ions that move into the cell through the voltage gated L-type Ca^{2+} channels (LCCs) enter a small sub-cellular compartment called the dyadic cleft, which separates the membrane (containing the LCCs) and the sacroplasmic reticulum (SR). These SRs are membrane-bound structures that function as Ca^{2+} storage units. Calcium ions within the cleft then bind to and activate the cardiac ryanodine receptors (RyRs) that are embedded in the SR membrane (see Fig. 2B). This activation leads to a large influx of Ca^{2+} into the cytoplasm and a ~ 10-fold increase in cytosolic Ca^{2+} concentration [29, 30]. Also part of the SR are SERCAs, Ca^{2+} pumps that are responsible for removing calcium ions from the cytosol and returning them to the SR. Once the cell has sufficiently repolarized, the activation cycle can start again.

The regulation of the RyR receptor has been subject of intense research, reviewed in, e.g., [31, 32]. Malfunctioning of this receptor has been implicated in heart failure, the condition during which the heart muscle is progressively weakened and unable to pump blood through the body [33]. It has also been connected to the initiation of cardiac arrhythmias, including ventricular and atrial fibrillation. In this case, it is believed that the leakage of the RyR receptor can result in spontaneous depolarization events and aberrant electrical activation, as further discussed in Section 4 [34].

2.3. Cell-to-cell coupling, tissue, and fiber orientation

So far, we have examined the dynamics of a single cell. Let us now consider what happens if we connect cells and form a cable. Cardiac cells are electrically coupled end-to-end through gap junctions and the depolarization of one cell will result in the increase of the potential in its neighboring cells. If this increase is such that the potential exceeds the excitatory threshold, the neighboring cells will depolarize as well. For sufficiently strong coupling this process will be repeated with other cells, and a wave of excitation will travel through the cable. This type of dynamics is not just limited to cardiac cells, but is also present in other excitable systems, including strands of nerve cells.

In cardiac tissue, the length-axes of the cells are typically aligned along their length axis and form a branched network (Fig. 3A). This fiber alignment has important consequences of the propagation velocity in cardiac tissue since the electrical conductivity along the fiber direction (longitudinal) is faster than the conductivity across fibers (transverse direction) [35, 36]. This anisotropic conductivity is simply because the gap junctions, which facilitate ionic movement between cells, are primarily found at end-to-end locations. The ratio of the longitudinal and transverse velocities varies in the heart and is approximately 2.5-4 in ventricular muscle but can be around 10 in some parts of the atrium [37, 38].

The fiber orientation in cardiac tissue can be quite complex. In the ventricular wall, the myocardium displays a laminar structure with cells stacked in sheets of varying orientation that are parallel to the epicardium and endocardium [39, 40]. The fiber axis of the cells is approximately identical within each sheet and rotates continuously as one traverses the ventricular wall. The angle over which the fibers rotate has been measured in *ex vivo* human hearts using diffusion tensor magnetic resonance imaging (DTMRI). This technique uses the diffusion of water molecules to generate images of fiber orientation in tissue [41]. These studies revealed that the helical angle of the fibers rotate approximately 107 $^{\circ}$ [42] and example of the fiber orientation in a DTMRI study of the left ventricle is shown in Fig. 3B [43].

Furthermore, the fiber orientation was found to be relatively conserved across different individuals. The same DTMRI technique can also be used to determine the fiber orientation in the atria. Examples of this orientation in two atrial specimens are shown in Fig. 3C. In this panel, the color represents the distance to the endocardial shell, with fibers located closer to the epicardium shown in red and those closer to the endocardium shown in yellow. In contrast to the ventricles, the atria appear to show significant differences between subjects in the orientation and location of fiber bundles [44].

3. Modeling cardiac activity

Cardiac modeling, and particular describing the electrical properties of the heart, has a long history as reviewed by Henriquez [45]. The modeling of electrical properties started with formulations of cardiac ionic channels and focused on the excitable nature of single cells (see Sec. 2.2 for a definition of excitability). Once computational speeds increased, it became feasible to simulate multiple, coupled cells and to address propagating electrical signals. These simulations resulted in breakthrough insights into arrhythmias, specifically

with regard to the role of reentry and spiral waves (see Section 4). More recently, computational studies have increased in complexity and now include patient-specific models, using clinically derived atrial and ventricular geometries. In addition, increased computational speeds make it possible to develop models that describe the feedback between electrical and mechanical activity of the heart [46] and these models are now also employed in patient-specific geometries [47]. In this review, however, we will focus on the electrophysiological properties of cardiac tissue and we refer the reader interested in cardiac mechanics to a recent review on the history of mechanical modeling [48]. In this section, we will first give an overview of single cell models. We will then describe modeling the propagation of an electrical signal in a one-dimensional cable and will conclude with a discussion of models in spatially extended geometries.

3.1. Single cells

To cast the time-dependence of the membrane potential of a cardiac cell, V, in the form of mathematical equations, one can view the cell membrane as a capacitor, with capacitance C_m per unit area (μF cm^{-2}), in parallel with a resistor, representing ionic currents. Since there cannot be any net accumulation of charge on either side of the membrane, the sum of the current through the channels and the capacitive current needs to be zero:

$$C_m \frac{dV}{dt} + I_{ion} = 0 \tag{1}$$

Here, the last term describes all ionic currents ($\mu A\ cm^{-2}$) considered in the model and where, by convention, inward currents are negative and outward currents are positive. The dynamics of these currents can be described in terms of ordinary differential equations, as first shown by the seminal work of Hodgkin and Huxley [49]. They studied action potentials in the squid giant axon using voltage clamp experiments, which measured the dynamics of the ion channel conductances. This study revealed that the generic form of a current, say X, is:

$$I_X = g_X f(V, x_1, x_2, ..., x_N)(V - E_X) \tag{2}$$

where E_X is its reversal potential, g_X represents the conductance per area, and f is a function that depends on gating variables x_i, $i = 1, ..., N$. For example, the potassium current per unit area for the giant squid axon can be accurately described as $I_K = g_K n^4 (V - E_K)$, where n is a dimensionless gating variable, given by:

$$\frac{dn}{dt} = \alpha_n(V)(1 - n) - \beta_n(V)n, \tag{3}$$

In this expression, α_n and β_n are functions of V, chosen to match experimental results.

Ionic channels in myocytes (some of which are shown in Fig. 2A) can be described using Hodgkin-Huxley-like expressions. During the past decades, a large number of cardiac models that formulate these ion channels have been developed with ever increasing complexity and details (see, e.g., the review by Fenton and Cherry [50]). A major

contributor to this increase of complexity is the introduction of calcium dynamics, absent in earlier and simplified models. Models have been developed for both ventricular [51, 52, 53] and atrial cells [54, 55, 56] and have been used to give insights into cardiac electrical dynamics, including arrhythmias (see Section 4).

In certain cases, for example for specific mutations of certain channels, the Hodgkin-Huxley formalism may not be sufficiently detailed to describe the electrical properties of the cell. For these cases, it is possible to formulate a Markov-based description of the gating of the channel. In this description, the ion channel is represented by a number of discrete states, corresponding to different configurations of the channel and the model incorporates the transition rates between these states, which can be found using fitting techniques [57]. These Markov formulations have been used to determine how certain genetic defects may be linked to cardiac arrhythmias [58, 59]. Furthermore, this type of model can be used to give insights in the effects of drugs that target channels; we will see an example of this in Section 6 [60]. Several studies have discussed the merits of the Markov vs Hodgkin-Huxley formalism [61, 62].

There are a number of drawbacks to using very detailed models that attempt to incorporate all possible ion channels. First of all, the number of variables is very large, which can make simulations more time consuming and less intuitive. For example, a Markov-based model for the human epicardial ventricular myocyte contains 67 variables [52]. More fundamentally, however, it is challenging to accurately describe all ion channels operating in human cardiac cells. The equations that describe the identified channels are highly nonlinear with many poorly characterized parameters. Some of these channels are not measured in human cells and are, instead, fitted to data from animal cells. Furthermore, a human heart consists of many different cells with different properties and capturing this heterogeneity is challenging at best. Finally, in addition to this patient-specific heterogeneity, there exists considerable patient-to-patient variability. This is the case for healthy individuals but especially for individuals that are suffering from cardiac diseases. Thus, it seems an impossible task to construct a universal electrophysiological cell model.

An alternative approach to developing highly detailed models is to forgo the complexity inherent to the many ion channels and create a model that can replicate some of the essential features of a cardiac cell with only a few variables. Such models should, of course, be able to create realistic action potential, characterized by a fast upstroke (i.e., increase) of the voltage, followed by a gradual return to equilibrium. In other words, these models should have excitable or excitable-like dynamics such that a small stimulus will have a significantly different and smaller response that a larger stimulus. Furthermore, these models should be able to display some of the spatially extended dynamics thought to underlie cardiac arrhythmias (see Section 4). In particular, it should exhibit spiral wave dynamics, which we will discuss in more detail in the next sections. The advantage of these models is that they are much easier to implement, are faster to simulate, and can sometimes be more intuitive. Of course, the price one pays is that determining the role of specific channels is no longer possible. Nevertheless, it was through the use of such models that some of the critical insights into spatio-temporal organization during cardiac arrhythmias were gained [63, 64].

One of the simplest models one can write down for a cardiac cell is the FitzHugh-Nagumo (FHN) model [65, 66]. This model contains only two variables, one of which (v) can be thought of as the membrane potential while the other one (w) represents all currents of the cardiac cell and functions as the recovery variable:

$$\frac{dv}{dt} = f(v, w) \tag{4}$$

$$\frac{dw}{dt} = \epsilon g(v, w), \tag{5}$$

In these equations, the parameter ϵ is taken to be much less than 1, such that v is the fast, or excitation, variable and w is the slow recovery variable. Furthermore, f is typically taken as cubic function while g is a linear function. Although many different forms can be taken, a particular and convenient form corresponds to $f(v, w) = v - \frac{v^3}{3} - w$ and $g(v, w) = v + a - bw$ where a and b are parameters of the model [67].

For such a model, it is possible and instructive to draw a phase diagram in the (v, w) space along with the nullclines, defined as the curves on which $\dot{v} = \dot{w} = 0$. The intersection of these nullclines then gives the fixed point [68]. Depending on the parameters of the model, this fixed point is either stable or unstable. Fig. 4A shows the nullclines for the convenient choice of f and g and for parameters for which the fixed point, indicated by the yellow dot, is stable [69]. Transiently perturbing the variables away from this fixed point, for example by introducing a non-zero excitation current to either the v or w variable, results in dynamics that depends critically on the amplitude of the perturbation. A small perturbation will result in a small deviation, followed by a return to the fixed point. An example of the dynamics in the (v, w) space following such a perturbation is shown as the red trajectory labeled by 1 in Fig. 4A while the corresponding time trace is plotted in Fig. 4B. This is in sharp contrast to the dynamics following a larger perturbation, represented by the trajectory and timetrace labeled 2 in Fig. 4A&B. In this case, the perturbation results in a large excursion in phase space. Due to the small value of ϵ, the v variable rapidly switches from its perturbed value to the right-most branch of the v nullcline. Once this nullcline is reached, the variables slowly follow it until they reach its maximum value. This is then followed by a rapid transition to the left-most branch of the v nullcline and a slow relaxation to the fixed point. For small values of ϵ, the time of the phase excursion can be estimated by computing the time spent on the v nullcline. For the specific form of the FHN model of Fig. 4, the time spent on the right-most branch of the v nullcline is found by evaluating

$$\epsilon T = \int_{v^*}^{1} \frac{(1 - v^2)}{v + a - b(v - v^3 / 3)} dv \tag{6}$$

where the integral runs from the solution of $f(v^*, -0.625) = 0$ on the right-most branch, to $v = 1$, corresponding to the maximum of the nullcline. A similar expression can be derived for the time spent on the left-most branch of the nullcline.

Even though the FHN model does not posses an actual firing threshold and does not display an all-or-none response [65], its dynamics is qualitatively similar to action potential generation, which is characterized by a rapid upstroke, followed by a slow relaxation to the equilibrium value. Furthermore, it also exhibits the refractoriness seen in cardiac cells: following an excitation as exemplified by trajectory #2 in Fig. 4, a new, large response can only be elicited when the variables have sufficiently recovered. This allows the FHN model to recapitulate generic excitable phenomenon when specific ionic dynamics are not important. However, it lacks several critical elements of the dynamics of cardiac cells and it is certainly not an electrophysiologically accurate model.

A more recent model, specifically developed to mimic cardiac dynamics, was introduced by Fenton and Karma (FK) [70]. In its original version, it contained only three currents (a fast and slow inward, and a slow outward current, which can be viewed as representatives of the Na^+, Ca^{2+}, and K^+ channels, respectively), along with two gating variables and, of course, the voltage. Importantly, and distinct from the FHN model, the parameters of the original FK model and its extensions can be adjusted to mimic features of more detailed models or clinical data [70, 71, 72, 73]. An example of this is shown in Fig. 5A, where the AP shape of a AF patient undergoing an AF ablation procedure is plotted as a dashed line. The AP shape for this patient, and 4 other patients, was obtained during controlled pacing in a patient using a monophasic action potential (MAP) catheter [73]. This type of catheter is able to faithfully record the membrane potential at a specific location [74, 75]. In this study, the FK parameters were adjusted to fit the clinical AP shapes and the results were excellent (see, e.g., the blue line in Fig. 5A). The same study also showed that the parameters of a detailed model, created by Koivumaki, Korhonen, and Tavi (KKT) and that contains 13 currents [56], can be adjusted to fit the AP shape. The result of fitting the parameters of this "KKT" model is shown in Fig. 5A as a red line. As is the case for the FK model, the KKT model parameters can also be fitted to produce good agreements with clinically obtained AP shapes.

Aside from the AP shape, the parameters of the FK model can also be adjusted to replicate several key dynamical characteristics of electrophysiological models and of patients. One example is the APD restitution curve, which describes how the APD recovers as a function of the rest period between repolarization and the next excitation [79]. As we will see in the next section, the APD restitution curve determines the stability of a cardiac cell. The curve can be computed by stimulating a cell using a current with period T, as schematically shown in Fig. 5B. Using the time trace of the resulting potential, we can then define the diastolic interval (DI), which is the time spent by the cell below a certain threshold potential value before a new stimulus (Fig. 5B). By varying the period T we can construct the APD restitution curve, which plots the APD as a function of the DI. In general, this curve has a positive slope: as the DI is reduced, the cell has less time to recover from the previous excitation. Consequently, channels do not open or close fully, resulting in a shorter APD. As T is further reduced, the APD continues to decrease until an excitation is no longer possible. We should point out that different qualitative shapes of the APD curve are possible, including multi-branch structures or ones where the slope is negative [80, 81, 82].

An example illustrating that the FK model (and the KKT model) can be fitted to clinically obtained data is shown in Fig. 5C. Here, the APD vs DI (open symbols), together with its high-order polynomial fit (grey closed symbols) are plotted for the AF patient presented in panel A. The fit of the FK model to the polynomial restitution curve for this patient is plotted in Fig. 5C as a blue line, while the fit for the KKT model is plotted as a red line. Both models were found to be able to replicate the restitution curves of all 5 patients [73].

These results demonstrate that simplified models are able to replicate certain cardiac properties, which make them useful tools to investigate cardiac dynamics in general and arrhythmias in particular. Clearly, as stressed before, the FK model, and similar simplified models, cannot describe the relative importance of specific channels. They can, however, simulate voltage dynamics in a more intuitive and efficient way. Both detailed and simplified models have their role in research and perhaps a hybrid approach, in which a detailed model is systematically reduced to a much simpler one, represents an attractive middle ground [83].

3.2. Cable propagation

So far, we have examined the dynamics of a single cell. Let us now consider what happens if we connect cells and form a cable. This 1-dimensional propagation can be captured by the cable equation, investigated in many studies (see, e.g., [84, 85, 22]). To derive this model, we assume that cells with radius a are coupled with a resistance per unit length equal to R_a and have a capacitance C_m. Then, applying Ohm's law and Kirchhoff's law, we can derive, in the continuous limit, the cable equation

$$\frac{\partial V}{\partial t} = D\frac{\partial^2 V}{\partial^2 x} + \frac{I_{ion}}{C_m} \tag{7}$$

where $D = 1/(4\pi a R_a C_m)$ [85]. Thus, the spreading of the potential V through the cable is governed by a reaction-diffusion equation with a diffusion constant D.

Stimulating a cable on one end with a sufficiently strong stimulus will result in a cardiac wave that propagates along the cable to the other end. It can be shown that the conduction velocity (CV) of this propagating wave scales as $v \sim \sqrt{D}$ [85]. In the case when the cable is paced at regular intervals, similar to the the periodic pacing of a single cell in Fig. 5B, this CV also depends on the period and thus the DI. The property is captured by the CV restitution curve, which plots the CV as a function of the DI. Just as the APD restitution curve, this curve typically has a positive slope: the CV decreases when the pacing frequency is increased. This is shown in Fig. 5D, where the CV restitution curve, obtained by stimulating one end of a 5 cm long cable, is plotted for several electrophysiological models [70]. Mechanistically, the CV restitution arises from the large timescales required to reset the quantities of the cell, most notably calcium. This plot also shows that the FK model parameters can be adjusted to replicate these CV restitution curves. The ability to adjust model parameters to fit CV restitution curves is further demonstrated in Fig. 5E. This plot shows the fits from both the FK (blue line) and KKT (red line) to the clinical CV restitution curve of the AF patient presented in panels A and C.

3.3. 2D and 3D

Aside from some specialized strands of tissue, most cardiac tissue can not be described as one dimensional cables. The next step in increasing complexity is considering wave propagation in flat, 2D sheets. Many studies have been and continue to be performed in these geometries and the results of these studies have been instrumental in our understanding of some of the mechanisms for the initiation and maintenance of cardiac arrhythmias (see Section 4). Furthermore, this geometry is also relevant for atrial tissue, which is generally very thin (< 1mm).

To model propagation in 2D, the cable equation (7) can be straightforwardly modified to allow conductivity in both the x and y direction. The only complication is that, as we have seen in Section 2, cardiac tissue is anisotropic. This means that the electrical conductivity is not uniform in all directions and that the conduction velocity is larger along the fibers than perpendicular to the fibers [35, 36]. Simulating a piece of tissue in an anisotropic domain in which the cells are aligned along the x-direction would thus require a different diffusion constant in the x and y direction, resulting in the following partial differential equation:

$$C_m \frac{dV}{dt} = D_x \frac{\partial^2 V}{\partial^2 x} + D_y \frac{\partial^2 V}{\partial^2 y} + \frac{I_{ion}}{C_m} \tag{8}$$

where I_{ion} includes all the relevant ionic currents. This equation can be straightforwardly implemented using finite difference schemes.

The propagation speed of an activation front also depends on its curvature. To illustrate this, we can carry out two simple simulations using the FK model, as shown in Fig. 6. In panel A, a homogeneous and isotropic computational domain is excited by a line stimulus. This stimulus results in planar waves that propagates in both directions, as indicated by the lines, which represent its location at successive time points separated by 50 ms. Stimulating this domain using a point stimulus instead of a line stimulus will result in concentrically propagating activation waves, as shown in Fig. 6B where we have again plotted the location of the activation front at successive 50 ms time points. As can be seen by comparing these two simple simulations, the speed of the planar wave is larger than the one for the circular wavefront. This can be understood by realizing that the activation is created by neighboring points (or cells) having a larger value of u. For a curved wavefront, the number of neighboring points is less and therefore the speed of the wave front is reduced. The relationship between the speed of a planar and spreading, curved wavefront can be written as

$$v_{curved} = v_{planar} - D / r \tag{9}$$

where r is the radius of curvature of the wavefront [86].

The simulation of Fig. 6B carried out in an an anisotropic domain (i.e., using unequal values of D_x and D_y) would result in a propagation pattern that is elliptical rather than circular. Specifically, if $D_x > D_y$, this pattern would be elongated along the x-direction. However, for a fixed anisotropy pattern, we should note that it is possible to simply rescale the x and

y coordinate, rendering the simulation isotropic again. For more complex fiber alignment patterns, where D_x and D_y are not constant in space, such rescaling is not feasible anymore.

To simulate cardiac wave propagation in 3D geometries requires solving the equation

$$\frac{dV}{dt} = \overrightarrow{\nabla} \cdot \widetilde{D} \overrightarrow{\nabla} V + \frac{I_{ion}(V)}{C_m} \tag{10}$$

where the diffusion tensor $\widetilde{D}$ is a 3x3 matrix which reflects the different propagation speeds along and transverse to the fiber orientation. This equation has to be supplemented by a no-flux (zero normal current) boundary condition:

$$\hat{n} \cdot \widetilde{D} \overrightarrow{\nabla} V = 0 \tag{11}$$

where $\hat{n}$ is the normal vector to the boundaries of the computational domain.

For simple geometries, such as a slab, this boundary condition can be readily implemented using finite difference algorithms that use regular grids [70, 88]. Realistic anatomical geometries, however, have curved boundaries, which makes it more challenging to use these finite difference schemes. One way to employ regular grids for these geometries is to use the phase field method, which has been extensively utilized in problems where a free boundary separates two phases [89, 90, 91, 92]. In this method, a new field, ϕ, is introduced that takes on $\phi = 1$ in the interior and $\phi = 0$ in the exterior of the heart and which varies rapidly and smoothly across a thin diffusive interface connecting the interior and exterior. The modified propagation equation then reads:

$$\frac{\partial}{\partial t}(\phi V) = \overrightarrow{\nabla} \cdot \left[D\phi \overrightarrow{\nabla} u \right] - \phi \frac{I_{ion}}{C_m} . \tag{12}$$

The precise form of the phase-field profile in the thin interface region is not critical to the algorithm and can be calculated via a relaxation method [93]. Since the boundaries are stationary, the profile only has to be computed at the onset of the simulation. It can then be shown that in the sharp interface limit, in which the interface width becomes negligible, this formulation recovers the appropriate no-flux boundary condition [93]. In principle, this method can also be extended to include moving boundaries, as has been done in a variety of other so-called free boundary problems [94, 95]. In this case, the dynamics of the phase field must be coupled to other physical fields through an appropriate set of differential equations.

Despite its ease of implementation, the phase field method has several limitations. Most notably, it is challenging to implement it for geometries that consist of very thin sheets since the width of the diffusive interface needs to be less that the smallest scale of the geometry. Thus, simulating electrical activity in atria with its thin walls would require a very fine spatial discretization and the phase field method may not be ideally suited for this geometry. To circumvent this problem, many current studies that use anatomically realistic geometries use either finite element [96, 97, 98] or finite volume algorithms [99, 100]. These models can also incorporate realistic fiber orientations that are derived from

imaging data such as the ones shown in see Fig. 3 [101, 102, 103]. As a result, it is now possible to develop patient-specific and personalized models of cardiac wave propagation and arrhythmias [104, 105, 106, 107, 108, 109, 110]. Recent developments also include the introduction of an open-source computational platform that can simulation cardiac models in a variety of geometries. This platform, OpenCarp, is actively maintained and should provide the community with a robust and well-tested package [111]. OpenCarp can simulate electrophysiological models in a variety of geometries, including anatomically derived atria and ventricles, as detailed on its website https://opencarp.org/.

Going to higher dimensions is clearly more challenging from a computational point of view. This is, of course, especially true for the more complex models, which can contain up to 100 different equations per element or grid point [50, 112]. Furthermore, cardiac models require high temporal and fine spatial resolution to capture the steep activation wavefront. Recent advances in computational approaches, however, have made performing extensive simulations more accessible. Specifically, the use of large-scale parallel processing using graphic processing units (GPUs) have resulted in significant gains in computational speed [113, 114, 115]. Furthermore, simulations can now be performed through web browsers, making it possible to run them without the installation of additional software on different computational platforms [116].

As a final note, we should mention that the model equations described above only consider the cardiac cells and not the extracellular space that surrounds these cells. It is therefore called the monodomain model in the literature. In contrast, the bidomain model takes into account the electrical activity in both the intracellular domain (the cardiac cells) and the extracellular domain [117]. In this model, both the potential in the intracellular domain, ϕ_i, and the potential in the extracellular domain, ϕ_e are thought to co-exist in space. One can then derive differential equations describing the two potentials [118, 119, 120]:

$$\nabla \cdot \sigma_i \nabla \phi_i = \beta(C_m \frac{\partial}{\partial t}(\phi_i - \phi_e) + I_{ion}) - I_i \tag{13}$$

$$\nabla \cdot \sigma_e \nabla \phi_e = -\beta(C_m \frac{\partial}{\partial t}(\phi_i - \phi_e) + I_{ion}) - I_e \tag{14}$$

In these equations, we have allowed for current sources in the intra- and extracellular space, respectively. Furthermore, β is the surface to volume ratio of the cardiac cells and σ_i and σ_i are the conductivity tensors in the two domains. The transmembrane potential is then the difference between the intracellular and the extracellular potential: $V_m = \phi_i - \phi_e$. It is easy to verify that if the two conductivity tensors are proportional we recover the monodomain equation Eq. 10.

Solving the coupled bidomain equations is more challenging and computationally more expensive than solving the monodomain equation [121, 122, 123]. Fortunately, for many cases the two models give almost identical results, negating the need for a bidomain approach. For example, a careful numerical study that simulated both the monodomain and bidomain model in an isolated human heart showed that the differences in propagation

patterns between the two models were small enough to be ignored [124]. For certain applications, however, the bidomain is critical. For example, when simulating applied currents, and in particular large currents as in the case of defibrillation, the bidomain model should be the model of choice [122]. Furthermore, to find accurate results for the magnetic field [125] or for the effect of fiber orientation on the membrane potential in the presence of an applied field requires the bidomain model [126]. We will briefly revisit the bidomain model in Section 4 when we discuss wave block and reentry and in Section 6 when we describe low-voltage defibrillation techniques.

4.   Initiation of arrhythmias

Normal sinus rhythm corresponds to a coherent wave that propagates from the right atrium to the ventricles. Arrhythmias are rhythm disorders, characterized by the disruption of this coherent wave propagation. These arrhythmias are the result of instabilities that arise either at the single cells level or at the tissue level. In either case, the resulting wave propagation is no longer coherent and can be characterized as a spatio-temporal disturbance. We will first discuss how a single cell undergoing periodic pacing can be destabilized. We will then address spatially extended instabilities, including the important concepts of reentry and spiral wave breakup.

4.1.   Single cell instabilities

4.1.1.   Alternans—When a single cell is paced with a constant frequency, the cell can develop an instability, resulting in an APD that is not constant. One particularly well studied example of such an instability is electrical alternans [127, 128, 129, 130, 131, 132, 133, 134]. During alternans, the sequence of APDs of a cardiac cell alternates between long and short and the first reports date back more than a century ago [135]. Alternans became a focus within the cardiac community when the beat-to-beat alternation of the T-wave on the ECG was recognized as a precursor to ventricular arrhythmias and sudden cardiac death [136, 137]. It garnered further attention when it was found that this instability may also play a role in the initiation of atrial fibrillation [138].

The slope of the APD restitution curve (see Fig. 5) has long been recognized as an important determinant for the initiation of electrical alternans [139, 140, 141]. As we recall from Section 2, this curve relates the APD to the preceding DI and in Fig. 7A&B we have plotted a restitution curve with a slope of less than and larger than 1, respectively. For a periodically paced cell, the sum of the APD and DI should be equal be equal to the pacing period T ($APD + DI = T$) and this line is plotted as a dashed line in Fig. 7A&B. To investigate whether the intersection of this line and the restitution curve (red point in Fig. 7A&B) is stable we can construct a cobweb diagram, a standard graphing technique in dynamical systems [142, 143]. To construct this diagram, we perturb the DI and find the corresponding APD from the restitution curve (blue point in Fig. 7A&B). This APD results in a DI that can be found using the period relationship (dashed line) which, in turn, leads to the next APD. Repeating this procedure, we can see that for restitution curves with a slope < 1 the perturbation decreases, indicating that the point is stable (Fig. 7A). For a slope > 1, however, the perturbation grows and the APD and DI alternate resulting in long-short-long

sequences (Fig. 7B). An example of this sequence is shown in Fig. 7C where the FK model is stimulated with a period corresponding to a slope of the restitution curve that is larger than one. As a result, the APD is long for one stimulus and short for the following.

The instability condition can also be derived algebraically. To determine the stability of a point APD^* and DI^* on the restitution curve, consider perturbing the diastolic interval by δDI: $DI_1 = DI^* + \delta DI$. For a linear restitution curve with slope a, the next action potential will have a duration of $APD_2 = APD^* + a\delta DI$ and the subsequent DI is given by $DI_2 = DI^* - a\delta DI$. Repeating this, we find that the n-th APD is given by

$$APD_n = APD^* + (-1)^n\alpha^{n-1}\delta DI \tag{15}$$

As one can see from this result, APD_n will approach APD^* as long as $a < 1$ but will diverge from APD^* if $a > 1$. Thus, points on the restitution curve with slope smaller than one are stable while points with a slope larger than one are unstable.

Aside from electrical alternans, manifested by APs with alternating durations, experiments have also shown alternans in intracellular Ca^{2+} cycling [144]. The fact that Ca^{2+} cycling shows alternans is perhaps not surprising, since there is a directional coupling between voltage and Ca^{2+} handling. As we have discussed in Section 2, Ca^{2+} is released from the SR upon depolarization and pumped back by SERCA pumps during the relaxation phase of the action potential. Thus, voltage regulates the release of Ca^{2+}, which means that electrical alternans can automatically result in alternating Ca^{2+} signals. In fact, this coupling is bi-directional since the amount of released Ca^{2+} also affects the LCC (it inactivates in a Ca^{2+} dependent manner) and the sodium-calcium exchanger (positively regulated by intracellular Ca^{2+}).

Initially, it was not clear if calcium alternans could occur without electrical alternans. Experiments in which the voltage was clamped and therefore did not alternate have shown, however, that calcium alternans can occur even in the absence of APD alternans [145]. Furthermore, additional experiments have demonstrated that APD and calcium alternans can even be out of phase, with the voltage displaying a short-long-short sequence while the Ca^{2+} concentration shows a long-short-long sequence [146]. An example of calcium alternans in a ventricular myocyte of a rat is shown in Fig. 8A. Here, the Ca^{2+} concentration along a line within the myocyte is plotted as a function of time for three successive beats using a fluorescent Ca^{2+} indicator [147]. Clearly, the Ca^{2+} release is large following the first and third beat, but not following the second beat.

The mechanisms responsible for calcium alternans have been actively investigated since its discovery (for a review, see e.g. [148]). To fully understand calcium alternans requires a more detailed look how Ca^{2+} is released from the SR following excitation. It turns out that this release does not necessarily occur uniformly within the entire myocyte. This is because Ca^{2+} is released from so-called calcium release units (CRUs), consisting of a few LCCs and roughly 100 RyRs. A typical myocyte contains approximately 20,000 CRUs that are closely packed in a three-dimensional 3D grid [149]. Calcium release from a single CRU, called a spark, is highly localized both in time (a typical spark lasts roughly 30 ms) and in space ~

2 μm. A spark is thus the elementary event in cardiac excitation-contraction coupling [150]. Furthermore, calcium sparks are stochastic (since LCCs and RyRs have random opening properties) and refractory: the probability of releasing calcium immediately following a spark is reduced and slowly recovers over ≈400ms [149]. In addition, the CRUs are coupled through the diffusion of Ca^{2+}, which can lead to waves of Ca^{2+} within a myocyte [151].

Computational models of coupled CRUs have demonstrated calcium alternans, as shown in Fig. 8B&C. Fig. 8B shows the calcium release of a 2D slice of a simulated cell and, as in the experimental result, the Ca^{2+} release alternates between large and small values. Furthermore, as shown from the line scan in Fig. 8B taken from a simulation of coupled CRUs, a wave of Ca^{2+} is triggered and propagate through the myocyte, consistent with experimental results. To further gain insight into calcium alternans, it is possible to derive a recurrence equation that relates the number of sparks in one beat to the number of sparks in the preceding beat [148]. For this, it is assumed that a CRU can fire (i.e., release Ca^{2+}) either through the direct activation by LCCs, with probability α, or in response to the firing of a neighboring CRU, with probability γ. The latter can arise from an increase in local Ca^{2+} due to diffusion. If we assume that CRUs recover with a probability β, that there are N_0 total CRUs present, and that the fraction of recruited CRUs through diffusion is f, we obtain for the number of sparks in beat $i + 1$, N_{i+1}, the following expression:

$$N_{i + 1} = \alpha(N_0 - \beta N_i) + (1 - \alpha)(N_0 - \beta N_i)f \tag{16}$$

In this expression, the first term represents firing from CRUs induced by the opening of LCCs while the second term represents firing due to diffusion from neighboring CRUs [152, 153]. For a well-mixed system, where the firing probability is uniform in space, the fraction f can be shown to be given by

$$f = 1 - (1 - \alpha\gamma[1 - \beta N_k / N_0])^M \tag{17}$$

where M is the number of nearest neighbors of a CRU. The iterative map can be analyzed to determine its steady state and its stability. This analysis reveals that a period-doubling instability, which represents alternans, can only occur for non-zero values of γ and β and when α deviates from one. In other words, alternans results from recruitment, refractoriness, and the stochastic firing of the CRUs.

4.2. Wave block

Alternans as described above is a single cell instability. However, most cardiac arrhythmias, including AF and VF, are spatio-temporal events and need to be investigated in spatially extended domains. One critical ingredient in the initiation of spatially extended arrhythmias is wave block, which occurs when the activation front is no longer able to propagate further and stalls. This can be either because the region is non-conductive due to, for example, injury or because it is temporarily refractory due to its specific electrophysiological properties. In either case, the wave stalls and, in a 1D cable, activation would terminate. In 2D or 3D, however, a different scenario can develop in which the wave is blocked in a particular region but continues to propagate around it. Under certain conditions, this

can result in a wave that curls around this region but "reenters" it after it has sufficiently recovered. This reentry is believed to be of paramount importance in the initiation of arrhythmias.

Wave block and reentry can be nicely illustrated by a conceptual "pinwheel" experiment, proposed by Winfree [155, 156] and schematically shown in Fig. 9A. In this figure, an initial stimulus has produced a planar activation wave, indicated by the green line and propagating from left to right. Behind the activation front the tissue is slowly recovering, illustrated by the graded gray scale, and is in the refractory state. After some time, a second stimulus is applied and the resulting activation pattern will depend critically on the timing of this second stimulus. Given immediately following the activation front, the entire stimulus will be firmly in refractive tissue and will not result in any additional activation. If the extra stimulus is provided a long time after the initial wave front has passed, the tissue will no longer be refractory and a new circular wave front will propagate radially outwards. For stimuli between these two extremes, something more interesting will happen, as indicated in the figure: the stimulus will result in propagation in the retrograde direction while it will be blocked in the opposite direction, as indicated by the green and red symbols, respectively. As the retrograde front progresses, the refractory tissue will further recover, eventually becoming excitable. As a result, the wave front can now curl around and reenters the previously inexcitable tissue, as depicted by the two curved green arrows in Fig. 9A.

The result of this properly timed extra-stimulus are thus two reentry waves. Given enough space, these reentry waves can continue to curl, leading to two counter-rotating spiral waves and a so-called figure-of-eight reentry pattern. We should point out that these spiral wave solutions are not only found in simulations of cardiac tissue but are generic solutions of spatially extended excitable systems. They are found in a variety of other systems, included in aggregation patterns of cells of the social amoeba *Dictyostelium discoideum* cells [157], in chicken retinas [158], in the oxidation of surface catalytic systems [159], and in chemical Belousov-Zhabotinsky systems [160, 161].

An example of the creation of spiral waves using the above pinwheel scenario is shown in Fig. 9B-E. Here, we used the FK model [70] and first created a planar wave that propagated from left to right in a 5x5 cm^2 computational domain. We then excited a region behind the activation front by adding a constant current to the equation of the voltage for a duration of 1ms (panel B). As can be seen from the snapshots, the part of the stimulus directed towards the planar front failed to propagate since it falls within the refractory period. The back part of the stimulus, however, was able to propagate into freshly depolarized tissue (panel C) and reentered into the previously refractory tissue (panel D). In this simulation, the amount of space was sufficient for the two reentry waves to curl backwards (panel D), resulting in two spiral wave and a figure-of-eight pattern (panel E).

As mentioned above, the timing of the additional stimulus is critical in the formation of a reentry pattern: a stimulus that is given too early will not result in any excitation while a stimulus that is given too late will result in centrifugal propagation. This means that there is a specific time interval T, termed the vulnerable window, which will lead to reentry [162, 163]. The size of this vulnerable window was estimated by Winfree as the ratio of size of

the circular stimulus and the conduction velocity of the planar front, v_{plane} [156]. This can be intuitively understood by realizing that a very fast moving wave should have a small vulnerable window. In addition, a stimulus with a large spatial extent will more easily cover both the refractive and non-refractive part of the tissue and will thus have a larger vulnerable window. A more precise result, using simple geometric arguments, was obtained by Yang *et al.*: $\Delta T = \sqrt{(R - R_c)} / v_{plane}$ [164]. In this expression, R_c is the critical stimulus size, below which propagation is not possible.

The generation of spiral wave reentry using a properly timed premature stimulus has been demonstrated in the laboratory as well [165, 166, 167]. The patterns observed in the experiments, however, are typically more complex than shown in Fig. 9. One reason for this is that cardiac tissue is anisotropic while the simulation in Fig. 9 was carried in an isotropic domain. Furthermore, simulations using the bidomain model, introduced in Section 3 and which takes into account both intracellular and extracellular resistivities, showed that more intricate patterns are possible [168, 169]. Some of these patterns were subsequently verified in an experimental study [170].

4.2.1. Alternans and reentry—Let us come back to alternans, characterized as an APD with alternating long and short duration. In Section 4.1.1 we introduced alternans as a single cell instability and it is not immediately clear how an instability at the single cell level can result in dangerous arrhythmias, as reported in the clinical literature [136, 137]. After all, coupling identical cells in a 1D cable or a 2D sheet will result in so-called spatially concordant alternans. In this dynamical state, not considered to be pro-arrhythmic, the entire spatial domain shows alternans with all elements in phase. In other words, during concordant alternans the alternating APD sequence is uniform in space with each point exhibiting the same short-long-short sequence. The pro-arrhythmic nature of single-cell alternans is related to a spatio-temporal instability that can develop when we couple these cells. This additional instability was observed in experiments in rings of cardiac tissue, which showed that the propagation of a pulse can become unstable if the circulation time around the ring was reduced [171]. This instability was also observed in computer simulations of a ring of cardiac tissue and in optical mapping experiments of the activation activity in guinea pig hearts [172, 129]. These studies showed that spatially extended systems can exhibit spatially discordant alternans, characterized by spatially distinct regions in which the alternans is out of phase. In other words, the alternans is no longer spatially uniform and regions that show small-large-small APD are adjacent to regions that show large-small-large APD. Furthermore, these studies also showed that discordant alternans creates large APD gradients, which can result in unidirectional propagation block. This wave block can then result in reentry, which can initiate arrhythmias, including life-threatening ventricular fibrillation. For a review on spatially discordant alternans, see e.g. [173, 174].

One obvious way of creating spatially discordant alternans is to have heterogeneous tissue with different properties in different regions. As shown by Watanabe *et al.*, however, homogeneous tissue that display concordant alternans can also create spatially discordant alternans [175]. Specifically, they showed that such discordant alternans can be initiated in one of two distinct scenarios. In the first, a cable is paced on one end and a extra stimulus

is given at the other end. For the right pacing rate and timing of the premature stimulus, the interaction between the activation wave from the pacing site and from the extra stimulus can create two regions in which the alternans exhibits different phases. This scenario, however, requires fine tuning of the pacing rate and timing of the premature stimulus and may not be of clinical relevance.

The second scenario involves CV restitution, already encountered in Section 3 (see Fig. 5). This scenario is illustrated in a computer simulation shown in Fig. 10A. The cable is paced at one end (top) with fixed rate and the first stimulus, shown as the left-most sequence and labeled A0, is applied after the tissue was at rest for a prolong period of time. As a result, the APD is long but the following DI is short. Due to CV restitution, the second stimulus (A1) has a smaller CV than A0, resulting in an increase in APD, and thus DI, as the pulse travels down the cable. The third stimulus follows a long DI and has thus a large CV. This, together with the increase in APD along the cable from the previous beat, results in decreasing DI and APD as the pulse travels down the cable. The next pulse, DI and APD increases again from top to bottom of the cable. This sequence of different speeds in successive beats is repeated, resulting in a spatial gradient of the APD. For steep enough CV restitution curves, eventually a node is formed, which separates a spatial region that exhibits small-large-small APD with a region that shows large-small-large APD. This is shown in the remainder of this panel, which plots the 13th and higher stimulus: both the top and bottom show alternating APDs that are out-of-phase. In 2D, this scenario results in out-of-phase regions that are separated by a nodal line, as illustrated in Fig. 10B. This nodal line separates the two out-of-phase regions and points on this line do not exhibit alternans.

The spatiotemporal dynamics of alternans of 1D and 2D paced tissue was mathematically analyzed by Echebarria and Karma [176, 177]. They derived an equation for small amplitude alternans and showed that a linear instability could lead to nodes in paced tissue that are either stationary or traveling. Furthermore, they showed how the wavelength of the pattern is a function of the electrotonic coupling and the CV restitution curve. Finally, the fact that discordant alternans can spontaneously arise in homogeneous tissue was also shown experimentally using optical mapping in paced rabbit hearts [178].

How is alternans in spatially extended system pro-arrhythmic? The answer lies in conduction block and reentry. Envision an extra stimulus in the spatial region of short APD, as indicated by the asterisk in the blue part of Fig. 10C. Within this spatial region, the resulting activation wave is able to propagate. Once it crosses the nodal line, however, it encounters the region of long APD. For an appropriately timed extra stimulus, this encounter will result in propagation that is blocked along the black line in the figure. However, as the wave is blocked, it continues to propagate in the direction parallel to the line of block. Eventually, the tissue on the long APD region repolarizes and activation can reenter. This will then potentially initiate spiral wave formation.

4.3. Tissue heterogeneities and wave breakup

Key ingredient in the above scenario is the large gradient of APD at the nodal line. This gradient, created even though the tissue is homogeneous, is purely due to the dynamics of the tissue and results in wave block and failure of propagation. It is also possible, however,

to create wave block and subsequent reentry in the presence of tissue heterogeneities. These heterogeneities can be pathological, due to disease, but also occur naturally in the heart. For example, the ventricular shows a significant transmural gradient in the APD, even in non-failing hearts [179]. Such heterogeneities can result in the local failure of propagation and in reentry.

The effect of heterogeneities on wave propagation has been studied extensively in both 2D and 3D computer models [180, 181, 182, 183, 184, 185]. An example of a heterogeneity-induced spiral wave is shown in the simulation snapshots of Fig. 11A [180]. Here, the FHN model is simulated in a rectangular domain with non-periodic boundaries. This domain contains a heterogeneity bounded by the red lines within which the refractory period is larger. Planar waves enter the domain from the left hand side. As a result of the increase in refractoriness in the heterogeneous region, the second planar wave is blocked when it encounters the heterogeneity. However, since the second wave has a lower velocity than the first one, eventually it is able to enter the heterogeneous region, resulting in reentry and a spiral wave.

Heterogeneities can also form in diseased or aging hearts, either acutely or over time. An example of the former is present in acute ischemia, during which part of the heart is deprived from oxygen. This lack of oxygen affects several ion channels and can result in significantly reduced conduction velocities and wave block [188]. An example of the latter can be found in the fibrotic remodeling of cardiac tissue. Fibroblasts are the most numerous cell type in the heart and play a critical role in maintaining the mechanical structure of the heart [189]. Due to aging or injury, these fibroblasts can be activated and differentiate into myofibroblasts, resulting in the deposition of excessive amounts of collagen fibers and fibrosis [190, 191, 192, 193, 194]. These collagen fibers can then act as conduction barriers between adjacent myocyte strands, altering the conduction properties of the tissue. Furthermore, fibrotic remodeling also affects the gap junction coupling between myocytes, resulting in a decrease in the longitudinal and transverse conduction [195, 104].

To incorporate the effects of fibrotic remodeling in computational models is challenging and is an active field of research, as reviewed in [196]. These models need to provide a description of the coupling between myofibroblasts and myocytes, the alteration of gap junction coupling, and the inclusion of non-conductive collagen fibers. The latter is particularly challenging since fibrosis can manifest itself not only in compact patterns, characterized by a relatively large area of non-conductive tissue, but also in diffuse patches, with short collagen strands scattered among myocardial fibers, or patchy patterns, characterized by small regions of fibrotic tissue [197]. These microstructure patterns require resolving propagation on small length scales, and it is still unclear if continuous modeling can appropriately mimic fibrosis [198]. For this reason, several studies are employing discrete approaches in which tissue is represented by discrete elements [199, 200, 201]. Furthermore, hybrid models, which combine continuous and discrete modeling approaches, are also being developed [202].

Regardless of the computational approach, modeling has shown that the inclusion of fibrosis can result in wave breakup and reentry [203, 204, 205, 206, 207, 186, 208]. Especially

diffuse or patchy fibrosis is pro-arrhythmic. An example from one of these simulations is shown in Fig. 11B, where a circular patch of fibrosis, modeled as a region with a high fraction of non-conducting links, is embedded in a 2D computational sheet [186]. A propagating planar front breaks inside the fibrotic region and reenters the homogeneous region, resulting in reentry and continuous activation of the tissue.

Clinical studies using advanced magnetic resonance imaging techniques have shown that fibrotic regions are linked to ventricular arrhythmia [209]. In addition, imaging studies have demonstrated that patients with more severe fibrosis have a larger probability of recurrent arrhythmia after AF ablation [210]. Recently, the results of these imaging studies were incorporated into patient-specific computer models of atrial wave propagation [206, 104, 207, 187, 106, 211]. An example of such a study is shown in Fig. 11C, where four snapshots of propagation patterns after the initiation of AF are plotted [187]. In this simulation, which uses a patient-specific geometry and fibrosis distribution, premature stimulation was able to generate reentry at a spatially conserved location. Importantly, the locations of these reentry events were highly correlated with zones of increased fibrosis, demonstrating that fibrotic remodeling can play a significant role in the generation of reentry and arrhythmia.

4.4. Spiral wave breakup

A single or a pair of spiral waves, as in the figure-of-eight pattern shown in Fig. 9, is likely not fatal to patients even if they form in the ventricles. It may result in an elevated heart rate (tachycardia) since the spiral wave will have a period that is shorter than the typical sino-atrial node period [212]. The activation of the heart, however, will still be mostly coherent, resulting in reduced but non-fatal pumping ability. The activation patterns during fibrillation, on the other hand, are less coherent than those created by a single of a pair of spiral waves and, most likely, involve multiple and possibly migrating spiral waves [213, 214]. This would mean that the initiation of fibrillation would encompass not only the creation of a spiral wave but also the break up of this spiral wave [127, 215].

Moe and co-workers, using a cellular automaton model, were the first to hypothesize that the breakup of spiral waves could underlie cardiac fibrillation [63]. Their computational model showed that a single spiral wave could break up in multiple wavelets in a stochastic fashion. These wavelets migrated through the domain and continued to be annihilated and born, resulting in a self-sustained computational arrhythmia.

Since this seminal work, many computational studies have demonstrated spiral wave breakup [216]. These simulations include algorithms that treat the medium as a continuum and cast the equations for the voltage in terms of the partial differential equations described in Section 3 (Eq. 8 and Eq. 10). Furthermore, the mechanisms behind spiral wave breakup have also been thoroughly investigated. Karma, for example, demonstrated that alternans can destabilize spiral waves [217, 128]. Specifically, he showed that alternans results in oscillations of the APD of the spiral wavefront. Once these oscillations become large enough, they lead to conduction block and to spiral wave break at that location.

Alternans is not the only mechanism that can create spiral wave breakup in homogeneous tissue. In an exhaustive numerical study, Fenton *et al.* revealed a number of potential

mechanisms for spiral wave breakup [87]. For example, aside from alternans, which will result in APD oscillations and wave break far from the tip, they showed that a steep APD restitution can also result in breakup close to the tip. In this case, the CVs of the front and back velocity of the wave are no longer identical, resulting in wave block and breakup. Another mechanism involves a Doppler shift in the wave frequency due to tip meandering. The Doppler effect arises since the tip, which can be viewed as a wave source, is moving so that the frequency is higher in the direction in which the spiral is moving than in the opposite direction. This higher frequency can then lead to wave block and breakup, even in the absence of a steep APD restitution curve (i.e., a curve with a slope smaller than one), as illustrated in Fig. 12. A final example comes from so-called supernormal CV restitution curves, observed in, for example, the His-Purkinje system [218]. In these curves, the CV *increases* rather then decreases as the DI becomes smaller. Due to this increase in the CV, there is a crowding of spiral waves, which can result in breakup. As with the Doppler effect, this breakup can occur for APD restitution curves with slopes that are smaller than one.

4.5. Spiral tips and their trajectories

It is clear from our discussion so far, that spiral waves play an important role in arrhythmias. How can we quantify the motion of these spiral waves? This is most commonly achieved by determining the location of the spiral wave tip. This tip can be thought of as the point where the activation front, separating the freshly excited tissue from recovered tissue, and the de-activation front, indicating where the tissue is recovered, intersect. To determine the location of this tip, it is common to construct a phase maps, which shows the progression from depolarization to repolarization [213]. The spiral tip then corresponds to a singularity, which is defined as the point around which the integral of the gradient of the phase ϕ is not equal to zero. Thus, the tip can be determined by computing the line integral around a closed path $\vec{s}$ [213, 219, 220]:

$$PS = \frac{1}{2\pi} \oint \vec{\nabla} \phi \cdot \vec{s} \tag{18}$$

If this closed path contains a single phase singularity, then $PS = \pm 1$, depending on the chirality of the spiral wave. Several different techniques can be used to compute these phase maps and the most common one employs applying the Hilbert transform to the time trace of the voltage $V(t)$:

$$H(V(t)) = \frac{1}{\pi} P\left[\int_{-\infty}^{\infty} \frac{V(\tau)}{t - \tau} d\tau \right] \tag{19}$$

where P is the Cauchy principal value of the integral. This operation, which is equivalent to taking the convolution of $V(t)$ with $1/\pi t$, results in a signal that is phase shifted by $\pi/2$. The analytical signal, defined as $V(t) + iH(V(t)) = A(t)e^{i\phi(t)}$, can then by used to construct the phase, which can be taken to be between $-\pi$ and $+\pi$.

An example of this is shown in Fig. 13A where we have plotted a snapshot of the voltage in a simulation of a single spiral wave. The voltage in this simulation was normalized to be

between 0 and 1 and the isocontours of V and $H(V)$ (chosen to be 0.5 for both) are shown in red and green, respectively. The phase singularity, corresponding to the spiral wave tip, is the intersection between these two lines and is indicated as a yellow dot.

It is trivial to extend this computation to a snapshot of a simulation with spiral wave breakup. In these simulations, spiral waves can rotate either counterclockwise or clockwise. This is illustrated in 13B, which shows a simulation of spiral wave breakup in a domain with non-conducting boundaries. In this panel, we have marked the tips of all clockwise rotating spirals as a black dots and the tips of all counterclockwise rotating spirals as a white dots. Furthermore, we have also plotted the activation and repolarization fronts as black and green lines, respectively. For topological reasons both fronts need to start and end at either a phase singularity of a non-conducting boundary. Therefore, for computational domains with periodic boundary conditions, spiral tips always come as pairs, corresponding to a counterclockwise and a clockwise rotating spiral.

Computing the spiral tip as a function of time results in a tip trajectory. This trajectory can take on a wide variety of shapes, depending on the parameters of the model (see, e.g., [222, 223]). For example, the trajectory can be perfectly circular or can meander through space, resulting in a "flower-like" pattern. These two possibilities are presented in Fig. 13C and D where a change in one parameter of the FK model dramatically alters the trajectory [221]. More complicated trajectories, including ones in which the path contains large linear segments, are also possible.

Even though these trajectories are the results of non-linear PDEs, previous studies have shown that the dynamics of spiral tips can be analyzed in terms of ordinary differential equations near bifurcation points [224, 225] and that simple equations can describe circular tip trajectories in the presence of periodic modulations [226]. Furthermore, the tip trajectories be faithfully reproduced by a single particle (SP) model, which describes the x and y coordinate of the spiral wave tip and, thus, ignores the spatial extent of the spiral wave arms. This is particularly the case for trajectories with dynamics that contain only a few frequencies. In this case, this model describes a single particle subject to periodic forcing terms with frequencies ω_1 and ω_2 and amplitudes F_1 and F_2:

$$\frac{d^2 x(t)}{dt^2} = F_1 \cos(\omega_1 t + \phi) + F_2 \cos(\omega_2 t) - \xi \frac{dx}{dt} \tag{20}$$

$$\frac{d^2 y(t)}{dt^2} = F_1 \sin(\omega_1 t) + F_2 \sin(\omega_2 t) - \xi \frac{dy}{dt} \tag{21}$$

where the phase ϕ determines whether the pattern is inward ($\phi = 0$) or outward ($\phi = \pi$) and where the third term represents a damping that prevents the model from drifting and allows it to converge to a steady state quickly. This SP model can be trivially solved and the parameters can be immediately determined from the tip trajectory computed using the spatially extended electrophysiological models [221]. Specifically, the angular frequencies are obtained from the power spectrum of the trajectory, with ω_1 corresponding to the overall

period of the spiral and ω_2, corresponding to the angular frequency of the petals in the flower patterns. Furthermore, F_1 and F_2, are determined by the overall size of the trajectory, and the size of the petals.

As shown in Fig. 13E, the SP model can faithfully capture the spiral wave trajectory of full, spatially extended electrophysiological models. In this panel, the trajectory of the full model is plotted in blue while the trajectory of the corresponding single particle model is plotted in red. The left and middle panel show the trajectories of the FK model corresponding to the snapshot in Fig. 13C&D. Both the simple circular trajectory as well as the meandering trajectory (middle column) are reproduced by the SP model. The SP model can also reproduce tip trajectories obtained using more complicated electrophysiological models [221]. An example of this is shown in the right-most trajectory in Fig. 13E, which represents the trajectory in the detailed KKT model [56], already encountered in Fig. 5, and its single particle counterpart (red). Even though this detailed model contains 13 currents and more than 40 parameters, its trajectory can still be accurately described by a single particle subject to two periodic forces. For more complicated trajectories, it should be possible to extend the number of frequencies appearing in the force terms.

Recently, it has been shown that this SP model can also be used to replicate more complex tip trajectories found in spatially extended models in the presence of heterogeneities. These complex trajectories were found in simulations of a single spiral wave in the presence of a pair of equal-sized heterogeneities, in which the conductance was decreased. Specifically, when the conductance inside these heterogeneities was decreased, trajectories in both the simple FK model and the detailed KKT model were found to display chaotic tip trajectories. Simulations revealed that the size of the heterogeneities and their spacing critically determined the tip dynamics [221]. This is quantified in the phase diagram shown in Fig. 14A, which also plots three trajectories for fixed heterogeneity size and different spacing. The phase diagram shows that for both small and large spacings, the spiral tip dynamics is regular: for small spacings, the spiral wave is anchored to both heterogeneities and orbits around them (blue region, Fig. 14A) while for large spacings, the spiral wave rotates around one of the two heterogeneities (purple region, Fig. 14A). For intermediate spacings, however, the trajectory becomes irregular and the spiral tip alternately circulates around one or the other heterogeneity. By computing the Lyapunov exponent of the time series of the tip [227], it was shown that these trajectories were chaotic. These dynamics can also be captured by the SP model when the x and y force equations (Eqns. 21) are supplemented by the terms $-\frac{dU(x, y)}{dx}$ and $-\frac{dU(x, y)}{dy}$, respectively. Here, the potential $U(x, y)$, shown in Fig. 14B, represents the two heterogeneities that can be described by two Gaussian wells with circular symmetry and with local minima at the locations of the heterogeneities (c_{x1}, c_{y1}) and $(c_{x2}; c_{y2})$:

$$U(x, y) = -\frac{g}{\sqrt{2\pi}}\left(\exp[-\frac{(x - c_{x1})^2 + (y - c_{y1})^2}{2s^2}] + \exp[-\frac{(x - c_{x2})^2 + (y - c_{y2})^2}{2s^2}]\right) \tag{22}$$

where g parametrizes the depth of the wells. This extended SP model was able to qualitatively reproduce the results of the full model, as can seen in the phase diagram presented in Fig. 14C [221]. As in the full model, for small spacing, the trajectory migrates around both heterogeneities and for large spacing the particle migrates around one of the two heterogeneities. For intermediate spacings, however, the spiral tip trajectory becomes chaotic with a positive Lyapunov exponent (Fig. 14C).

Another example where the single particle model can qualitatively reproduce results from the spatially extended cardiac model equations comes from the intermittent trapping of spiral waves [228]. This trapping was found to occur when a circular heterogeneity with depressed excitability was introduced into a computational domain. This is illustrated in 14D-E, where the tip trajectory of a spiral wave in the FK model is shown in red. The spiral wave migrates through the computational domain, encounters the heterogeneity and is trapped for several rotations, after which is dislodges and migrates further through the domain. This intermittent trapping can also be seen in Fig. 14F, which plots the distance r from the tip to the center of the heterogeneity as a function of time. For this time interval, the particle was trapped three times, as indicated by the red bars. To replicate these dynamics, a single well potential was added to the SP model (Fig. 14G). As in the full model, the SP model also exhibited trajectories that were intermittently trapped (Fig. 14H). Furthermore, the phase diagram in size vs. heterogeneity strength space was qualitatively similar, indicating that the particle model can be used to simulate spiral tip dynamics [228].

4.6. Filaments

Cardiac tissue has varying thickness, ranging from > 1 cm in parts of the ventricles to as small as 1 mm in regions of the atria. Thus, reentry in actual heart tissue, including spiral wave dynamics, can be an intrinsic 3D phenomenon, especially in the ventricles. The 3D equivalent of a spiral wave can be produced by taking a 2D spiral and stacking it in the third dimension. The resulting structure forms a scroll wave that rotates around a singularity line called the filament. In a slab of tissue or in the heart walls, this filament is either attached on both sides to the non-conducting boundary or is closed upon itself, forming a scroll ring. Early experiments in thin tissues showed that spiral waves were stable [229, 230], suggesting that a minimum tissue thickness was needed to observe the progression from tachycardia to fibrillation and that fibrillation is a 3D phenomena. Based on these experiments, it was argued by Winfree that filament instabilities result in a turbulent state, responsible for clinical fibrillation [231].

The stability of a filament has been extensively studied [232, 233, 70, 234, 235, 88, 236, 237], see also the review by Alonso et al. [238]. A critical determinant of this stability is the filament tension. Specifically, a positive tension results in the reduction of the filament length while a negative tension leads to increasing filament lengths. Consequently, under positive tension, scroll rings shrink and non-closed filaments become stable. Under negative tension, however, the size of the ring and filament increase, which can result in instabilities and the formation of multiple filaments.

In addition to negative tension, filament twist also plays a role in determining the stability of filaments. This twist arises from the fiber anisotropy present in cardiac tissue (see

also Section 2). This is illustrated in Fig. 15A where we show a schematic representation of the rotating anisotropy in a wedge of cardiac tissue. Studies have demonstrated that the destabilization of a vortex filament can only occur above a critical thickness, which decreases for increasing rotation rates. An example of such destabilization is presented in Fig. 15B, which shows the scroll wave filament in a numerical simulation of the Beeler-Reuter model [76] in a slab with a thickness of 0.9 cm. As initial condition, a single 2D spiral wave was stacked in the *z*-direction, corresponding to a straight filament. The first frames show that the filament buckles and breaks apart when the curved part touches the upper boundary. In the subsequent frames, the half ring created after a collision with the boundary expands and forms two separate filaments when it reaches a boundary. As time progresses, the activity becomes more irregular and multiple filaments appear.

4.6.1.   Other cardiac instabilities—Aside from alternans and spiral wave breakup, there are several additional instabilities that may play a role in the initiation of cardiac arrhythmias. One of these occurs in the cells of the sino-atrial node. This node consists of a group of specialized cells that generate spontaneous oscillations [239]. Just as other cells in the heart, these cells contain ion channels and their proper function, together with intracellular Ca^{2+} signaling, result in period electrical activations. The improper functioning of this node can result in an abnormally low heart rate, known as bradychardia [239]. This arrhythmia is typically age-related and can be related to progressive fibrosis or ion channel dysfunction and is usually treated by the implantation of a pacemaker.

Another cardiac arrhythmia occurs when signals from the atria are only intermittently able to pass through the AV node into the ventricles [240]. In a so-called n:m Wenckebach rhythm, where n>m, only m ventricular excitations occur for every n atrial beats. These rhythms can be understood when one assumes that the atrium is periodically paced and that the conduction time through the AV node depends on the recovery time after the last excitation. It can then be shown graphically, similar to the case of alternans, that different Wenckebach rhythms can be generated for different frequencies of atrial activation [241, 242].

Finally, it is worth discussing how extra stimuli may occur in cardiac tissue. One possibility is that these stimuli arise from cells that display so-called early afterdepolarizations, during which a repolarizing current develops during the depolarizing phase of the action potential [243]. Both the LCC and the sodium calcium exchange current are thought to play a role in this instability and when enough cells within a spatial domain exhibit these early afterdepolarizations, it can result in an extra stimulus and wave blocks [244, 245]. Another possibility comes from delayed afterdepolarisations, which occur in the diastolic phase following an action potential. These afterdepolarizations are caused by spontaneous calcium release from the SR and can trigger an AP and, thus, an extra stimulus [246].

5.   Experimental and clinical observations of disorders

Clinically, the existence of a rhythm disorder is most often determined using an electrocardiogram (ECG). This is a system of electrodes that is positioned on the patient's body, and thus removed from the heart surface. The electrodes measure the potential arising from the electrical activity of the heart, each lead from a different angle. The depolarization

and repolarization of the cardiac tissue results in characteristic deflections of the electrical trace. These deflections are marked by letters (PQRSTU) on the electrocardiogram and their amplitude, relative timing, and morphology can be analyzed to identify cardiac arrhythmias.

Despite their wide clinical use, the ECG is not able to record the spatio-temporal dynamics of the electrical activation during an arrhythmia. After all, the electrical signals arriving at the ECG electrodes have to traverse the chest of the patient and is therefore not a direct measurement of the electrical activity of the tissue. Thus, ECGs are not able to determine the exact nature of arrhythmias, including fibrillation, let alone the location of reentry waves. Other more sophisticated and often more invasive mapping modalities with a higher spatial resolution are therefore needed to map the spatio-temporal dynamics of arrhythmias. In this section, we will describe some of these modalities. We will start by giving an estimate for the temporal and spatial resolution necessary to accurately map arrhythmias. We will then describe optical mapping techniques, suitable for animal model studies. We will end this section by reviewing electrode mapping techniques, which can be applied to patients, and several other, more recently developed techniques.

5.1. Required spatial and temporal resolution

What is the minimum required spatial and temporal resolution to capture atrial and ventricular fibrillation in a clinical setting? The ability to determine accurate intracardiac maps of AF from noisy signals depends on the level of contamination, as was recently discussed [247]. For signals that are noise-free, on the other hand, the resolution requirements can be estimated from a general scale analysis [248, 249]. The minimum temporal resolution required to map human VF and AF can be estimated from tissue characteristics. The mapping must be able to distinguish activation on neighboring recording sites, and can be found by dividing the spatial resolution by the conduction velocity of the activation fronts. Typical conduction velocities of cardiac fronts are in the range of 50-150 cm/s [250]. Thus, for a spatial resolution of 5 mm applicable to the basket of Fig. 16D, this results in a required temporal resolution in the range of 3-10 ms. This temporal resolution is easily achievable using clinical mapping systems.

The required spatial resolution depends on the length scale of the mapped event. We will consider two different activation patterns: spiral waves and focal sources. For spiral waves, we can identify three spatial scales. The first scale is the wavelength, λ, defined as the spatial separation between two successive arms of the spiral. If this spiral is rotating in a rigid fashion, we can estimate that to accurately capture this spiral we will need approximately 4 spatial grid points between successive wavefronts, resulting in $x_{req} \approx \lambda/4$. Second, a migrating spiral wave has a length scale given by R_{tip}, typically smaller than the wavelength. Finally, there is also a minimum required field of view size, reflecting the scale of the coherent domain of the spiral wave, R_{rotor}. Choosing fields of view that are smaller than R_{rotor} can miss the spiral tip and rotational activity.

These different length scales have been determined experimentally. The spatial scale of the spiral wave tip, for example, ranges from $R_{tip} = 1$ cm to $R_{tip} = 3$ cm, requiring a resolution of 0.5 cm to theoretically map the trajectory of spiral tips [251, 252]. The coherent domain of a spiral wave can be estimated to have an area of > 5 cm^2, corresponding to $R_{rotor} \approx 2.5$

cm [253]. Therefore, the field of view of the mapping technique should be at least 2.5x2.5 cm. The spiral wavelength can be estimated as the product of the minimum conduction velocity and shortest refractory period [254]. In human AF, the former is approximately 40 cm/s [250] while the latter is roughly 110 ms [255], resulting in a minimum wavelength of $\lambda \approx 4 - 5$ cm. Taken together, this means that the smallest spiral waves require a spatial resolution of approximately 1 cm although a larger resolution may be sufficient if the spiral waves are larger. For human VF, the conduction velocity varies within the ventricular wall but is within the same range as AF velocities [256], and the expected spatial resolution requirements are therefore similar to the ones of human AF.

5.2. Optical mapping

Optical mapping is by many considered the gold standard of cardiac imaging. In this technique, voltage sensitive dyes are infused into the heart after which the heart is illuminated with light. The photo-emitting properties of the dyes change as a function of the membrane potential, thus allowing the visualization of cardiac electrical activation and recovery at spatial and temporal resolutions that can easily satisfy the requirements discussed in Sec. 5.1. [257, 213, 258, 259]. These features make optical mapping ideal to map complex activation patterns, including fibrillation.

An example of an *in vitro* experiment using optical mapping is shown in Fig. 16A [260]. This example shows a series of images of a monolayer of cardiac cells where the fluorescence level was directly converted into a color map. From this map, it is possible to determine the spatio-temporal dynamics of tissue activation, which in this case reveals a clear counter-rotating spiral wave. Importantly, in this experiment, the monolayer was prepared such that it was relatively homogeneous and the observed reentry was therefore functional and not dependent on tissue heterogeneities. A second example of optical mapping is shown in Fig. 16B, where the activation on the surface of a rabbit heart during an arrhythmia is visualized using an optical dye [213]. In this case, the fluorescent data is converted into a phase map, which demonstrates the presence of a spiral wave. A final example shows the activation pattern in an explanted human heart (Fig. 16C) [261]. In this case, the activity was measured on both surfaces of the atrium, revealing a rotating reentry pattern.

5.3. Electrode mapping

Currently, optical mapping techniques are not available in humans due to the toxicity of dyes and other technical problems [264]. It is possible, however, to obtain spatio-temporal information of the electrical activity within the atria and ventricles using an array of contact electrodes. Some of these arrays contain many electrodes with spacing as little as ≈ 1 mm but can only map a relatively small area of the tissue [265, 266]. Other arrays cover a large part of the cardiac chamber but with lower spatial resolution [267, 262]. An example of the latter involves advancing basket electrodes into the atria or ventricles of patients and recording signals from the contact electrodes [214, 267, 262, 268]. This basket consists of 8 flexible splines, each containing 8 electrodes, that are inserted into the atria within a sheath. After removing the sheath, the splines extend and make contact with the atrial wall, resulting a spatial resolution of approximately 5 mm and a coverage of approximately

70% of the atrium, as schematically shown in Fig. 16D. Recordings can be made in both chambers simultaneously or sequentially, after which the electrograms can be analyzed to determine the local activation times. These times can then be used to construct activation or phase maps, visualizing the spatio-temporal dynamics of AF or VF. Importantly, these large electrode baskets meet the spatial resolution requirements discussed above.

The difficulty in interpreting the signals from the contact electrodes, however, is to extract the correct activation time. Often, the electrograms are quite noisy due to, e.g., poor contact with the wall or far field effects. These activation times are required to create activation maps, which visualizes the spatio-temporal dynamics of the cardiac rhythm. Alternatively, they can be used to construct a phase map, This is accomplished by using the activation times to assign a phase as a function of time for each electrode location. Once these phase maps have been constructed, they can be used to compute the location of the singularities, corresponding to the tips of spiral waves (see Section 4 and Eq. 18).

The 64-electrode baskets have demonstrated the existence of spiral waves in both the atria and ventricles of patients in AF and VF [214, 267, 262, 268]. Moreover, for AF patients, it was shown that the tips of these spiral waves are often localized in a conserved location, representing a spiral wave that is spatially stable. An example of spatially conserved activations maps obtained using electrode mapping in a patient is presented in Fig. 16D. These maps were obtained 237 days apart and during AF and revealed a counter-clockwise rotating spiral wave in roughly the same location. Since no procedure was carried out during this interval, these maps suggest that in this patient the spiral wave activity during AF is conserved. In other AF patients, however, tip trajectories were shown to be meandering with a significant spatial extent [262].

We should note that these observations are not completely without controversy. Several reports, using high resolution electrode arrays, have failed to observe consistent rotational activity [266, 269, 265]. There are a number of possible explanations for these disparate results. First, these reports typically record activity patterns on the epicardial wall, which may be more complex than endocardial patterns [270]. Second, the spatial extent of these arrays are small, making it more difficult to capture large scale rotational activity. Third, the spatio-temporal patterns are analyzed using activation times at the site of each electrode. As discussed before, the electrical recordings are noisy and assigning activation times is challenging. Incorrect identification of the activation times results in flawed activation maps, which may hinder the identification of rotational patterns.

5.4. Additional mapping modalities

In an alternative to the invasive electrode baskets, the spatio-temporal dynamics of AF or VF can be determined using non-invasive techniques. In one of these techniques, called electrocardiographic imaging (ECGI), the patient is fitted with a vest that contains many (>250) electrodes. The recordings of these surface electrodes, together with structural information about the heart, are then used to determine the spatio-temporal dynamics of the cardiac activation through inverse mapping methods [271, 272, 273]. The reported resolution in humans significantly varies from study to study. For paced beats in the ventricles, representing large current injections and large volumes, the resolution was found to be 10

mm [274]. Surprisingly, in the atria, which has less volume than the ventricles and therefore a smaller signal, the resolution was found to be 6 mm during AF [275]. A more recent article obtained a resolution of 16 mm in dog hearts [276].

Finally, another non-invasive technique that uses ultra-sound is able to visualize 3D scroll waves within ventricular tissue, as reported in a recent study using isolated pig hearts [263]. This technique is able to measure mechanical contractions within the heart with a spatial resolution of 0.5-1 mm. From this data, one can then determine the propagation of mechanical waves, which was shown to coincide with electrical waves that were determined using optical mapping. Furthermore, the mechanical and electrical phase singularities occurred at the same locations, demonstrating that the 3D spatiotemporal dynamics of cardiac fibrillation can be visualized using ultra-sound techniques. An example of the resulting filaments during reentry in the pig heart is shown in Fig. 16E. This promising non-invasive technique, however, has not yet been applied in humans and it remains unclear whether it will have any clinical applications in the near future. Furthermore, it may not be feasible to use in atria, where the thickness of the wall is much smaller than in the ventricles.

6. Treatment of rhythm disorders

A large medical literature exists describing different treatment strategies for different arrhythmias. In this Section, we will focus on the treatment options that are inspired or guided by modeling studies. These include defibrillation, with an emphasis on low-energy defibrillation, and localized ablation techniques. We will also discuss proposed methods to control fibrillation and will discuss how fibrillation may spontaneously terminate. We will start, however, with a brief discussion of the traditional clinical approaches.

6.1. Drug therapy

Drugs that target ion channels can be used to treat patients with cardiac arrhythmias. In the case of AF, for example, patients can be given drugs that either aim to restore and maintain sinus rhythm or that attempt to control the ventricular rate [277, 278]. Unfortunately, the success rate of these pharmacological interventions is relatively low. The problem is that it is challenging to predict how changing the properties of a specific ion channel may affect the spatio-temporal dynamics of heart tissue. What might be antiarrhythmic at the single cell level could be pro-arrhythmic at the organ level. A well known example of this comes from the Cardiac Arrhythmia Suppression Trial (CAST) trial, which was conducted in the 1980s [279]. This trial tested whether so-called class I drugs, drugs that block the fast sodium channel, would reduce the occurrence of VF. Single cell experiments had shown that these drugs were able to suppress spontaneous electrical activity and the hypothesis was that fewer extra stimuli would reduce the risk of fibrillation [280]. Unfortunately, the trial actually showed the opposite and had to be stopped prematurely [279, 281]. It was not until 2011 that a modeling study pinpointed the reason why these drugs were pro-arrhythmic [60]. This study showed that even though these sodium channel blockers may reduce spontaneous electrical activity they can also increase the size of the vulnerable window and, thus, lead to unidirectional block, as discussed in Section 4. This unidirectional block can then result in retrograde conduction and the initiation of reentry and, possibly, fibrillation.

6.2. Termination of fibrillation using shocks

VF is lethal within minutes and the only chance of survival for a patient is defibrillation using a defibrillator. This device creates a large electrical field across to the heart, after which the heart is hopefully be able to restart its normal sinus rhythm [282, 283]. Defibrillation can be applied using an external defibrillator or a implantable cardioverter defibrillator (ICD). The latter, used in patients that have a high risk of developing VF, can automatically detect a ventricular arrhythmia. Repeated shocks are, however, associated with an increase in mortality [284] and to limit the amount of shocks, ICDs apply an antitachycardia pacing (ATP) protocol to terminate detected VTs. In this case, the device delivers a train of stimuli to the heart and the idea is that the activation waves generated by the stimuli interfere with the tachycardia rhythm and take control of the tissue [285, 286]. Several different ATP algorithms are currently in use [287] and a recent study used personalized computational modeling to determine the efficacy of two of these algorithms [288].

The precise mechanism by which defibrillation works has long been a topic of discussion but it is clear that it has to affect the membrane potential far away from the electrodes of the defibrillating device. Applying an electric field in homogeneous tissue, however, would result in changes in the membrane potential that decay exponentially with distance x from the electrodes: $V \sim exp(-x/\lambda)$ [289]. Here, λ is the space constant of cardiac tissue, which is on the order of 1 mm. Thus, the applied electric field decays quickly, will be essentially negligible several millimeters away from the electrodes, and will not be able to affect the membrane potential in most of the tissue.

Over the last few decades, insights from modeling studies have provided plausible defibrillation scenarios. Crucial in these scenarios is the fact that cardiac tissue is not homogeneous but consists of cardiac cells that are coupled through gap junctions that have a higher resistance than the rest of the cell. The resulting heterogeneities, on the scale of the cell, can lead to oscillatory variations in the membrane potential that do not decay away from the defibrillator electrodes [290, 291, 292, 293]. This scenario is shown in Fig. 17A, where the membrane potential is computed in a cable comprised of cells with a high junctional resistance. Due to this junctional resistance, the membrane potential is not smoothly varying but, instead, has a characteristic sawtooth shape. For a sufficiently large shock, these oscillations can excite quiescent cells, which leads to additional propagating activation waves, even far away from the stimulus site. These waves can then interact with the irregular activation responsible for VF, leading to termination of all propagation.

The amount of energy delivered by a single shock from an external and an implantable defibrillator is approximately 150-360 J and 10-30 J, respectively. This large amount of energy is above the pain threshold for humans and can have deleterious effects [294]. Therefore, it would be advantageous to implement low-energy defibrillation techniques that are below the pain threshold and that are not harmful to the patient (for a recent review, see [295]). One of these techniques rely on the concept of so-called virtual electrodes [296, 297, 298, 299, 283]. These virtual electrodes arise from the difference in anisotropy between the intracellular domain (the cardiac cells) and the extracellular domain (the space surrounding the cells).

The appearance of virtual electrodes can be shown by simulating the bidomain equations, which describe the potential in the intracellular and in the extracellular domain (see Eqn. 14 in Section 3). The effect of the anisotropy ratio is illustrated in Fig. 17B. The upper panel shows the activation pattern following anodal stimulation in a piece of tissue with equal anisotropy ratio. This stimulation results in an ellipsoidal hyperpolarized region indicated by AN (anode) that will not result in tissue activation. Note that the observed pattern would be identical to the one obtained using the monodomain equation formulation (see Section 3).

For unequal anisotropy ratios, however, the bidomain equations will give a different polarization pattern for the same stimulus since the potential in the intra- and extracellular space will evolve differently. In particular, close to the stimulus, it is now possible to have regions that are both depolarized and hyperpolarized. This is shown in the lower panel of Fig. 17B: the anodal stimulus results not only in a hyperpolarized region (again labeled as AN) but also in two depolarized regions. These regions are called virtual electrodes (and in this case virtual cathodes and labeled as VC since the regions are depolarized) and can, for strong enough stimulation, result in tissue activation even in the case of an anodal stimulus. These virtual electrode patterns can occur during both onset and termination of the stimulation and for different electrode configurations and have been verified in multiple optical mapping experiments [300, 301, 302].

The fact that virtual electrodes can hyperpolarize or depolarize regions near a stimulation electrode can play a significant role in the success or failure of a defibrillating shock [299, 305]. Furthermore, the creation of virtual electrodes near obstacles can be used to lower the required energy for defibrillation. Specifically, simulation studies showed that the application of an electric field can induce regions of hyperpolarization and depolarization near an anatomical heterogeneity where the conductivity changes in a discontinuous manner. These studies also showed that the resulting activation sites were able to unpin a rotating wave anchored to this heterogeneity [306, 307]. Subsequent experimental work demonstrated that the required energy to unpin is significantly smaller than a defibrillating shock [308].

Pumir and Krinsky provided an analytical approach that showed how the depolarization or hyperpolarization near an obstacle depends on the applied electric field E_0 [306]. They linearized the monodomain equation around the resting potential, V_r, to obtain

$$\nabla^2 e - \frac{e}{\lambda^2} = 0 \tag{23}$$

where $e = V_m - V_r$, V_m is the membrane potential, and λ is the already encountered space constant. For a circular obstacle with radius R, it is possible to find a solution using the appropriate boundary conditions: $e(\mathbf{r}) \to 0$ when $|\mathbf{r}| \to \infty$ and $\nabla(e + E_0 \cdot \mathbf{r}) \cdot \mathbf{n} = 0$ on the boundary of the obstacle. The latter condition means that the current across the obstacle's boundary is zero, with $\mathbf{n}$ being its normal. The solution of this problem, expressed in polar coordinates (r, θ), is written in terms of Bessel functions:

$$e(\mathbf{r}) = -\frac{K_1(r/\lambda)}{K_1'(R/\lambda)}E_0\lambda cos(\theta) \qquad (24)$$

Thus, the maximum value of e is achieved at the boundary of the obstacle and increases for increasing values of *R*.

The scenario above focused on the appearance of a virtual electrode from a single obstacle. If the domain contains multiple discontinuities in conductivity, then a virtual electrode will appear at each of these discontinuities. For a sufficiently strong electric field, these virtual electrodes depolarize the tissue above the excitation threshold and can act as sites of activation. In that case, the additional activation waves can excite large portions of the domain, potentially extinguishing any existing propagating waves. Indeed, computational studies showed that the combination of small scale heterogeneities and an low energy electric field can effectively defibrillate cardiac tissue [303]. An example of this is shown in Fig. 17C, where spiral wave breakup was created in a square computational domain that contains multiple small and large non-conducting obstacles (panel 1). Electric field pulses resulted in the initiation of waves from the heterogeneities (panel 2 and 3) and the interaction with these waves and the original spiral waves led to the termination of any activation (panel 4).

Experimental studies, both *in vitro* and *in vivo* have tested the idea of low-energy defibrillation based on heterogeneity-induced virtual electrodes [309, 304]. These studies found that it is possible to terminate atrial and ventricular fibrillation using a limited number of shocks with an energy that is approximately 10% of the energy of a standard defibrillating shock. An example of the *in vivo* work is presented in Fig. 17D, which shows sequential snapshots of the optical mapping of AF in a dog before (upper row) and during (lower row) the delivery of low energy electric pulses. The pulses were able to create additional activation sites as is evident from the increase in size of the excited area in the lower row. After the last pulse, all activation terminated and the tissue became quiescent. Although a number of structural properties can act as the heterogeneities required for the generation of additional activation sites, including abrupt changes in the fiber orientation and fibrosis, the study by Luther *et al.* suggested that blood vessels are sufficient to explain the appearance of the additional activation sites [304].

6.3. Ablation treatments

It has become increasingly common to use ablation to treat a variety of cardiac arrhythmias. In this procedure, cardiac tissue is destroyed and rendered non-conductive, typically using either radiofrequency ablation, which burns cells, or cryoablation, which freezes cells. Ablation is used to treat relatively "simple arrhythmias", including supraventricular tachycardia and ventricular tachycardia but also the most complex heart rhythm disorder, fibrillation.

6.3.1. Ablation of AF: Pulmonary vein isolation—In the late 1990s, Haissaguerre and coworkers showed that ectopic beats are prevalent in and near the pulmonary veins of

AF patients [310]. Furthermore, these ectopic beats were shown to be able to initiate AF [311, 312]. Even though this initiation of AF nor the resulting AF were mapped in detail, it was reasonable to assume that the premature stimuli resulted in wave block and reentry (see Section 4). Therefore, to prevent the initiation of AF, clinicians started to electrically isolate the pulmonary veins from the atrium by catheter ablation in a procedure called pulmonary vein isolation (PVI). The primary goal PVI is thus not to terminate AF but to prevent the initiation of AF.

PVI has become the "cornerstone of AF ablation" and has grown into a multi-billion dollar market. The success of PVI, and any other procedure, is typically measured as the percentage of patients who remain AF free after one year. For PVI ablation, this success rate varies between studies and centers but has a higher success rate than other therapies, including antiarrhythmic drug therapy. Nevertheless, this success rate is still suboptimal. For example, a recent study reported that 63.9% of patients were AF free after 12 months, which dropped to 51.5% at 18 months [313]. Therefore, many patients require additional ablation procedures and it would be beneficial to search for alternative strategies.

6.3.2. Ablation of AF: targeted ablation—One such alternative strategy uses ablation to target the sites of rotational or focal activity [214]. Using the electrode basket described in Section 5, it is possible to pinpoint the location of the tips of spiral waves (see Fig. 16D) [267]. These tip locations can then be targeted using localized ablation, rendering the area of the spiral wave tip non-excitable. This technique was shown to be able to abruptly terminate AF in some patients [214, 267, 314]. Furthermore, this procedure also reported better long term outcomes than PVI ablation, although outcomes vary be center [214, 315]. The observed termination was perhaps surprising since it was thought that the creation of a non-excitable region may anchor spiral waves, resulting in waves that indefinitely rotate around the ablation spot. Using computational analysis, several possible mechanisms have been proposed to explain the success of this targeted ablation [316]. For example, it is possible that the ablation lesion connects the tip location to a non-excitable boundary, thus creating a line of block that prevents the spiral wave to continue its rotation. It is also possible that ablation removes a particular reentry path within the atrium, as shown in Fig. 18A-D. In this case, an isthmus between two nonconducting regions, indicated by the hatches in the figure, provides a conduction pathway and ablating this pathway will remove the reentry.

In addition, spatial heterogeneities in excitability in combination with ablation lesions, can play a role in the termination of reentry. In Fig. 18E&F we show two examples of this scenario where the excitability parameter in the Fenton-Karma model (τ_d) is varied in a radial fashion. In the first, a spiral wave is stably attached to a nonconducting zone and the excitability is higher close to this zone than in the surrounding tissue. Ablating the heterogeneous high-excitability domain results in a nonconducting zone, detachment of the spiral wave, and consequent migration and collision with anatomic obstacles, which are modeled as no-flux boundaries, and termination. In the second scenario, illustrated in Fig. 18F, a spiral wave is located in a region of low excitability surrounded by higher excitability. Initially, the activation front is anchored at a small, circular nonconducting obstacle. Creating an ablation lesion of larger radius results in the activation front propagating

in tissue with higher excitability and correspondingly higher wave speed, allowing the activation front and back to meet, leading to wave block (double bars in the right panel of Fig. 18F) and termination.

It is also possible to determine the effect of localized ablation using patient-specific atrial geometries that include areas of fibrosis, as was carried out in a recent computational study [211]. These fibrotic areas were determined using late gadolinium enhancement magnetic resonance imaging (LGE-MRI) [210]. This technique can visualize gadolinium-based contrast agents within the extracellular space of the myocardium, although its reproducibility and accuracy are still under investigation [317]. An example of the results of this imaging technique in a patient is shown in Fig. 18G, where the fibrotic regions are plotted in green. This computational study then applied virtual ablation targeted to these sites of fibrosis and continued to add additional lesions until AF was no longer inducible [211]. The lesions for this particular patient are shown in Fig. 18H as red dots and connect the region of fibrosis with a non-conducting boundary. As a proof of concept, this procedure was prospectively tested in a clinical setting with a limited number of patients, showing promising results [211].

6.3.3.   Ablation of VT and VF—Different forms of ventricular arrhythmias can also be treated with ablation. An example of a VT than can be ablated with a high success rate is the occurrence of supraventricular tachycardia, defined as a tachycardia that requires atrial or atrioventricular junctional tissue for its initiation and maintenance [318]. In the case of the Wolff-Parkinson-White (WPW) syndrome, for example, there is an auxiliary conduction path between the atrium and the ventricles, resulting in re-excitement of the atria after the ventricles have been activated. A clinical solution to this syndrome consists of removing this extra pathway through ablation using catheters, which has proven to be highly successful with an ablation success rate close to 100% [319, 320]. Once destroyed, the tissue is no longer conductive and re-activation of the atria is prevented.

Another type of VT that can be successfully targeted using ablation therapy is idiopathic VT. This VT is defined as a tachycardia in patients without structural heart disease or other plausible causes and is characterized by premature ventricular beats that occur in particular locations. Idiopathic VT is not considered life-threatening and precise mapping of the locations of these premature beats is possible. These locations can then be targeted by ablation in a procedure that has an acute success rate of approximately 85-90% and prevention of arrhythmia recurrence of about 75-80% [321].

In other cases, VT can be linked to the malfunctioning of ion channels (channelopathies). One example is the Brugada syndrome, a rare but life-threatening disease in young people with no structural heart disease that can be identified using ECG recordings [322, 323]. A number of mutations that affect different ion channels have been implicated in this disease, including the sodium channel. Although the primary treatment of this disease is the use of implantable cardiac defibrillators (ICDs), ablation has also been applied. In particular, it was found that certain regions in the right ventricular epicardium displayed abnormal electrograms. When these regions were ablated, VT or VF was no longer inducible nor recurred in the vast majority of patients [324, 325].

The examples of VT described above are relatively rare and the most common form of VT occurs in structurally diseased hearts. In these hearts, scar tissue and other abnormal structures have been formed as the result of disease or myocardial infarction [326]. These heterogeneities can create sites of local conduction slowing and block that can result in reentry and VT, and possibly VF [327]. In many of these patients, the arrhythmia is very stable over time and the reentry involves a narrow isthmus (as schematically shown in Fig. 18A). In that case, and if VT can be safely induced, it is possible to identify the reentry circuit without the need to map the entire activation pathway [328]. Even if VT can not be safely induced, it is still possible to locate the areas of scar tissue using substrate mapping [329]. In this case, the ventricles are mapped during sinus rhythm using an electrode and scar is identified as regions of low voltage or other electrogram characteristics. In either case, ablation of the identified sites can eliminate the reentry pathways and can thus terminate VT [330].

Even though VT ablation has been shown to more effective than drug therapy in patients with a previous myocardial infarction [331], its success rate is only modest, with a recurrence of 25%-50% based on long-term follow-up, mostly due to challenges associated with accurate mapping [332, 333]. Recent computational studies have attempted to guide VT ablation by constructing patient-specific computational models [334, 106]. These studies used magnetic resonance imaging data to construct personalized ventricular geometries and the regions of scar. The likelihood of VT initiation was assessed by stimulating from multiple locations. The optimal ablation lesion was then defined as the lesion which rendered VT non-inducible from any pacing location. The feasibility of this approach was demonstrated both retrospectively and, albeit in a small number of patients, prospectively [106].

Given the success of targeted ablation for AF based on basket electrode mapping, it is logical to ask if there is a role for this mapping based ablation procedure in VF. This could be especially useful in patients with structurally normal hearts that do not exhibit clear triggers. Mapping of VF, however, is much more challenging than for AF since a patient can only sustain VF for a few tens of seconds. Thus, focal or rotational sources need to be identified within a very short time window. Nevertheless, targeted ablation for VF was carried in a recent study that involved 6 patients with ICDs. [335]. These patients had experienced, on average, more than one ICD shocks per month prior to the procedure. In this study, VF was induced with rapid pacing and rotational and focal activation sites were mapped using 64-pole basket catheters. These sites were then targeted with ablation. The follow-up on these patients, for a duration of one year, revealed that the number of ICD shocks per month had drastically decreased to an average of 0.05 per month. These results suggest that sources can be identified and ablated, even when VF can only be mapped for a short amount of time.

6.4. Control of fibrillation

A number of alternative options have been proposed to treat fibrillation. Most of these options are based on theoretical and computational studies and have not yet been implemented in clinics. One proposed treatment option attempts to use control theory to

prevent alternans from occurring. As discussed in Section 4, alternans manifests itself in APDs or Ca^{2+} signals that alternate between long and short and can also materialize at a spatial scale. Focusing on electrical alternans, we can write the restitution curve (see Fig. 5) as $APD_{n+1} = f(APD_n, T)$, where APD_i is the action potential duration of the i-th beat and where T is the pacing period. For restitution curves with a slope larger than one, we saw that the fixed point of this recurrence map is unstable. Employing a feedback control scheme, however, that changes the pacing period in a judicious way, makes it possible to drive the system to its stable fixed point. For example, replacing the pacing period at each cycle to $T - \frac{\alpha}{2}(APD_n - APD_{n-1})$, results in the following 2D map

$$APD_{n+1} = f(APD_n, T - \frac{\alpha}{2}(APD_n - Y_n))$$
$$Y_{n+1} = APD_n \qquad (25)$$

The fixed point of this system, $APD^* = Y^*$ is stable as long as

$$\frac{|A| - 1}{|B|} < \alpha < \frac{2}{|B|} \qquad (26)$$

where $A = \frac{\partial f}{\partial APD}$ and $B = \frac{\partial f}{\partial T}$ [336]. This and other control schemes have been shown to be successful in computational and small scale *in vitro* systems although adding the dynamics of Ca^{2+} may make it more difficult to achieve adequate control [336, 337, 338, 339, 340, 341, 342].

The heart is, of course, a spatially extended system and the control of spatio-temporal instabilities arising from alternans is more challenging [343]. A computational study investigated the break up of a spiral wave in the presence of equally spaced control points [344]. It showed that applying a feedback current at these discrete points during the repolarizing phase of the action potential could suppress alternans and, therefore, prevent spiral wave break up. It also determined that the success of the control scheme critically depends on two factors: the amplification time of the instability of spiral wave break up and the electrode spacing. For successful control, the amplification time needs to be larger than the time required for control and the the electrode spacing must be comparable or smaller than the spiral wavelength. These factors, in addition to other practical issues, make it difficult to apply this control scheme to *in vivo* settings. Interestingly, a recent study showed that a proprietary closed-loop system was able to significantly suppress the amplitude of alternans voltage in swine hearts [345]. Furthermore, this study showed a trend toward reduced arrhythmia susceptibility in the presence of control. It would be interesting to further understand the mechanisms that underlie these results.

6.5. Termination as a Stochastic Process

The termination of AF by targeted ablation is often not instantaneous. Instead, termination can take minutes to days [346], suggesting that the dynamical state following ablation is transient. This is consistent with the clinical picture of paroxysmal AF, defined as AF with intermittent episodes of variable duration. In addition, spontaneous termination of

ventricular arrhythmias has also been reported [347, 348, 349]. These observations illustrate that fibrillation can terminate spontaneously and can, thus, have a finite lifetime [350, 351]. This dynamics is consistent with spiral defect chaos (SDC), present in a variety of different pattern-forming systems that exhibit spiral waves [352, 353, 354, 355, 356, 357, 358, 359, 360]. During SDC, spiral waves continuously break down to form new ones, and are removed through collisions with other spiral waves or with non-conducting boundaries. The resulting stochastic competition between creation and annihilation persists until the last spiral wave is terminated and the duration of SDC is therefore a stochastic quantity. If SDC underlies fibrillation, then its mean episode duration τ would be an important quantity for fibrillation management and therapy. This would be particularly the case for AF where computing τ in the presence of different lesion sets may be an important step towards more efficient AF therapies [361, 104].

The mean episode duration τ can be computed using direct simulations of the standard equation for membrane potential (Eq. 8). These simulations use random initial conditions and are continued until the last spiral wave has been annihilated. Repeating this many times, starting with different and independent initial conditions, results in a distribution of termination times, T_t, from which τ can be estimated by simple averaging. Simulations using several different electrophysiological models revealed that this distribution is exponentially distributed: $P(T_t) = \dfrac{e^{-T_t / \tau}}{\tau}$. Thus, spiral wave termination can be well described as a Poisson process, with a mean episode duration given by τ [362, 363]. These results are in agreement with a recent study which showed that phase singularities, corresponding to spiral wave tips, are exponentially distributed in human AF and animal models [363].

Computing τ using direct simulations of cardiac models, however, is challenging because a statistically significant determination of this stochastic quantity requires simulating a large number of independent termination events and is computationally expensive. An additional complication comes from the fact that numerical studies have shown that τ increases sharply as a function of the system size [364, 365, 362]. This is shown in Fig. 19A where τ is plotted as a function of the domain size A as red symbols. The mean episode duration increases exponentially with the domain size and the results show that doubling the size of the computational domain from, for example, 20 cm^2 to 40 cm^2, will result in an increase in τ of more than one order of magnitude.

To estimate τ for large values of A, it is convenient to develop a statistical description of the number of spiral tips as a function of time, by quantifying the birth and death rates of spiral waves using a limited set of direct numerical simulations. The dynamics of SDC, and thus fibrillation, can then be cast into the form of a master equation, which can be solved using a number of techniques, exact and approximate, from the fields of theoretical ecology and population dynamics. This master equation describes the probability $P(n, t)$ of having n spiral tips at time t as

$$\frac{dP(n,t)}{dt} = \sum_r [W_r(n-r)P(n-r,t) - W_r(n)P(n,t)] \tag{27}$$

where W_r are transition rates for the number of spiral tips to change by r tips and can be computed directly from spatially extended simulations of cardiac models [362]. In the simulations, tips are created and annihilated either as pairs or as singlets. Therefore, the only possible values of r in the master equation are $r = \pm 1, \pm 2$. Furthermore, once $n = 0$, all tips are eliminated and the simulation is stopped. This means that $n = 0$ is an absorbing boundary and $W_r(0) = 0$.

In a typical simulation, the number of collisions between tips increases for increasing values of n and the death rate will become larger than the birth rate. Conversely, for small values of n, the birth rate will exceed the death rate. As a result, the system will develop a quasi-stationary long-lived metastable state with a mean number of tips $n*$, together with a quasi-stationary distribution $P_{qs}(n)$ [366, 367]. Of course, the stationary distribution trivially corresponds to $P(n) = 0$ for all n 0 and $P(0) = 1$ due to the absorbing boundary condition at $n = 0$. In this quasi-stationary state, n fluctuates around $n*$ for long times and termination will occur when a large fluctuation away from $n*$ drives the system towards $n = 0$.

For this statistical physics approach, it is necessary to compute the transition rates using direct simulations. The results for the FK model are shown in Fig. 19B&C, where the rates were computed for several different 2D computational domain sizes. These simulations considered periodic boundary conditions, such that spiral wave tips can only be created or annihilated in pairs. These simulations revealed that for large area A all rates collapse onto a single curve when plotted as a function of the density $q = n/A$. More precisely, the simulations revealed that the $W_{\pm 2}$ rates only depend on the density and scale as $W_{\pm 2}(n) \sim A w_{\pm 2}(q)$ (Figs. 19D). In other words, the tips are well-mixed. Similar scaling can be found for simulations with non-conducting boundaries and for different electrophysiological models [362].

Once the transition rates are computed, it is possible to construct a transition matrix, Q, with elements Q_{ij} that represent the probability of transitioning from state i to state j [368]. The transition matrix can be used to compute the so-called fundamental matrix $N = I + Q + Q^2 + \ldots = (I - Q)^{-1}$, where I is the identity matrix. The entry N_{ij} corresponds to the mean time the system will be in state j given an initial state i. The mean episode duration τ can then be computed as $N \vec{e}$, where $\vec{e}$ is a column vector of ones. An example of the results using this approach is shown as black symbols in Fig. 19A. The values of τ obtained with this master equation approach agree well with the ones obtained from direct simulations. Importantly, however, constructing the transition matrix only requires values of the transition rates, which can be obtained in simulations of limited duration through interpolation. Thus, this approach allows one to estimate the mean episode duration for system sizes where determination of this quantity using simulations of the full model is prohibitively expensive [362].

The exponential dependence of τ on A can also be derived using approximation techniques. For periodic boundary conditions, one can write down an analytical expression for τ [369]:

$$\tau(n_0) = \sum_{k=1}^{n_0/2} \phi(2(k-1)) \sum_{j=k}^{\infty} \frac{1}{\phi(2j)W_{+2}(2j)} \tag{28}$$

In this expression, n_0 is the initial number of spiral tips, $\phi(k) = \prod_{i=1}^{k/2} W_{-2}(2i) / W_{+2}(2i)$, and $\phi(0) \equiv 1$. Using the fact that the quasi-stationary distribution of n is peaked at n^* one can derive an approximate expression for τ [362]:

$$\tau \sim \exp\left[A \int_{2/A}^{q^*} \ln\sqrt{\frac{w_{+2}(s)}{w_{-2}(s)}} ds \right] \quad (29)$$

This expression is written in terms of the scaled quantities q and $w_\pm$ and shows that τ scales exponentially with the area, consistent with the direct numerical results (solid line Fig. 19A). For non-periodic boundary conditions, it is still possible to to determine the scaling of the mean episode duration. In this case, one can use a dissipative WKB approximation, pioneered by Kubo et al. [370], and further explored in more recent studies [366, 367]. Again, one finds that the mean episode duration scales exponentially with the domain size [362].

The stochastic description of spiral wave dynamics not only explains the diversity in observed episode durations of fibrillation, it is also consistent with the so-called critical mass hypothesis [371, 365, 372]. Based upon observations of fibrillation in animals, this hypothesis states that fibrillation can only be sustained in hearts larger than some critical size. This theory formed the rationale behind the surgical Cox-Maze procedure, during which the atria is subdivided into small compartments by a set of incisions [373] and which has shown good success rates in eliminating AF [374]. From a stochastic point of view, this hypothesis makes sense because with less tissue for the wavelets to traverse, collisions are increasingly likely which will cause the mean episode duration to become negligible.

Recently, the stochastic termination of spiral wave dynamics in cardiac tissue was also observed *in vivo* in AF patients. The spiral wave activity in these patients was mapped and the locations of spiral wave sources was targeted using radiofrequency ablation [314]. This study found that targeted ablation was able to terminate AF, but only after a variable delay of up to several minutes and that termination was not accompanied by gradual temporal or spatial organization. These results were modeled by simulating a heterogeneity that harbored a stable spiral wave, surrounded by spiral wave breakup. The virtual ablation of this heterogeneity, and thus the stable spiral wave, resulted in SDC. As described above, the eventual termination was stochastic and Poisson-distributed and the dynamics were accurately described by a master equation using birth and death rates [314]. Thus, spiral waves near heterogeneities can be a driving source of AF and the removal of these sources will result in SDC, which has a finite lifetime. This suggests that eliminating spiral wave sources may be a viable treatment option for AF.

7. Outlook

As is hopefully clear after reading this review, cardiac arrhythmias in general and cardiac fibrillation in particular are disease types that involve events on multiple spatial and temporal scales. Furthermore, they can be described by the dynamics of spatially extended systems and lend themselves to a variety of modeling approaches. In fact, it

is fair to say that some of the most important concepts and mechanisms underlying arrhythmias were first hypothesized or demonstrated in theoretical studies. These include the concepts of vulnerable window, spiral wave dynamics, wave break, spiral wave instabilities, and alternans. These concepts were and continue to be delineated in a vast body of computational and theoretical work, which exists in addition to the vast clinical literature in cardiology.

Despite the large amount of research dedicated to arrhythmias, most of the mechanisms are still poorly understood, preventing better therapeutic interventions. Part of the reason behind this lack of understanding are the challenges of imaging arrhythmias and fibrillation in humans. Current mapping methodologies, as reviewed in Section 5, have significant shortcomings. They are either unable to visualize arrhythmias during procedures, have limited spatial or temporal resolution, or produce data that are very noisy and hard to interpret. It will therefore be of paramount importance to develop better mapping techniques that are safe and that can visualize activation patterns with high spatial and temporal resolution. This development will most likely involve additional computational and theoretical advances and will be necessary to further our understanding of cardiac arrhythmias. New imaging techniques may also resolve some of the existing controversies in the field, including whether or not spiral waves drive human fibrillation.

A number of novel and promising directions in the field of modeling cardiac arrhythmias can be identified. Some of these directions have been made possible in part by the increase in raw computational power. It is now possible to simulate cardiac propagation patterns in 3D in near real time [116]. This increase in computational power, coupled with imaging techniques that can determine the geometry and tissue fibrosis, have contributed to the development of patient-specific models as a new direction to tackle heart rhythm disorders. Preliminary results using these models to guide ablation in AF patients, for example, show promising results [211]. It remains to be seen, however, if this modeling strategy will result in further insights and whether it can be applied on a large scale. Additionally, the quantification of the heart's geometry, its electrophysiological heterogeneity, fiber directions, and fibrotic regions are essential in these patient-specific models but remain challenging. This is especially true for the atria, where the thin walls pose significant segmentation challenges. Regardless, patient-specific mechanistic modeling has started to make inroads into clinical practice, and it is likely that this type of modeling will become more common in the near future [375].

Another new modeling direction is the use of machine learning and artificial intelligence. As in almost any other field of science, artificial intelligent approaches are becoming more common and are used to, for example, better determine the location of spiral waves, guide targeted ablation, suggest the optimal treatment option for individual patients, and predict patient susceptibility to heart rhythm disorders [376, 377, 378]. As the data sets become larger, these techniques are expected to have a positive impact on the field of cardiology.

Recently, efforts are under way to combine these two new directions to create so-called cardiac "digital twins". Such twins are *in-silico* replicas of patient hearts that have as goal to match as much of the available clinical data as possible [379]. It may be feasible in the

future to use these twins to gain insights into mechanisms, to guide treatments, and even to run "virtual" trails [109]. In that case, collaborative studies between modelers and clinicians could potentially be able to develop novel and more adequate treatment options.

Acknowledgements

References

[1]. Centers for Disease Control and Prevention, Mortality 1999-2020 on cdc wonder online database, released in 2021, https://wonder.cdc.gov/Deaths-by-Underlying-Cause.html.

[2]. World Health Organization, The top 10 causes of death, https://www.who.int/news-room/fact-sheets/detail/the-top-10-causes-of-death.

[3]. Fryar CD, Chen T-C, Li X, Prevalence of uncontrolled risk factors for cardiovascular disease: United States, 1999-2010, no. 103, US Department of Health and Human Services, Centers for Disease Control and Prevention, National Center for Health Statistics, 2012.

[4]. Adabag AS, Luepker RV, Roger VL, Gersh BJ, Sudden cardiac death: epidemiology and risk factors, Nature Reviews Cardiology 7 (4) (2010) 216–225. [PubMed: 20142817]

[5]. Katz A, Physiology of the heart, Raven Press, New York, 1992.

[6]. Klabunde R, Cardiovascular physiology concepts, Lippincott Williams & Wilkins, 2011.

[7]. Herring N, Paterson DJ, Levick's introduction to cardiovascular physiology, CRC Press, 2018.

[8]. Betts JG, Desaix P, Johnson J, Korol O, Kruse D, Poe B, Wise J, Womble M, Young K, Openstax college, et al. anatomy and physiology, Tech. rep, ISBN 1-938168-13-5: 787–846 (2013).

[9]. Boyett MR, Honjo H, Kodama I, The sinoatrial node, a heterogeneous pacemaker structure, Cardiovascular research 47 (4) (2000) 658–687. [PubMed: 10974216]

[10]. Irisawa H, Brown H, Giles W, Cardiac pacemaking in the sinoatrial node, Physiological reviews 73 (1) (1993) 197–227. [PubMed: 8380502]

[11]. Rohr S, Role of gap junctions in the propagation of the cardiac action potential, Cardiovascular research 62 (2) (2004) 309–322. [PubMed: 15094351]

[12]. Evans WH, Martin PE, Gap junctions: structure and function (review), Molecular membrane biology 19 (2) (2002) 121–136. [PubMed: 12126230]

[13]. Bers D, Cardiac excitation-contraction coupling, Nature 415 (2002) 198–205. [PubMed: 11805843]

[14]. Betts JG, et al., Anatomy & physiology.(2013), Open Stax College.

[15]. Kupersmith J, Krongrad E, Waldo AL, Conduction intervals and conduction velocity in the human cardiac conduction system: studies during open-heart surgery, Circulation 47 (4) (1973) 776–785. [PubMed: 4696799]

[16]. Ho SY, Anatomy and myoarchitecture of the left ventricular wall in normal and in disease, European Journal of Echocardiography 10 (8) (2009) iii3–iii7. [PubMed: 19889656]

[17]. Whitaker J, Rajani R, Chubb H, Gabrawi M, Varela M, Wright M, Niederer S, O'Neill MD, The role of myocardial wall thickness in atrial arrhythmogenesis, EP Europace 18 (12) (2016) 1758–1772.

[18]. Bootman MD, Higazi DR, Coombes S, Roderick HL, Calcium signalling during excitation-contraction coupling in mammalian atrial myocytes, Journal of cell science 119 (19) (2006) 3915–3925. [PubMed: 16988026]

[19]. Roux B, Ion conduction and selectivity in K+ channels, Annu. Rev. Biophys. Biomol. Struct 34 (2005) 153–171. [PubMed: 15869387]

[20]. Roden DM, Balser JR, George AL Jr, Anderson ME, Cardiac ion channels, Annual review of physiology 64 (1) (2002) 431–475.

[21]. Grant AO, Cardiac ion channels, Circulation: Arrhythmia and Electrophysiology 2 (2) (2009) 185–194. [PubMed: 19808464]

[22]. Plonsey R, Barr R, Bioelectricity: a quantitative approach, Plenum Press, New York, 1988.

[23]. Bullock T, Horridge GA, Structure and function in the nervous systems of invertebrates., Freeman San Francisco, 1965.

[24]. Aquila LA, McCarthy PM, Smedira NG, Young JB, Moravec CS, Cytoskeletal structure and recovery in single human cardiac myocytes, The Journal of heart and lung transplantation 23 (8) (2004) 954–963. [PubMed: 15312825]

[25]. Rudy Y, Ackerman MJ, Bers DM, Clancy CE, Houser SR, London B, McCulloch AD, Przywara DA, Rasmusson RL, Solaro RJ, et al. , Systems approach to understanding electromechanical activity in the human heart, Circulation 118 (11) (2008) 1202–1211. [PubMed: 18779456]

[26]. Eisner DA, Caldwell JL, Kistamás K, Trafford AW, Calcium and excitation-contraction coupling in the heart, Circulation research 121 (2) (2017) 181–195. [PubMed: 28684623]

[27]. Sweeney HL, Houdusse A, Structural and functional insights into the myosin motor mechanism, Annual review of biophysics 39 (2010) 539–557.

[28]. Fabiato A, Time and calcium dependence of activation and inactivation of calcium-induced release of calcium from the sarcoplasmic reticulum of a skinned canine cardiac purkinje cell., The Journal of general physiology 85 (2) (1985) 247–289. [PubMed: 2580043]

[29]. Marx SO, Marks AR, Dysfunctional ryanodine receptors in the heart: new insights into complex cardiovascular diseases, Journal of molecular and cellular cardiology 58 (2013) 225–231. [PubMed: 23507255]

[30]. Blayney LM, Lai FA, Ryanodine receptor-mediated arrhythmias and sudden cardiac death, Pharmacology & therapeutics 123 (2) (2009) 151–177. [PubMed: 19345240]

[31]. Zalk R, Lehnart SE, Marks AR, Modulation of the ryanodine receptor and intracellular calcium, Annu. Rev. Biochem 76 (2007) 367–385. [PubMed: 17506640]

[32]. Zalk R, Clarke OB, Des Georges A, Grassucci RA, Reiken S, Mancia F, Hendrickson WA, Frank J, Marks AR, Structure of a mammalian ryanodine receptor, Nature 517 (7532) (2015) 44–49. [PubMed: 25470061]

[33]. Marks AR, Ryanodine receptors/calcium release channels in heart failure and sudden cardiac death, Journal of molecular and cellular cardiology 33 (4) (2001) 615–624. [PubMed: 11273716]

[34]. Dobrev D, Wehrens XH, Role of RyR2 phosphorylation in heart failure and arrhythmias: controversies around ryanodine receptor phosphorylation in cardiac disease, Circulation research 114 (8) (2014) 1311–1319. [PubMed: 24723656]

[35]. Taggart P, Sutton PM, Opthof T, Coronel R, Trimlett R, Pugsley W, Kallis P, Inhomogeneous transmural conduction during early ischaemia in patients with coronary artery disease, Journal of molecular and cellular cardiology 32 (4) (2000) 621–630. [PubMed: 10756118]

[36]. Kotadia I, Whitaker J, Roney C, Niederer S, O'Neill M, Bishop M, Wright M, Anisotropic cardiac conduction, Arrhythmia & Electrophysiology Review 9 (4) (2020) 202. [PubMed: 33437488]

[37]. Spach MS, Miller W 3rd, Geselowitz DB, Barr RC, Kootsey JM, Johnson EA, The discontinuous nature of propagation in normal canine cardiac muscle. evidence for recurrent discontinuities of intracellular resistance that affect the membrane currents., Circulation research 48 (1) (1981) 39–54. [PubMed: 7438345]

[38]. Saffitz JE, Kanter HL, Green KG, Tolley TK, Beyer EC, Tissue-specific determinants of anisotropic conduction velocity in canine atrial and ventricular myocardium., Circulation research 74 (6) (1994) 1065–1070. [PubMed: 8187276]

[39]. LeGrice IJ, Smaill B, Chai L, Edgar S, Gavin J, Hunter PJ, Laminar structure of the heart: ventricular myocyte arrangement and connective tissue architecture in the dog, American Journal of Physiology-Heart and Circulatory Physiology 269 (2) (1995) H571–H582.

[40]. Costa KD, May-Newman K, Farr D, O'Dell WG, McCulloch AD, Omens JH, Three-dimensional residual strain in midanterior canine left ventricle, American Journal of Physiology-Heart and Circulatory Physiology 273 (4) (1997) H1968–H1976.

[41]. Basser PJ, Mattiello J, LeBihan D, MR diffusion tensor spectroscopy and imaging, Biophysical journal 66 (1) (1994) 259–267. [PubMed: 8130344]

[42]. Lombaert H, Peyrat J-M, Croisille P, Rapacchi S, Fanton L, Cheriet F, Clarysse P, Magnin I, Delingette H, Ayache N, Human atlas of the cardiac fiber architecture: study on a healthy population, IEEE transactions on medical imaging 31 (7) (2012) 1436–1447. [PubMed: 22481815]

[43]. Rohmer D, Sitek A, Gullberg GT, Reconstruction and visualization of fiber and sheet structure with regularized tensor diffusion mri in the human heart, Lawrence Berkeley National Laboratory Publication. LBNL-60277 (2006) 25.

[44]. Pashakhanloo F, Herzka DA, Ashikaga H, Mori S, Gai N, Bluemke DA, Trayanova NA, McVeigh ER, Myofiber architecture of the human atria as revealed by submillimeter diffusion tensor imaging, Circulation: arrhythmia and electrophysiology 9 (4) (2016) e004133. [PubMed: 27071829]

[45]. Henriquez CS, A brief history of tissue models for cardiac electrophysiology, IEEE Transactions on Biomedical Engineering 61 (5) (2014) 1457–1465. [PubMed: 24759278]

[46]. Nash MP, Panfilov AV, Electromechanical model of excitable tissue to study reentrant cardiac arrhythmias, Progress in biophysics and molecular biology 85 (2-3) (2004) 501–522. [PubMed: 15142759]

[47]. Augustin CM, Fastl TE, Neic A, Bellini C, Whitaker J, Rajani R, O'Neill MD, Bishop MJ, Plank G, Niederer SA, The impact of wall thickness and curvature on wall stress in patient-specific electromechanical models of the left atrium, Biomechanics and modeling in mechanobiology 19 (3) (2020) 1015–1034. [PubMed: 31802292]

[48]. Niederer SA, Campbell KS, Campbell SG, A short history of the development of mathematical models of cardiac mechanics, Journal of molecular and cellular cardiology 127 (2019) 11–19. [PubMed: 30503754]

[49]. Hodgkin AL, Huxley AF, A quantitative description of membrane current and its application to conduction and excitation in nerve, J Physiol (Lond) 117 (1952) 500–544. [PubMed: 12991237]

[50]. Fenton FH, Cherry EM, Models of cardiac cell, Scholarpedia 3 (8) (2008) 1868.

[51]. Ten Tusscher K, Noble D, Noble P, Panfilov A, A model for human ventricular tissue, American Journal of Physiology-Heart and Circulatory Physiology 286 (4) (2004) H1573–H1589. [PubMed: 14656705]

[52]. Iyer RMV, Winslow RL, A computational model of the human left-ventricular epicardial myocyte, Biophys J 87 (2004) 1507–1525. [PubMed: 15345532]

[53]. Grandi E, Pasqualini FS, Bers DM, A novel computational model of the human ventricular action potential and ca transient, Journal of molecular and cellular cardiology 48 (1) (2010) 112–121. [PubMed: 19835882]

[54]. Courtemanche M, Ramirez RJ, Nattel S, Ionic mechanisms underlying human atrial action potential properties: insights from a mathematical model, Am J Physiol 275 (1 Pt 2) (1998) H301–H321. [PubMed: 9688927]

[55]. Nygren A, Fiset C, Firek L, Clark JW, Lindblad DS, Clark RB, Giles WR, Mathematical model of an adult human atrial cell: the role of K+ currents in repolarization, Circ Res 82 (1) (1998) 63–81. [PubMed: 9440706]

[56]. Koivumaki JT, Korhonen T, Tavi P, Impact of sarcoplasmic reticulum calcium release on calcium dynamics and action potential morphology in human atrial myocytes: a computational study, PLoS Comput. Biol 7 (1) (2011) e1001067. [PubMed: 21298076]

[57]. Balser JR, Roden DM, Bennett PB, Global parameter optimization for cardiac potassium channel gating models, Biophysical journal 57 (3) (1990) 433–444. [PubMed: 2306494]

[58]. Clancy CE, Rudy Y, Linking a genetic defect to its cellular phenotype in a cardiac arrhythmia, Nature 400 (1999) 566–569. [PubMed: 10448858]

[59]. Clancy CE, Rudy Y, Cellular consequences of HERG mutations in the long QT syndrome: precursors to sudden cardiac death, Cardiovasc Res 50 (2001) 301–313. [PubMed: 11334834]

[60]. Moreno JD, Zhu ZI, Yang P-C, Bankston JR, Jeng M-T, Kang C, Wang L, Bayer JD, Christini DJ, Trayanova NA, et al. , A computational model to predict the effects of class I antiarrhythmic drugs on ventricular rhythms, Science translational medicine 3 (98) (2011) 98ra83–98ra83.

[61]. Fink M, Noble D, Markov models for ion channels: versatility versus identifiability and speed, Philosophical Transactions of the Royal Society A: Mathematical, Physical and Engineering Sciences 367 (1896) (2009) 2161–2179.

[62]. Carbonell-Pascual B, Godoy E, Ferrer A, Romero L, Ferrero JM, Comparison between Hodgkin–Huxley and Markov formulations of cardiac ion channels, Journal of theoretical biology 399 (2016) 92–102. [PubMed: 27059892]

[63]. Moe GK, Rheinboldt WC, Abildskov J, A computer model of atrial fibrillation, American heart journal 67 (2) (1964) 200–220. [PubMed: 14118488]

[64]. Winfree AT, Varieties of spiral wave behavior: An experimentalist's approach to the theory of excitable media, Chaos 1 (1991) 303–334. [PubMed: 12779929]

[65]. FitzHugh R, Mathematical models of threshold phenomena in the nerve membrane, The bulletin of mathematical biophysics 17 (4) (1955) 257–278.

[66]. Nagumo J, Arimoto S, Yoshizawa S, An active pulse transmission line simulating nerve axon, Proc. IRE 50 (1962) 2061–2070.

[67]. FitzHugh R, Impulses and physiological states in theoretical models of nerve membrane, Biophys. J 1 (1961) 445–446. [PubMed: 19431309]

[68]. Koch C, Biophysics of computation: information processing in single neurons, Oxford university press, 2004.

[69]. Cronin J, Boutelle JC, Mathematical aspects of Hodgkin-Huxley neural theory, Cambridge University Press, 1987.

[70]. Fenton F, Karma A, Vortex dynamics in three-dimensional continuous myocardium with fiber rotation: Filament instability and fibrillation, Chaos 8 (1998) 20–47. [PubMed: 12779708]

[71]. Cherry EM, Fenton FH, A tale of two dogs: analyzing two models of canine ventricular electrophysiology, American Journal of Physiology-Heart and Circulatory Physiology 292 (1) (2007) H43–H55. [PubMed: 16997886]

[72]. Bueno-Orovio A, Cherry EM, Fenton FH, Minimal model for human ventricular action potentials in tissue, J. Theor. Biol 253 (3) (2008) 544–560. [PubMed: 18495166]

[73]. Lombardo DM, Fenton FH, Narayan SM, Rappel W-J, Comparison of detailed and simplified models of human atrial myocytes to recapitulate patient specific properties, PLoS Comput Biol 12 (8) (2016) e1005060. [PubMed: 27494252]

[74]. Ino T, Karagueuzian HS, Hong K, Meesmann M, Mandel WJ, Peter T, Relation of monophasic action potential recorded with contact electrode to underlying transmembrane action potential properties in isolated cardiac tissues: a systematic microelectrode validation study, Cardiovascular research 22 (4) (1988) 255–264. [PubMed: 3197056]

[75]. Iravanian S, Uzelac I, Herndon C, Langberg JJ, Fenton FH, Generation of monophasic action potentials and intermediate forms, Biophysical Journal 119 (2) (2020) 460–469. [PubMed: 32645291]

[76]. Beeler GW, Reuter H, Reconstruction of the action potential of ventricular myocardial fibres, J Physiol 268 (1977) 177–210. [PubMed: 874889]

[77]. Luo CH, Rudy Y, A model of the ventricular cardiac action potential. Depolarization, repolarization, and their interaction, Circ Res 68 (1991) 1501–1526. [PubMed: 1709839]

[78]. Girouard SD, Pastore JM, Laurita KR, Gregory KW, Rosenbaum DS, Optical mapping in a new guinea pig model of ventricular tachycardia reveals mechanisms for multiple wavelengths in a single reentrant circuit, Circulation 93 (3) (1996) 603–613. [PubMed: 8565181]

[79]. Franz MR, The electrical restitution curve revisited, Journal of cardiovascular electrophysiology 14 (s10) (2003) S140–S147. [PubMed: 14760916]

[80]. Franz MR, Schaefer J, Schöttler M, Seed WA, Noble MI, Electrical and mechanical restitution of the human heart at different rates of stimulation., Circulation Research 53 (6) (1983) 815–822. [PubMed: 6640866]

[81]. Panfilov A, Zemlin C, Wave propagation in an excitable medium with a negatively sloped restitution curve, Chaos: An Interdisciplinary Journal of Nonlinear Science 12 (3) (2002) 800–806.

[82]. Qu Z, Weiss JN, Garfinkel A, Spatiotemporal chaos in a simulated ring of cardiac cells, Physical Review Letters 78 (7) (1997) 1387.

[83]. Lombardo DM, Rappel W-J, Systematic reduction of a detailed atrial myocyte model, Chaos: An Interdisciplinary Journal of Nonlinear Science 27 (9) (2017) 093914.

[84]. Rall W, Core conductor theory and cable properties of neurons, Comprehensive physiology.

[85]. Keener JP, Sneyd J, Mathematical physiology, Vol. 1, Springer, 1998.

[86]. Tyson JJ, Keener JP, Singular perturbation theory of traveling waves in excitable media (a review), Physica D: Nonlinear Phenomena 32 (3) (1988) 327–361.

[87]. Fenton FH, Cherry EM, Hastings HM, Evans SJ, Multiple mechanisms of spiral wave breakup in a model of cardiac electrical activity, Chaos 12 (2002) 852–892. [PubMed: 12779613]

[88]. Rappel W-J, Filament instability and rotational tissue anisotropy: A numerical study using detailed cardiac models, Chaos 11 (2001) 71–80. [PubMed: 12779442]

[89]. Collins J, Levine H, Diffusion interface model of diffusion-limited crystal growth., Phys. Rev. B 31 (9) (1985) 6118–22.

[90]. Karma A, Rappel W-J, Quantitative phase-field modeling of dendritic growth in two and three dimensions, Phys Rev E 57 (1998) 4323–4349.

[91]. Kockelkoren J, Levine H, Rappel W-J, Computational approach for modeling intra- and extracellular dynamics, Phys Rev E 68 (3) (2003) 037702.

[92]. Ziebert F, Swaminathan S, Aranson IS, Model for self-polarization and motility of keratocyte fragments, Journal of The Royal Society Interface 9 (70) (2012) 1084–1092. [PubMed: 22012972]

[93]. Fenton FH, Cherry EM, Karma A, Rappel W-J, Modeling wave propagation in realistic heart geometries using the phase-field method, Chaos 15 (1) (2005) 13502. [PubMed: 15836267]

[94]. Karma A, Kessler D, Levine H, Phase-field model of mode III dynamic fracture., Phys Rev Lett 87 (4) (2001) 045501. [PubMed: 11461627]

[95]. Shao D, Levine H, Rappel WJ, Coupling actin flow, adhesion, and morphology in a computational cell motility model, Proc Natl Acad Sci U S A.

[96]. Rogers JM, McCulloch AD, A collocation-Galerkin finite element model of cardiac action potential propagation, IEEE Transactions on Biomedical Engineering 41 (8) (1994) 743–757. [PubMed: 7927397]

[97]. Vigmond EJ, Aguel F, Trayanova NA, Computational techniques for solving the bidomain equations in three dimensions, IEEE Transactions on Biomedical Engineering 49 (11) (2002) 1260–1269. [PubMed: 12450356]

[98]. Gonzales MJ, Sturgeon G, Krishnamurthy A, Hake J, Jonas R, Stark P, Rappel W-J, Narayan SM, Zhang Y, Segars WP, McCulloch AD, A three-dimensional finite element model of human atrial anatomy: new methods for cubic Hermite meshes with extraordinary vertices, Med Image Anal 17 (5) (2013) 525–537. [PubMed: 23602918]

[99]. Harrild D, Henriquez C, A computer model of normal conduction in the human atria, Circ Res 87 (2000) E25–E36. [PubMed: 11009627]

[100]. Jacquemet V, Henriquez CS, Finite volume stiffness matrix for solving anisotropic cardiac propagation in 2-D and 3-D unstructured meshes, IEEE transactions on biomedical engineering 52 (8) (2005) 1490–1492. [PubMed: 16119246]

[101]. Krueger MW, Schmidt V, Tobón C, Weber FM, Lorenz C, Keller DU, Barschdorf H, Burdumy M, Neher P, Plank G, et al., Modeling atrial fiber orientation in patient-specific geometries: a semi-automatic rule-based approach, in: International Conference on Functional Imaging and Modeling of the Heart, Springer, 2011, pp. 223–232.

[102]. Saliani A, Tsikhanovich A, Jacquemet V, Visualization of interpolated atrial fiber orientation using evenly-spaced streamlines, Computers in biology and medicine 111 (2019) 103349. [PubMed: 31301635]

[103]. Roney CH, Bendikas R, Pashakhanloo F, Corrado C, Vigmond EJ, McVeigh ER, Trayanova NA, Niederer SA, Constructing a human atrial fibre atlas, Annals of biomedical engineering 49 (2021) 233–250. [PubMed: 32458222]

[104]. McDowell KS, Vadakkumpadan F, Blake R, Blauer J, Plank G, MacLeod RS, Trayanova NA, Methodology for patient-specific modeling of atrial fibrosis as a substrate for atrial fibrillation, Journal of electrocardiology 45 (6) (2012) 640–645. [PubMed: 22999492]

[105]. Trayanova NA, Your personal virtual heart, IEEE Spectrum 51 (11) (2014) 34–59.

[106]. Prakosa A, Arevalo HJ, Deng D, Boyle PM, Nikolov PP, Ashikaga H, Blauer JJ, Ghafoori E, Park CJ, Blake RC, et al. , Personalized virtual-heart technology for guiding the ablation of infarct-related ventricular tachycardia, Nature biomedical engineering 2 (10) (2018) 732–740.

[107]. Lopez-Perez A, Sebastian R, Izquierdo M, Ruiz R, Bishop M, Ferrero JM, Personalized cardiac computational models: from clinical data to simulation of infarct-related ventricular tachycardia, Frontiers in physiology 10 (2019) 580. [PubMed: 31156460]

[108]. Roney CH, Beach ML, Mehta AM, Sim I, Corrado C, Bendikas R, Solis-Lemus JA, Razeghi O, Whitaker J, O'Neill L, et al. , In silico comparison of left atrial ablation techniques that target the anatomical, structural, and electrical substrates of atrial fibrillation, Frontiers in physiology 11 (2020) 1145. [PubMed: 33041850]

[109]. Niederer S, Aboelkassem Y, Cantwell CD, Corrado C, Coveney S, Cherry EM, Delhaas T, Fenton FH, Panfilov A, Pathmanathan P, et al. , Creation and application of virtual patient cohorts of heart models, Philosophical Transactions of the Royal Society A 378 (2173) (2020) 20190558.

[110]. Roney CH, Beach M, Mehta A, Sim I, Corrado C, Bendikas R, Solis-Lemus JA, Razeghi O, Whitaker J, O'Neill L, et al., Constructing virtual patient cohorts for simulating atrial fibrillation ablation, in: 2020 Computing in Cardiology, IEEE, 2020, pp. 1–4.

[111]. Plank G, Loewe A, Neic A, Augustin C, Huang Y-L, Gsell MA, Karabelas E, Nothstein M, Prassl AJ, Sánchez J, et al. , The openCARP Simulation Environment for Cardiac Electrophysiology, Computer Methods and Programs in Biomedicine (2021) 106223. [PubMed: 34171774]

[112]. Niederer SA, Lumens J, Trayanova NA, Computational models in cardiology, Nature Reviews Cardiology 16 (2) (2019) 100–111. [PubMed: 30361497]

[113]. Sato D, Xie Y, Weiss JN, Qu Z, Garfinkel A, Sanderson AR, Acceleration of cardiac tissue simulation with graphic processing units, Medical & biological engineering & computing 47 (9) (2009) 1011–1015. [PubMed: 19655187]

[114]. Niederer S, Mitchell L, Smith N, Plank G, Simulating human cardiac electrophysiology on clinical time-scales, Frontiers in physiology 2 (2011) 14. [PubMed: 21516246]

[115]. Gouvêa de Barros B, Sachetto Oliveira R, Meira W, Lobosco M, Weber dos Santos R, Simulations of complex and microscopic models of cardiac electrophysiology powered by multi-gpu platforms, Computational and mathematical methods in medicine 2012.

[116]. Kaboudian A, Cherry EM, Fenton FH, Real-time interactive simulations of large-scale systems on personal computers and cell phones: Toward patient-specific heart modeling and other applications, Science advances 5 (3) (2019) eaav6019. [PubMed: 30944861]

[117]. Tung L, A bi-domain model for describing ischemic myocardial dc potentials., Ph.D. thesis, Massachusetts Institute of Technology (1978).

[118]. Neu J, Krassowska W, Homogenization of syncytial tissues., Critical reviews in biomedical engineering 21 (2) (1993) 137–199. [PubMed: 8243090]

[119]. Henriquez CS, Simulating the electrical behavior of cardiac tissue using the bidomain model, Crit Rev Biomed Eng 21 (1) (1993) 1–77. [PubMed: 8365198]

[120]. Roth BJ, Electrical conductivity values used with the bidomain model of cardiac tissue, IEEE Transactions on Biomedical Engineering 44 (4) (1997) 326–328. [PubMed: 9125816]

[121]. Sundnes J, Nielsen BF, Mardal KA, Cai X, Lines GT, Tveito A, On the computational complexity of the bidomain and the monodomain models of electrophysiology, Annals of biomedical engineering 34 (7) (2006) 1088–1097. [PubMed: 16773461]

[122]. Vigmond E, Dos Santos RW, Prassl A, Deo M, Plank G, Solvers for the cardiac bidomain equations, Progress in biophysics and molecular biology 96 (1-3) (2008) 3–18. [PubMed: 17900668]

[123]. Ethier M, Bourgault Y, Semi-implicit time-discretization schemes for the bidomain model, SIAM Journal on Numerical Analysis 46 (5) (2008) 2443–2468.

[124]. Potse M, Dubé B, Richer J, Vinet A, Gulrajani RM, A comparison of monodomain and bidomain reaction-diffusion models for action potential propagation in the human heart, IEEE Transactions on Biomedical Engineering 53 (12) (2006) 2425–2435. [PubMed: 17153199]

[125]. dos Santos RW, Dickstein F, On the influence of a volume conductor on the orientation of currents in a thin cardiac tissue, Lecture Notes in Computer Science (2003) 111–121.

[126]. Roth BJ, Beaudoin DL, Approximate analytical solutions of the bidomain equations for electrical stimulation of cardiac tissue with curving fibers, Physical Review E 67 (5) (2003) 051925.

[127]. Karma A, Spiral breakup in model equations of action potential propagation in cardiac tissue, Physical review letters 71 (7) (1993) 1103. [PubMed: 10055449]

[128]. Karma A, Electrical alternans and spiral wave breakup in cardiac tissue, Chaos: An Interdisciplinary Journal of Nonlinear Science 4 (3) (1994) 461–472.

[129]. Pastore JM, Girouard SD, Laurita KR, Akar FG, Rosenbaum DS, Mechanism linking T-wave alternans to the genesis of cardiac fibrillation, Circulation 99 (10) (1999) 1385–1394. [PubMed: 10077525]

[130]. Fox JJ, Riccio ML, Hua F, Bodenschatz E, Gilmour RF, Spatiotemporal transition to conduction block in canine ventricle, Circ Res 90 (2002) 289–296. [PubMed: 11861417]

[131]. Fox JJ, McHarg JL, Gilmour RF, Ionic mechanism of electrical alternans, Am J Physiol Heart Circ Physiol 282 (2002) H516–H530. [PubMed: 11788399]

[132]. Fox JJ, Gilmour R, Bodenschatz E, Conduction block in one-dimensional heart fibers, Phys Rev Lett 89 (19) (2002) 198101. [PubMed: 12443153]

[133]. Echebarria B, Karma A, Instability and spatiotemporal dynamics of alternans in paced cardiac tissue, Phys. Rev. Lett 88 (2002) 208101. [PubMed: 12005608]

[134]. Sato D, Shiferaw Y, Garfinkel A, Weiss JN, Qu Z, Karma A, Spatially discordant alternans in cardiac tissue, Circulation research 99 (5) (2006) 520–527. [PubMed: 16902177]

[135]. Lewis T, Notes upon alternation of the heart, Quart J Med 4 (141) (1910) 1910–1911.

[136]. Rosenbaum DS, Jackson LE, Smith JM, Garan H, Ruskin JN, Cohen RJ, Electrical alternans and vulnerability to ventricular arrhythmias, New England Journal of Medicine 330 (4) (1994) 235–241. [PubMed: 8272084]

[137]. Estes NA 3rd, Michaud G, Zipes DP, El-Sherif N, Venditti FJ, Rosenbaum DS, Albrecht P, Wang PJ, Cohen RJ, Electrical alternans during rest and exercise as predictors of vulnerability to ventricular arrhythmias, Am J Cardiol 80 (10) (1997) 1314–1318. [PubMed: 9388105]

[138]. Narayan SM, Bode F, Karasik PL, Franz MR, Alternans of atrial action potentials during atrial flutter as a precursor to atrial fibrillation, Circulation 106 (15) (2002) 1968–1973. [PubMed: 12370221]

[139]. Nolasco JB, Dahlen RW, A graphic method for the study of alternation in cardiac action potentials, J Appl Physiol 25 (2) (1968) 191–196. [PubMed: 5666097]

[140]. Guevara M, Ward G, Shrier A, Glass L, Electrical alternans and period doubling bifurcations, IEEE Comp. Cardiol 562 (1984) 167–170.

[141]. Guevara M, Alonso F, van Ginneken DJD,A, Alternans in periodically stimulated isolated ventricular myocytes: experiment and model, in: Goldbeter A (Ed.), Cell to Cell Signalling: From Experiments to Theoretical Models, Academic, London, 1989, pp. 551–563.

[142]. Strogatz SH, Nonlinear dynamics and chaos: with applications to physics, biology, chemistry, and engineering, Westview press, 2014.

[143]. Qu Z, Xie Y, Garfinkel A, Weiss JN, T-wave alternans and arrhythmogenesis in cardiac diseases, Frontiers in physiology 1 (2010) 154. [PubMed: 21286254]

[144]. Lab M, Lee J, Changes in intracellular calcium during mechanical alternans in isolated ferret ventricular muscle., Circulation research 66 (3) (1990) 585–595. [PubMed: 2306800]

[145]. Chudin E, Goldhaber J, Garfinkel A, Weiss J, Kogan B, Intracellular Ca2+ dynamics and the stability of ventricular tachycardia, Biophysical journal 77 (6) (1999) 2930–2941. [PubMed: 10585917]

[146]. Hüser J, Wang YG, Sheehan KA, Cifuentes F, Lipsius SL, Blatter LA, Functional coupling between glycolysis and excitationcontraction coupling underlies alternans in cat heart cells, The Journal of physiology 524 (3) (2000) 795–806. [PubMed: 10790159]

[147]. Díaz ME, O'neill SC, Eisner DA, Sarcoplasmic reticulum calcium content fluctuation is the key to cardiac alternans, Circulation research 94 (5) (2004) 650–656. [PubMed: 14752033]

[148]. Qu Z, Nivala M, Weiss JN, Calcium alternans in cardiac myocytes: order from disorder, Journal of molecular and cellular cardiology 58 (2013) 100–109. [PubMed: 23104004]

[149]. Bers D, Excitation-contraction coupling and cardiac contractile force, Kluwer, Boston, 2001.

[150]. Cheng H, Lederer WJ, Cannell MB, Calcium sparks: elementary events underlying excitation-contraction coupling in heart muscle, Science 262 (5134) (1993) 740–744. [PubMed: 8235594]

[151]. Kockskämper J, Blatter LA, Subcellular Ca2+ alternans represents a novel mechanism for the generation of arrhythmogenic Ca2+ waves in cat atrial myocytes, The Journal of physiology 545 (1) (2002) 65–79. [PubMed: 12433950]

[152]. Cui X, Rovetti RJ, Yang L, Garfinkel A, Weiss JN, Qu Z, Period-doubling bifurcation in an array of coupled stochastically excitable elements subjected to global periodic forcing, Physical review letters 103 (4) (2009) 044102. [PubMed: 19659359]

[153]. Rovetti R, Cui X, Garfinkel A, Weiss JN, Qu Z, Spark-induced sparks as a mechanism of intra-cellular calcium alternans in cardiac myocytes, Circulation research 106 (10) (2010) 1582–1591. [PubMed: 20378857]

[154]. Restrepo JG, Karma A, Spatiotemporal intracellular calcium dynamics during cardiac alternans, Chaos: An Interdisciplinary Journal of Nonlinear Science 19 (3) (2009) 037115.

[155]. Winfree AT, When Time Breaks Down: The Three-dimensional Dynamics of Electrochemical Waves and Cardiac Arrhythmias, Princeton University Press, Princeton, N.J., 1987.

[156]. Winfree AT, Electrical instability in cardiac muscle: phase singularities and rotors, Journal of Theoretical Biology 138 (3) (1989) 353–405. [PubMed: 2593680]

[157]. Lee KJ, Cox EC, Goldstein RE, Competing patterns of signaling activity in Dictyostelium discoideum, Physical Review Letters 76 (7) (1996) 1174. [PubMed: 10061652]

[158]. Gorelova N, Bureš J, Spiral waves of spreading depression in the isolated chicken retina, Developmental Neurobiology 14 (5) (1983) 353–363.

[159]. Jakubith S, Rotermund HH, Engel W, Von Oertzen A, Ertl G, Spatiotemporal concentration patterns in a surface reaction: Propagating and standing waves, rotating spirals, and turbulence, Physical Review Letters 65 (24) (1990) 3013. [PubMed: 10042757]

[160]. Epstein IR, Showalter K, Nonlinear chemical dynamics: oscillations, patterns, and chaos, The Journal of Physical Chemistry 100 (31) (1996) 13132–13147.

[161]. Winfree AT, Spiral waves of chemical activity, Science 175 (4022) (1972) 634–636. [PubMed: 17808803]

[162]. Quan W, Rudy Y, Unidirectional block and reentry of cardiac excitation: a model study., Circulation research 66 (2) (1990) 367–382. [PubMed: 2297808]

[163]. Xie Y, Garfinkel A, Camelliti P, Kohl P, Weiss JN, Qu Z, Effects of fibroblast-myocyte coupling on cardiac conduction and vulnerability to reentry: a computational study, Heart Rhythm 6 (11) (2009) 1641–1649. [PubMed: 19879544]

[164]. Yang M-J, Tran DX, Weiss JN, Garfinkel A, Qu Z, The pinwheel experiment revisited: effects of cellular electrophysiological properties on vulnerability to cardiac reentry, American Journal of Physiology-Heart and Circulatory Physiology 293 (3) (2007) H1781–H1790. [PubMed: 17586622]

[165]. Shibata N, Chen P-S, Dixon EG, Wolf PD, Danieley N, Smith WM, Ideker RE, Influence of shock strength and timing on induction of ventricular arrhythmias in dogs, American Journal of Physiology-Heart and Circulatory Physiology 255 (4) (1988) H891–H901.

[166]. Chen P-S, Wolf PD, Dixon EG, Danieley ND, Frazier DW, Smith WM, Ideker RE, Mechanism of ventricular vulnerability to single premature stimuli in open-chest dogs., Circulation research 62 (6) (1988) 1191–1209. [PubMed: 2454762]

[167]. Frazier DW, Wolf PD, Wharton JM, Tang A, Smith WM, Ideker RE, et al. , Stimulus-induced critical point. mechanism for electrical initiation of reentry in normal canine myocardium., The Journal of clinical investigation 83 (3) (1989) 1039–1052. [PubMed: 2921316]

[168]. Roth BJ, The pinwheel experiment revisited, Journal of theoretical biology 190 (4) (1998) 389–393. [PubMed: 9533873]

[169]. Sambelashvili A, Efimov IR, The pinwheel experiment re-revisited, Journal of theoretical biology 214 (2) (2002) 147–153. [PubMed: 11812169]

[170]. Lin S-F, Roth BJ, Wikswo JP Jr, Quatrefoil reentry in myocardinm: An optical imaging study of the induction mechanism, Journal of cardiovascular electrophysiology 10 (4) (1999) 574–586. [PubMed: 10355700]

[171]. Frame LH, Simson MB, Oscillations of conduction, action potential duration, and refractoriness. a mechanism for spontaneous termination of reentrant tachycardias., Circulation 78 (5) (1988) 1277–1287. [PubMed: 3180384]

[172]. Courtemanche M, Glass L, Keener JP, Instabilities of a propagating pulse in a ring of excitable media, Physical Review Letters 70 (14) (1993) 2182. [PubMed: 10053491]

[173]. Weiss JN, Karma A, Shiferaw Y, Chen P-S, Garfinkel A, Qu Z, From pulsus to pulseless, Circulation research 98 (10) (2006) 1244–1253. [PubMed: 16728670]

[174]. Gaeta S, Christini DJ, Non-linear dynamics of cardiac alternans: subcellular to tissue-level mechanisms of arrhythmia, Frontiers in physiology 3 (2012) 157. [PubMed: 22783195]

[175]. Watanabe MA, Fenton FH, Evans SJ, Hastings HM, Karma A, Mechanisms for discordant alternans, J Cardiovasc Electrophysiol 12 (2001) 196–206. [PubMed: 11232619]

[176]. Echebarria B, Karma A, Instability and spatiotemporal dynamics of alternans in paced cardiac tissue, Physical review letters 88 (20) (2002) 208101. [PubMed: 12005608]

[177]. Echebarria B, Karma A, Amplitude equation approach to spatiotemporal dynamics of cardiac alternans, Physical Review E 76 (5) (2007) 051911.

[178]. Hayashi H, Shiferaw Y, Sato D, Nihei M, Lin S-F, Chen P-S, Garfinkel A, Weiss JN, Qu Z, Dynamic origin of spatially discordant alternans in cardiac tissue, Biophysical journal 92 (2) (2007) 448–460. [PubMed: 17071663]

[179]. Glukhov AV, Fedorov VV, Lou Q, Ravikumar VK, Kalish PW, Schuessler RB, Moazami N, Efimov IR, Transmural dispersion of repolarization in failing and nonfailing human ventricle, Circulation research 106 (5) (2010) 981–991. [PubMed: 20093630]

[180]. Panfilov A, Vasiev B, Vortex initiation in a heterogeneous excitable medium, Physica D: Nonlinear Phenomena 49 (1-2) (1991) 107–113.

[181]. Aliev RR, Panfilov AV, Modeling of heart excitation patterns caused by a local inhomogeneity, Journal of theoretical biology 181 (1) (1996) 33–40. [PubMed: 8796189]

[182]. Starobin JM, Zilberter YI, Rusnak EM, Starmer CF, Wavelet formation in excitable cardiac tissue: the role of wavefront-obstacle interactions in initiating high-frequency fibrillatory-like arrhythmias, Biophysical journal 70 (2) (1996) 581–594. [PubMed: 8789078]

[183]. Qu Z, Garfinkel A, Weiss JN, Vulnerable window for conduction block in a one-dimensional cable of cardiac cells, 1: single extrasystoles, Biophysical journal 91 (3) (2006) 793–804. [PubMed: 16679367]

[184]. Keldermann RH, ten Tusscher KH, Nash MP, Hren R, Taggart P, Panfilov AV, Effect of heterogeneous apd restitution on vf organization in a model of the human ventricles, American Journal of Physiology-Heart and Circulatory Physiology 294 (2) (2008) H764–H774. [PubMed: 18055526]

[185]. Defauw A, Dawyndt P, Panfilov AV, Initiation and dynamics of a spiral wave around an ionic heterogeneity in a model for human cardiac tissue, Physical Review E 88 (6) (2013) 062703.

[186]. Alonso S, Bär M, Reentry near the percolation threshold in a heterogeneous discrete model for cardiac tissue, Physical review letters 110 (15) (2013) 158101. [PubMed: 25167313]

[187]. Zahid S, Cochet H, Boyle PM, Schwarz EL, Whyte KN, Vigmond EJ, Dubois R, Hocini M, Haïssaguerre M, Jaïs P, et al. , Patient-derived models link re-entrant driver localization in atrial fibrillation to fibrosis spatial pattern, Cardiovascular research 110 (3) (2016) 443–454. [PubMed: 27056895]

[188]. Shaw RM, Rudy Y, Electrophysiologic effects of acute myocardial ischemia: a mechanistic investigation of action potential conduction and conduction failure, Circulation Research 80 (1) (1997) 124–138. [PubMed: 8978331]

[189]. Baudino TA, Carver W, Giles W, Borg TK, Cardiac fibroblasts: friend or foe?, American Journal of Physiology-Heart and Circulatory Physiology 291 (3) (2006) H1015–H1026. [PubMed: 16617141]

[190]. Khan R, Sheppard R, Fibrosis in heart disease: understanding the role of transforming growth factor-β1 in cardiomyopathy, valvular disease and arrhythmia, Immunology 118 (1) (2006) 10–24. [PubMed: 16630019]

[191]. Kong P, Christia P, Frangogiannis NG, The pathogenesis of cardiac fibrosis, Cellular and molecular life sciences 71 (4) (2014) 549–574. [PubMed: 23649149]

[192]. Biernacka A, Frangogiannis NG, Aging and cardiac fibrosis, Aging and disease 2 (2) (2011) 158. [PubMed: 21837283]

[193]. Hinderer S, Schenke-Layland K, Cardiac fibrosis–a short review of causes and therapeutic strategies, Advanced drug delivery reviews 146 (2019) 77–82. [PubMed: 31158407]

[194]. Moreira LM, Takawale A, Hulsurkar M, Menassa DA, Antanaviciute A, Lahiri SK, Mehta N, Evans N, Psarros C, Robinson P, et al. , Paracrine signalling by cardiac calcitonin controls atrial fibrogenesis and arrhythmia, Nature 587 (7834) (2020) 460–465. [PubMed: 33149301]

[195]. Kostin S, Klein G, Szalay Z, Hein S, Bauer EP, Schaper J, Structural correlate of atrial fibrillation in human patients, Cardiovascular research 54 (2) (2002) 361–379. [PubMed: 12062341]

[196]. Zeigler AC, Richardson WJ, Holmes JW, Saucerman JJ, Computational modeling of cardiac fibroblasts and fibrosis, Journal of molecular and cellular cardiology 93 (2016) 73–83. [PubMed: 26608708]

[197]. Nguyen TP, Qu Z, Weiss JN, Cardiac fibrosis and arrhythmogenesis: the road to repair is paved with perils, Journal of molecular and cellular cardiology 70 (2014) 83–91. [PubMed: 24184999]

[198]. Gokhale TA, Medvescek E, Henriquez CS, Modeling dynamics in diseased cardiac tissue: Impact of model choice, Chaos: An Interdisciplinary Journal of Nonlinear Science 27 (9) (2017) 093909.

[199]. Spach MS, Boineau JP, Microfibrosis produces electrical load variations due to loss of side-to-side cell connections; a major mechanism of structural heart disease arrhythmias, Pacing and clinical electrophysiology 20 (2) (1997) 397–413. [PubMed: 9058844]

[200]. Christensen K, Manani KA, Peters NS, Simple model for identifying critical regions in atrial fibrillation, Physical review letters 114 (2) (2015) 028104. [PubMed: 25635565]

[201]. Ciacci A, Falkenberg M, Manani KA, Evans TS, Peters NS, Christensen K, Understanding the transition from paroxysmal to persistent atrial fibrillation, Physical review research 2 (2) (2020) 023311. [PubMed: 32607500]

[202]. Costa CM, Campos FO, Prassl AJ, dos Santos RW, Sánchez-Quintana D, Ahammer H, Hofer E, Plank G, An efficient finite element approach for modeling fibrotic clefts in the heart, IEEE Transactions on Biomedical Engineering 61 (3) (2013) 900–910.

[203]. Spach MS, Heidlage JF, Dolber PC, Barr RC, Mechanism of origin of conduction disturbances in aging human atrial bundles: experimental and model study, Heart rhythm 4 (2) (2007) 175–185. [PubMed: 17275753]

[204]. Engelman ZJ, Trew ML, Smaill BH, Structural heterogeneity alone is a sufficient substrate for dynamic instability and altered restitution, Circulation: Arrhythmia and Electrophysiology 3 (2) (2010) 195–203. [PubMed: 20133934]

[205]. Hubbard ML, Henriquez CS, A microstructural model of reentry arising from focal breakthrough at sites of source-load mismatch in a central region of slow conduction, American Journal of Physiology-Heart and Circulatory Physiology 306 (9) (2014) H1341–H1352. [PubMed: 24610922]

[206]. McDowell KS, Arevalo HJ, Maleckar MM, Trayanova NA, Susceptibility to arrhythmia in the infarcted heart depends on myofibroblast density, Biophysical journal 101 (6) (2011) 1307–1315. [PubMed: 21943411]

[207]. McDowell KS, Vadakkumpadan F, Blake R, Blauer J, Plank G, MacLeod RS, Trayanova NA, Mechanistic inquiry into the role of tissue remodeling in fibrotic lesions in human atrial fibrillation, Biophysical journal 104 (12) (2013) 2764–2773. [PubMed: 23790385]

[208]. Alonso S, Dos Santos RW, Bär M, Reentry and ectopic pacemakers emerge in a three-dimensional model for a slab of cardiac tissue with diffuse microfibrosis near the percolation threshold, PloS one 11 (11) (2016) e0166972. [PubMed: 27875591]

[209]. Ashikaga H, Arevalo H, Vadakkumpadan F, Blake III RC, Bayer JD, Nazarian S, Zviman MM, Tandri H, Berger RD, Calkins H, et al. , Feasibility of image-based simulation to estimate ablation target in human ventricular arrhythmia, Heart Rhythm 10 (8) (2013) 1109–1116. [PubMed: 23608593]

[210]. Marrouche NF, Wilber D, Hindricks G, Jais P, Akoum N, Marchlinski F, Kholmovski E, Burgon N, Hu N, Mont L, et al. , Association of atrial tissue fibrosis identified by delayed enhancement MRI and atrial fibrillation catheter ablation: the DECAAF study, Jama 311 (5) (2014) 498–506. [PubMed: 24496537]

[211]. Boyle PM, Zghaib T, Zahid S, Ali RL, Deng D, Franceschi WH, Hakim JB, Murphy MJ, Prakosa A, Zimmerman SL, et al. , Computationally guided personalized targeted ablation of persistent atrial fibrillation, Nature biomedical engineering 3 (11) (2019) 870–879.

[212]. Garfinkel A, Qu Z, Nonlinear dynamics of excitation and propagation in cardiac muscle, in: Zipes DP, Jalife J (Eds.), Cardiac Electrophysiology: From Cell to Bedside, WB Saunders, Philadelphia, 1999, pp. 315–320.

[213]. Gray RA, Pertsov AM, Jalife J, Spatial and temporal organization during cardiac fibrillation, Nature 392 (6671) (1998) 75–78. [PubMed: 9510249]

[214]. Narayan SM, Krummen DE, Shivkumar K, Clopton P, Rappel W-J, Miller JM, Treatment of atrial fibrillation by the ablation of localized sources: CONFIRM (Conventional Ablation for Atrial Fibrillation With or Without Focal Impulse and Rotor Modulation) trial, Journal of the American College of Cardiology 60 (7) (2012) 628–636. [PubMed: 22818076]

[215]. Qu Z, Xie F, Garfinkel A, Weiss JN, Origins of spiral wave meander and breakup in a two-dimensional cardiac tissue model, Ann Biomed Eng 28 (7) (2000) 755–771. [PubMed: 11016413]

[216]. Courtemanche M, Winfree A, Re-entrant rotating waves in a Beeler-Reuter based model of two-dimensional cardiac electrical activity, International Journal of Bifurcation and Chaos 1 (1991) 431–444.

[217]. Karma A, Spiral breakup in model equations of action potential propagation in cardiac tissue, Physical Review Letters 71 (1993) 1103–1106. [PubMed: 10055449]

[218]. Chialvo DR, Michaels DC, Jalife J, Supernormal excitability as a mechanism of chaotic dynamics of activation in cardiac purkinje fibers., Circulation research 66 (2) (1990) 525–545. [PubMed: 2297816]

[219]. Bray M-A, Lin S-F, Aliev RR, Roth BJ, Wikswo JP Jr, Experimental and theoretical analysis of phase singularity dynamics in cardiac tissue, Journal of cardiovascular electrophysiology 12 (6) (2001) 716–722. [PubMed: 11405407]

[220]. Bray M-A, Wikswo JP, Use of topological charge to determine filament location and dynamics in a numerical model of scroll wave activity, IEEE transactions on biomedical engineering 49 (10) (2002) 1086–1093. [PubMed: 12374332]

[221]. Lombardo DM, Rappel W-J, Chaotic tip trajectories of a single spiral wave in the presence of heterogeneities, Physical Review E 99 (6) (2019) 062409. [PubMed: 31330597]

[222]. Winfree AT, Varieties of spiral wave behavior: An experimentalists approach to the theory of excitable media, Chaos: An Interdisciplinary Journal of Nonlinear Science 1 (3) (1991) 303–334.

[223]. Cherry EM, Evans S, Properties of two human atrial cell models in tissue: restitution, memory, propagation, and reentry, J Theor Biol 254 (2008) 674–690. [PubMed: 18652834]

[224]. Barkley D, Euclidean symmetry and the dynamics of rotating spiral waves, Physical Review Letters 72 (1994) 164–167. [PubMed: 10055592]

[225]. Sandstede B, Scheel A, Superspiral structures of meandering and drifting spiral waves, Physical Review Letters 86 (1) (2001) 171. [PubMed: 11136121]

[226]. Xu L, Li Z, Qu Z, Di Z, Resonance drifts of spiral waves on media of periodic excitability, Physical Review E 85 (4) (2012) 046216.

[227]. Wolf A, Swift JB, Swinney HL, Vastano JA, Determining Lyapunov exponents from a time series, Physica D: nonlinear phenomena 16 (3) (1985) 285–317.

[228]. Rappel W-J, Intermittent trapping of spiral waves in a cardiac model, Physical Review E 105 (1) (2022) 014404. [PubMed: 35193211]

[229]. Allessie MA, Bonke FI, Schopman FJ, Circus movement in rabbit atrial muscle as a mechanism of tachycardia, Circulation research 33 (1) (1973) 54–62. [PubMed: 4765700]

[230]. Kavanagh KM, Kabas JS, Rollins DL, Melnick SB, Smith WM, Ideker RE, High-current stimuli to the spared epicardium of a large infarct induce ventricular tachycardia., Circulation 85 (2) (1992) 680–698. [PubMed: 1735161]

[231]. Winfree A, Electrical turbulence in three-dimensional heart muscle, Science 266 (5187) (1994) 1003–1006. [PubMed: 7973648]

[232]. Keener JP, The dynamics of three-dimensional scroll waves in excitable media, Physica D: Nonlinear Phenomena 31 (2) (1988) 269–276.

[233]. Biktashev V, Holden A, Zhang H, Tension of organizing filaments of scroll waves, Philosophical Transactions of the Royal Society of London. Series A: Physical and Engineering Sciences 347 (1685) (1994) 611–630.

[234]. Fenton F, Karma A, Fiber-rotation-induced vortex turbulence in thick myocardium, Physical review letters 81 (2) (1998) 481.

[235]. Henry H, Hakim V, Linear stability of scroll waves, Physical review letters 85 (25) (2000) 5328. [PubMed: 11135988]

[236]. Alonso S, Sagués F, Mikhailov AS, Taming Winfree turbulence of scroll waves in excitable media, Science 299 (5613) (2003) 1722–1725. [PubMed: 12560470]

[237]. Davidsen J, Zhan M, Kapral R, Filament-induced surface spiral turbulence in three-dimensional excitable media, Physical Review Letters 101 (20) (2008) 208302. [PubMed: 19113385]

[238]. Alonso S, Bär M, Panfilov AV, Negative tension of scroll wave filaments and turbulence in three-dimensional excitable media and application in cardiac dynamics, Bulletin of Mathematical Biology 75 (8) (2013) 1351–1376. [PubMed: 22829178]

[239]. Mangoni ME, Nargeot J, Genesis and regulation of the heart automaticity, Physiological reviews 88 (3) (2008) 919–982. [PubMed: 18626064]

[240]. Lev M, The pathology of complete atrioventricular block, Progress in cardiovascular diseases 6 (4) (1964) 317–326. [PubMed: 14105712]

[241]. Keener JP, On cardiac arrythmias: AV conduction block, Journal of Mathematical Biology 12 (2) (1981) 215–225.

[242]. Shrier A, Dubarsky H, Rosengarten M, Guevara MR, Nattel S, Glass L, Prediction of complex atrioventricular conduction rhythms in humans with use of the atrioventricular nodal recovery curve., Circulation 76 (6) (1987) 1196–1205. [PubMed: 3677347]

[243]. January CT, Riddle JM, Early afterdepolarizations: mechanism of induction and block. A role for L-type Ca2+ current., Circulation research 64 (5) (1989) 977–990. [PubMed: 2468430]

[244]. Sato D, Xie L-H, Sovari AA, Tran DX, Morita N, Xie F, Karagueuzian H, Garfinkel A, Weiss JN, Qu Z, Synchronization of chaotic early afterdepolarizations in the genesis of cardiac arrhythmias, Proceedings of the National Academy of Sciences 106 (9) (2009) 2983–2988.

[245]. Weiss JN, Garfinkel A, Karagueuzian HS, Chen P-S, Qu Z, Early afterdepolarizations and cardiac arrhythmias, Heart rhythm 7 (12) (2010) 1891–1899. [PubMed: 20868774]

[246]. Ter Keurs HE, Boyden PA, Calcium and arrhythmogenesis, Physiological reviews 87 (2) (2007) 457–506. [PubMed: 17429038]

[247]. Vidmar D, Alhusseini MI, Narayan SM, Rappel W-J, Characterizing electrogram signal fidelity and the effects of signal contamination on mapping human persistent atrial fibrillation, Frontiers in Physiology 9 (2018) 1232. [PubMed: 30237766]

[248]. Rappel W-J, Narayan SM, Theoretical considerations for mapping activation in human cardiac fibrillation, Chaos: An Interdisciplinary Journal of Nonlinear Science 23 (2) (2013) 023113.

[249]. Roney CH, Cantwell CD, Bayer JD, Qureshi NA, Lim PB, Tweedy JH, Kanagaratnam P, Peters NS, Vigmond EJ, Ng FS, Spatial resolution requirements for accurate identification of drivers of atrial fibrillation, Circulation: Arrhythmia and Electrophysiology 10 (5) (2017) e004899. [PubMed: 28500175]

[250]. Lalani GG, Schricker A, Gibson M, Rostamian A, Krummen DE, Narayan SM, Atrial conduction slows immediately before the onset of human atrial fibrillation: a bi-atrial contact mapping study of transitions to atrial fibrillation, Journal of the American College of Cardiology 59 (6) (2012) 595–606. [PubMed: 22300695]

[251]. Skanes AC, Mandapati R, Berenfeld O, Davidenko JM, Jalife J, Spatiotemporal periodicity during atrial fibrillation in the isolated sheep heart, Circulation 98 (12) (1998) 1236–1248. [PubMed: 9743516]

[252]. Kirchhof C, Chorro F, Scheffer GJ, Brugada J, Konings K, Zetelaki Z, Allessie M, Regional entrainment of atrial fibrillation studied by high-resolution mapping in open-chest dogs., Circulation 88 (2) (1993) 736–749. [PubMed: 8339434]

[253]. Cherry EM, Fenton FH, Visualization of spiral and scroll waves in simulated and experimental cardiac tissue, New Journal of Physics 10 (12) (2008) 125016.

[254]. Rensma PL, Allessie MA, Lammers WJ, Bonke FI, Schalij MJ, Length of excitation wave and susceptibility to reentrant atrial arrhythmias in normal conscious dogs., Circulation research 62 (2) (1988) 395–410. [PubMed: 3338122]

[255]. Narayan SM, Kazi D, Krummen DE, Rappel W-J, Repolarization and activation restitution near human pulmonary veins and atrial fibrillation initiation: a mechanism for the initiation of atrial fibrillation by premature beats, Journal of the American College of Cardiology 52 (15) (2008) 1222–1230. [PubMed: 18926325]

[256]. Glukhov AV, Fedorov VV, Kalish PW, Ravikumar VK, Lou Q, Janks D, Schuessler RB, Moazami N, Efimov IR, Conduction remodeling in human end-stage nonischemic left ventricular cardiomyopathy, Circulation 125 (15) (2012) 1835–1847. [PubMed: 22412072]

[257]. Davidenko J, Pertsov A, Salomonsz R, Baxter W, Jalife J, Stationary and drifting spiral waves of excitation in isolated cardiac muscle, Nature 355 (6358) (1992) 349–351. [PubMed: 1731248]

[258]. Laurita KR, Girouard SD, Rosenbaum DS, Modulation of ventricular repolarization by a premature stimulus: role of epicardial dispersion of repolarization kinetics demonstrated by optical mapping of the intact guinea pig heart, Circulation research 79 (3) (1996) 493–503. [PubMed: 8781482]

[259]. Efimov IR, Nikolski VP, Salama G, Optical imaging of the heart, Circulation research 95 (1) (2004) 21–33. [PubMed: 15242982]

[260]. Iravanian S, Nabutovsky Y, Kong C-R, Saha S, Bursac N, Tung L, Functional reentry in cultured monolayers of neonatal rat cardiac cells, American Journal of Physiology-Heart and Circulatory Physiology 285 (1) (2003) H449–H456. [PubMed: 12623789]

[261]. Hansen BJ, Zhao J, Csepe TA, Moore BT, Li N, Jayne LA, Kalyanasundaram A, Lim P, Bratasz A, Powell KA, Simonetti OP, Higgins RS, Kilic A, Mohler PJ, Janssen PM, Weiss R, Hummel JD, Fedorov VV, Atrial fibrillation driven by micro-anatomic intramural re-entry revealed by simultaneous sub-epicardial and sub-endocardial optical mapping in explanted human hearts, Eur. Heart J (2015) 2390–2401. [PubMed: 26059724]

[262]. Narayan SM, Krummen DE, Enyeart MW, Rappel W-J, Computational mapping identifies localized mechanisms for ablation of atrial fibrillation, PLoS ONE 7 (9) (2012) e46034. [PubMed: 23049929]

[263]. Christoph J, Chebbok M, Richter C, Schröder-Schetelig J, Bittihn P, Stein S, Uzelac I, Fenton FH, Hasenfuß G, Gilmour R Jr, et al. , Electromechanical vortex filaments during cardiac fibrillation, Nature 555 (7698) (2018) 667–672. [PubMed: 29466325]

[264]. Lee P, Taghavi F, Yan P, Ewart P, Ashley EA, Loew LM, Kohl P, Bollensdorff C, Woods CE, In situ optical mapping of voltage and calcium in the heart, PloS one 7 (8) (2012) e42562. [PubMed: 22876327]

[265]. Konings KT, Kirchhof CJ, Smeets JR, Wellens HJ, Penn OC, Allessie MA, High-density mapping of electrically induced atrial fibrillation in humans., Circulation 89 (4) (1994) 1665–1680. [PubMed: 8149534]

[266]. Lee S, Sahadevan J, Khrestian CM, Cakulev I, Markowitz A, Waldo AL, Simultaneous biatrial high-density (510–512 electrodes) epicardial mapping of persistent and long-standing persistent atrial fibrillation in patients: new insights into the mechanism of its maintenance, Circulation 132 (22) (2015) 2108–2117. [PubMed: 26499963]

[267]. Narayan SM, Krummen DE, Rappel W-J, Clinical mapping approach to diagnose electrical rotors and focal impulse sources for human atrial fibrillation, Journal of cardiovascular electrophysiology 23 (5) (2012) 447–454. [PubMed: 22537106]

[268]. Krummen DE, Hayase J, Morris DJ, Ho J, Smetak MR, Clopton P, Rappel W-J, Narayan SM, Rotor stability separates sustained ventricular fibrillation from self-terminating episodes in humans, Journal of the American College of Cardiology 63 (24) (2014) 2712–2721. [PubMed: 24794115]

[269]. Allessie MA, de Groot NM, Houben RP, Schotten U, Boersma E, Smeets JL, Crijns HJ, Electropathological substrate of long-standing persistent atrial fibrillation in patients with structural heart disease: longitudinal dissociation, Circulation: Arrhythmia and Electrophysiology 3 (6) (2010) 606–615. [PubMed: 20719881]

[270]. Tung R, Raiman M, Liao H, Zhan X, Chung FP, Nagel R, Hu H, Jian J, Shatz DY, Besser SA, et al. , Simultaneous endocardial and epicardial delineation of 3D reentrant ventricular tachycardia, Journal of the American College of Cardiology 75 (8) (2020) 884–897. [PubMed: 32130924]

[271]. Ramanathan C, Ghanem RN, Jia P, Ryu K, Rudy Y, Noninvasive electrocardiographic imaging for cardiac electrophysiology and arrhythmia, Nature medicine 10 (4) (2004) 422.

[272]. Cuculich PS, Wang Y, Lindsay BD, Faddis MN, Schuessler RB, Damiano RJ Jr, Li L, Rudy Y, Noninvasive characterization of epicardial activation in humans with diverse atrial fibrillation patterns, Circulation 122 (14) (2010) 1364–1372. [PubMed: 20855661]

[273]. Rudy Y, Noninvasive electrocardiographic imaging of arrhythmogenic substrates in humans, Circulation research 112 (5) (2013) 863–874. [PubMed: 23449548]

[274]. Cluitmans MJ, Bonizzi P, Karel JM, Das M, Kietselaer BL, de Jong MM, Prinzen FW, Peeters RL, Westra RL, Volders PG, In vivo validation of electrocardiographic imaging, JACC: Clinical Electrophysiology (2017) 319.

[275]. Haissaguerre M, Hocini M, Denis A, Shah AJ, Komatsu Y, Yamashita S, Daly M, Amraoui S, Zellerhoff S, Picat MQ, Quotb A, Jesel L, Lim H, Ploux S, Bordachar P, Attuel G, Meillet V, Ritter P, Derval N, Sacher F, Bernus O, Cochet H, Jais P, Dubois R, Driver domains in persistent atrial fibrillation, Circulation 130 (7) (2014) 530–538. [PubMed: 25028391]

[276]. Bear LR, LeGrice IJ, Sands GB, Lever NA, Loiselle DS, Paterson DJ, Cheng LK, Smaill BH, How accurate is inverse electrocardiographic mapping? a systematic in vivo evaluation, Circulation: Arrhythmia and Electrophysiology 11 (5) (2018) e006108. [PubMed: 29700057]

[277]. Roy D, Talajic M, Nattel S, Wyse DG, Dorian P, Lee KL, Bourassa MG, Arnold JMO, Buxton AE, Camm AJ, et al. , Rhythm control versus rate control for atrial fibrillation and heart failure, New England Journal of Medicine 358 (25) (2008) 2667–2677. [PubMed: 18565859]

[278]. Van Gelder IC, Groenveld HF, Crijns HJ, Tuininga YS, Tijssen JG, Alings AM, Hillege HL, Bergsma-Kadijk JA, Cornel JH, Kamp O, et al. , Lenient versus strict rate control in patients with atrial fibrillation, New England Journal of Medicine 362 (15) (2010) 1363–1373. [PubMed: 20231232]

[279]. Cardiac Arrhythmia Suppression Trial (CAST) Investigators, Preliminary report: effect of encainide and flecainide on mortality in a randomized trial of arrhythmia suppression after myocardial infarction, New England Journal of Medicine 321 (6) (1989) 406–412. [PubMed: 2473403]

[280]. Rosen MR, Hoffman BF, Mechanisms of action of antiarrhythmic drugs, Circulation research 32 (1) (1973) 1–8. [PubMed: 4567446]

[281]. Echt DS, Liebson PR, Mitchell LB, Peters RW, Obias-Manno D, Barker AH, Arensberg D, Baker A, Friedman L, Greene HL, et al. , Mortality and morbidity in patients receiving encainide, flecainide, or placebo: the cardiac arrhythmia suppression trial, New England journal of medicine 324 (12) (1991) 781–788. [PubMed: 1900101]

[282]. Dosdall DJ, Fast VG, Ideker RE, Mechanisms of defibrillation, Annual review of biomedical engineering 12 (2010) 233–258.

[283]. Roth BJ, Sidorov VY, Wikswo JP, Virtual electrode theory of pacing, in: Cardiac Bioelectric Therapy, Springer, 2021, pp. 147–179.

[284]. Sweeney MO, Sherfesee L, DeGroot PJ, Wathen MS, Wilkoff BL, Differences in effects of electrical therapy type for ventricular arrhythmias on mortality in implantable cardioverter-defibrillator patients, Heart rhythm 7 (3) (2010) 353–360. [PubMed: 20185109]

[285]. Gillis AM, Unterberg-Buchwald C, Schmidinger H, Massimo S, Wolfe K, Kavaney DJ, Otterness MF, Hohnloser SH, G. I. A. W. Investigators, Safety and efficacy of advanced atrial

pacing therapies for atrial tachyarrhythmias in patients with a new implantable dual chamber cardioverter-defibrillator, Journal of the American College of Cardiology 40 (9) (2002) 1653–1659. [PubMed: 12427419]

[286]. Wathen MS, DeGroot PJ, Sweeney MO, Stark AJ, Otterness MF, Adkisson WO, Canby RC, Khalighi K, Machado C, Rubenstein DS, et al. , Prospective randomized multicenter trial of empirical antitachycardia pacing versus shocks for spontaneous rapid ventricular tachycardia in patients with implantable cardioverter-defibrillators: Pacing fast ventricular tachycardia reduces shock therapies (painfree rx ii) trial results, Circulation 110 (17) (2004) 2591–2596. [PubMed: 15492306]

[287]. Rosenqvist M, Antitachycardia pacing: which patients and which methods?, The American journal of cardiology 78 (5) (1996) 92–97. [PubMed: 8820842]

[288]. Swenson DJ, Taepke RT, Blauer JJ, Kwan E, Ghafoori E, Plank G, Vigmond E, MacLeod RS, DeGroot P, Ranjan R, Direct comparison of a novel antitachycardia pacing algorithm against present methods using virtual patient modeling, Heart Rhythm 17 (9) (2020) 1602–1608. [PubMed: 32438017]

[289]. Jack JJB, Noble D, Tsien RW, Electric current flow in excitable cells, Clarendon Press Oxford, 1975.

[290]. Plonsey R, Barr R, Effect of microscopic and macroscopic discontinuities on the response of cardiac tissue to defibrillating (stimulating) currents, Medical and Biological Engineering and Computing 24 (2) (1986) 130–136. [PubMed: 3713273]

[291]. Plonsey R, Barr R, Witkowski F, One-dimensional model of cardiac defibrillation, Medical and Biological Engineering and Computing 29 (5) (1991) 465–469. [PubMed: 1817207]

[292]. Keener JP, Direct activation and defibrillation of cardiac tissue, Journal of theoretical biology 178 (3) (1996) 313–324. [PubMed: 8730350]

[293]. Pumir A, Krinsky VI, How does an electric field defibrillate cardiac muscle?, Physica D: Nonlinear Phenomena 91 (1-2) (1996) 205–219.

[294]. van Rees JB, Borleffs CJW, de Bie MK, Stijnen T, van Erven L, Bax JJ, Schalij MJ, Inap-propriate implantable cardioverter-defibrillator shocks: incidence, predictors, and impact on mortality, Journal of the American College of Cardiology 57 (5) (2011) 556–562. [PubMed: 21272746]

[295]. Buchan S, Kar R, John M, Post A, Razavi M, Electrical stimulation for low-energy termination of cardiac arrhythmias: a review, Cardiovascular Drugs and Therapy (2021) 1–18.

[296]. Sepulveda NG, Roth BJ, Wikswo JP Jr, Current injection into a two-dimensional anisotropic bidomain, Biophysical journal 55 (5) (1989) 987–999. [PubMed: 2720084]

[297]. Sobie EA, Susil RC, Tung L, A generalized activating function for predicting virtual electrodes in cardiac tissue, Biophysical journal 73 (3) (1997) 1410–1423. [PubMed: 9284308]

[298]. Fast VG, Rohr S, Gillis AM, Kleber AG, Activation of cardiac tissue by extracellular electrical shocks: formation of secondary sources at intercellular clefts in monolayers of cultured myocytes, Circulation Research 82 (3) (1998) 375–385. [PubMed: 9486666]

[299]. Efimov IR, Cheng Y, Van Wagoner DR, Mazgalev T, Tchou PJ, Virtual electrode–induced phase singularity: A basic mechanism of defibrillation failure, Circulation Research 82 (8) (1998) 918–925. [PubMed: 9576111]

[300]. Nikolski VP, Sambelashvili AT, Efimov IR, Mechanisms of make and break excitation revisited: paradoxical break excitation during diastolic stimulation, American Journal of Physiology-Heart and Circulatory Physiology 282 (2) (2002) H565–H575. [PubMed: 11788404]

[301]. Knisley SB, Hill BC, Ideker RE, Virtual electrode effects in myocardial fibers, Biophysical journal 66 (3) (1994) 719–728. [PubMed: 8011903]

[302]. Wikswo JP Jr, Lin S-F, Abbas RA, Virtual electrodes in cardiac tissue: a common mechanism for anodal and cathodal stimulation, Biophysical journal 69 (6) (1995) 2195–2210. [PubMed: 8599628]

[303]. Pumir A, Nikolski V, Hörning M, Isomura A, Agladze K, Yoshikawa K, Gilmour R, Bodenschatz E, Krinsky V, Wave emission from heterogeneities opens a way to controlling chaos in the heart, Physical review letters 99 (20) (2007) 208101. [PubMed: 18233188]

[304]. Luther S, Fenton FH, Kornreich BG, Squires A, Bittihn P, Hornung D, Zabel M, Flanders J, Gladuli A, Campoy L, et al. , Low-energy control of electrical turbulence in the heart, Nature 475 (7355) (2011) 235–239. [PubMed: 21753855]

[305]. Trayanova N, Defibrillation of the heart: insights into mechanisms from modelling studies, Experimental physiology 91 (2) (2006) 323–337. [PubMed: 16469820]

[306]. Pumir A, Krinsky V, Unpinning of a rotating wave in cardiac muscle by an electric field, Journal of theoretical biology 199 (3) (1999) 311–319. [PubMed: 10433895]

[307]. Takagi S, Pumir A, Pazo D, Efimov I, Nikolski V, Krinsky V, Unpinning and removal of a rotating wave in cardiac muscle, Physical review letters 93 (5) (2004) 058101. [PubMed: 15323732]

[308]. Ripplinger CM, Krinsky VI, Nikolski VP, Efimov IR, Mechanisms of unpinning and termination of ventricular tachycardia, American Journal of Physiology-Heart and Circulatory Physiology 291 (1) (2006) H184–H192. [PubMed: 16501014]

[309]. Fenton FH, Luther S, Cherry EM, Otani NF, Krinsky V, Pumir A, Bodenschatz E, Gilmour RF Jr, Termination of atrial fibrillation using pulsed low-energy far-field stimulation, Circulation 120 (6) (2009) 467–476. [PubMed: 19635972]

[310]. Haissaguerre M, Jais P, Shah DC, Takahashi A, Hocini M, Quiniou G, Garrigue S, Le Mouroux A, Le Metayer P, Clementy J, Spontaneous initiation of atrial fibrillation by ectopic beats originating in the pulmonary veins, N. Engl. J. Med 339 (10) (1998) 659–666. [PubMed: 9725923]

[311]. Haissaguerre M, Shah AJ, Cochet H, Hocini M, Dubois R, Efimov I, Vigmond E, Bernus O, Trayanova N, Intermittent drivers anchoring to structural heterogeneities as a major pathophysiological mechanism of human persistent atrial fibrillation, The Journal of physiology 594 (9) (2016) 2387–2398. [PubMed: 26890861]

[312]. Chen S-A, Hsieh M-H, Tai C-T, Tsai C-F, Prakash V, Yu W-C, Hsu T-L, Ding Y-A, Chang M-S, Initiation of atrial fibrillation by ectopic beats originating from the pulmonary veins: electrophysiological characteristics, pharmacological responses, and effects of radiofrequency ablation, Circulation 100 (18) (1999) 1879–1886. [PubMed: 10545432]

[313]. Tondo C, Iacopino S, Pieragnoli P, Molon G, Verlato R, Curnis A, Landolina M, Allocca G, Arena G, Fassini G, et al. , Pulmonary vein isolation cryoablation for patients with persistent and long-standing persistent atrial fibrillation: Clinical outcomes from the real-world multicenter observational project, Heart Rhythm 15 (3) (2018) 363–368. [PubMed: 29107190]

[314]. Rappel W-J, Krummen DE, Baykaner T, Zaman J, Donsky A, Swarup V, Miller JM, Narayan SM, Stochastic termination of spiral wave dynamics in cardiac tissue, Frontiers in Network Physiology (2022) 2.

[315]. Baykaner T, Rogers AJ, Meckler GL, Zaman J, Navara R, Rodrigo M, Alhusseini M, Kowalewski CA, Viswanathan MN, Narayan SM, et al. , Clinical implications of ablation of drivers for atrial fibrillation: a systematic review and meta-analysis, Circulation: Arrhythmia and Electrophysiology 11 (5) (2018) e006119. [PubMed: 29743170]

[316]. Rappel W-J, Zaman JA, Narayan SM, Mechanisms for the termination of atrial fibrillation by localized ablation: computational and clinical studies, Circulation: Arrhythmia and Electrophysiology 8 (6) (2015) 1325–1333. [PubMed: 26359479]

[317]. Caixal G, Alarcón F, Althoff TF, Nuñez-Garcia M, Benito EM, Borràs R, Perea RJ, Prat-González S, Garre P, Soto-Iglesias D, et al. , Accuracy of left atrial fibrosis detection with cardiac magnetic resonance: correlation of late gadolinium enhancement with endocardial voltage and conduction velocity, EP Europace 23 (3) (2021) 380–388.

[318]. Ganz LI, Friedman PL, Supraventricular tachycardia, New England Journal of Medicine 332 (3) (1995) 162–173. [PubMed: 7800009]

[319]. Jackman WM, Wang X, Friday KJ, Roman CA, Moulton KP, Beckman KJ, Mc-Clelland JH, Twidale N, Hazlitt HA, Prior MI, et al. , Catheter ablation of accessory atrioventricular pathways (Wolff–Parkinson–White syndrome) by radiofrequency current, New England Journal of Medicine 324 (23) (1991) 1605–1611. [PubMed: 2030716]

[320]. Pappone C, Vicedomini G, Manguso F, Saviano M, Baldi M, Pappone A, Ciaccio C, Giannelli L, Ionescu B, Petretta A, et al. , Wolff-Parkinson-White syndrome in the era of catheter ablation:

insights from a registry study of 2169 patients, Circulation 130 (10) (2014) 811–819. [PubMed: 25052405]

[321]. Badhwar N, Scheinman MM, Idiopathic ventricular tachycardia: diagnosis and management, Current problems in cardiology 32 (1) (2007) 7–43. [PubMed: 17197289]

[322]. Brugada P, Brugada J, Right bundle branch block, persistent ST segment elevation and sudden cardiac death: a distinct clinical and electrocardiographic syndrome: a multicenter report, Journal of the American College of Cardiology 20 (6) (1992) 1391–1396. [PubMed: 1309182]

[323]. Brugada J, Campuzano O, Arbelo E, Sarquella-Brugada G, Brugada R, Present status of Brugada syndrome: JACC state-of-the-art review, Journal of the American College of Cardiology 72 (9) (2018) 1046–1059. [PubMed: 30139433]

[324]. Nademanee K, Veerakul G, Chandanamattha P, Chaothawee L, Ariyachaipanich A, Jirasiriro-janakorn K, Likittanasombat K, Bhuripanyo K, Ngarmukos T, Prevention of ventricular fibrillation episodes in Brugada syndrome by catheter ablation over the anterior right ventricular outflow tract epicardium, Circulation 123 (12) (2011) 1270–1279. [PubMed: 21403098]

[325]. Brugada J, Pappone C, Berruezo A, Vicedomini G, Manguso F, Ciconte G, Giannelli L, Santinelli V, Brugada syndrome phenotype elimination by epicardial substrate ablation, Circulation: Arrhythmia and Electrophysiology 8 (6) (2015) 1373–1381. [PubMed: 26291334]

[326]. Dukkipati SR, Choudry S, Koruth JS, Miller MA, Whang W, Reddy VY, Catheter ablation of ventricular tachycardia in structurally normal hearts: indications, strategies, and outcomespart i, Journal of the American College of Cardiology 70 (23) (2017) 2909–2923. [PubMed: 29216987]

[327]. Stevenson WG, Soejima K, Catheter ablation for ventricular tachycardia, Circulation 115 (21) (2007) 2750–2760. [PubMed: 17533195]

[328]. Stevenson WG, Friedman PL, Sager PT, Saxon LA, Kocovic D, Harada T, Wiener I, Khan H, Exploring postinfarction reentrant ventricular tachycardia with entrainment mapping, Journal of the American College of Cardiology 29 (6) (1997) 1180–1189. [PubMed: 9137211]

[329]. Josephson ME, Anter E, Substrate mapping for ventricular tachycardia: assumptions and misconceptions, JACC: Clinical Electrophysiology 1 (5) (2015) 341–352. [PubMed: 29759461]

[330]. Stevenson WG, Friedman PL, Kocovic D, Sager PT, Saxon LA, Pavri B, Radiofrequency catheter ablation of ventricular tachycardia after myocardial infarction, Circulation 98 (4) (1998) 308–314. [PubMed: 9711935]

[331]. Sapp JL, Wells GA, Parkash R, Stevenson WG, Blier L, Sarrazin J-F, Thibault B, Rivard L, Gula L, Leong-Sit P, et al. , Ventricular tachycardia ablation versus escalation of antiarrhythmic drugs, New England Journal of Medicine 375 (2) (2016) 111–121. [PubMed: 27149033]

[332]. Tung R, Vaseghi M, Frankel DS, Vergara P, Di Biase L, Nagashima K, Yu R, Vangala S, Tseng C-H, Choi E-K, et al. , Freedom from recurrent ventricular tachycardia after catheter ablation is associated with improved survival in patients with structural heart disease: an International VT Ablation Center Collaborative Group study, Heart rhythm 12 (9) (2015) 1997–2007. [PubMed: 26031376]

[333]. Tanawuttiwat T, Nazarian S, Calkins H, The role of catheter ablation in the management of ventricular tachycardia, European heart journal 37 (7) (2016) 594–609. [PubMed: 26324538]

[334]. Arevalo HJ, Vadakkumpadan F, Guallar E, Jebb A, Malamas P, Wu KC, Trayanova NA, Arrhythmia risk stratification of patients after myocardial infarction using personalized heart models, Nature communications 7 (1) (2016) 1–8.

[335]. Krummen DE, Ho G, Hoffmayer KS, Schweis FN, Baykaner T, Rogers A, Han FT, Hsu JC, Viswanathan MN, Wang PJ, et al. , Electrical substrate ablation for refractory ventricular fibrillation: Results of the AVATAR study, Circulation: Arrhythmia and Electrophysiology 14 (3) (2021) e008868. [PubMed: 33550811]

[336]. Hall K, Christini DJ, Tremblay M, Collins JJ, Glass L, Billette J, Dynamic control of cardiac alternans, Physical Review Letters 78 (23) (1997) 4518.

[337]. Hall GM, Gauthier DJ, Experimental control of cardiac muscle alternans, Physical Review Letters 88 (19) (2002) 198102. [PubMed: 12005667]

[338]. Landaw J, Qu Z, Control of voltage-driven instabilities in cardiac myocytes with memory, Chaos: An Interdisciplinary Journal of Nonlinear Science 28 (11) (2018) 113122.

[339]. Jordan PN, Christini DJ, Adaptive diastolic interval control of cardiac action potential duration alternans, Journal of cardiovascular electrophysiology 15 (10) (2004) 1177–1185. [PubMed: 15485444]

[340]. Wu R, Patwardhan A, Restitution of action potential duration during sequential changes in diastolic intervals shows multimodal behavior, Circulation research 94 (5) (2004) 634–641. [PubMed: 14752029]

[341]. Cherry EM, Distinguishing mechanisms for alternans in cardiac cells using constant-diastolic-interval pacing, Chaos: An Interdisciplinary Journal of Nonlinear Science 27 (9) (2017) 093902.

[342]. Zlochiver S, Johnson C, Tolkacheva E, Constant DI pacing suppresses cardiac alternans formation in numerical cable models, Chaos: An Interdisciplinary Journal of Nonlinear Science 27 (9) (2017) 093903.

[343]. Echebarria B, Karma A, Spatiotemporal control of cardiac alternans, Chaos: An Interdisciplinary Journal of Nonlinear Science 12 (3) (2002) 923–930.

[344]. Rappel W-J, Fenton F, Karma A, Spatiotemporal control of wave instabilities in cardiac tissue, Physical review letters 83 (2) (1999) 456.

[345]. Merchant FM, Sayadi O, Sohn K, Weiss EH, Puppala D, Doddamani R, Singh JP, Heist EK, Owen C, Kulkarni K, et al. , Real-time closed-loop suppression of repolarization alternans reduces arrhythmia susceptibility in vivo, Circulation: Arrhythmia and Electrophysiology 13 (6) (2020) e008186. [PubMed: 32434448]

[346]. Sommer P, Kircher S, Rolf S, John S, Arya A, Dinov B, Richter S, Bollmann A, Hindricks G, Successful repeat catheter ablation of recurrent longstanding persistent atrial fibrillation with rotor elimination as the procedural endpoint: a case series, Journal of cardiovascular electrophysiology 27 (3) (2016) 274–280. [PubMed: 26527103]

[347]. Clayton R, Murray A, Higham P, Campbell R, Self-terminating ventricular tachyarrhythmias - a diagnostic dilemma?, The Lancet 341 (8837) (1993) 93–95.

[348]. Chen P-S, Wu T-J, Ting C-T, Karagueuzian HS, Garfinkel A, Lin S-F, Weiss JN, A tale of two fibrillations, Circulation 108 (19) (2003) 2298–2303. [PubMed: 14609997]

[349]. Konishi S, Minamiguchi H, Masuda M, Ashihara T, Okuyama Y, Ohtani T, Sakata Y, Self-terminated long-lasting ventricular fibrillation: What is the mechanism?, Journal of cardiology cases 10 (4) (2014) 136–139. [PubMed: 30534225]

[350]. Lilienkamp T, Parlitz U, Terminal transient phase of chaotic transients, Physical review letters 120 (9) (2018) 094101. [PubMed: 29547310]

[351]. Lilienkamp T, Parlitz U, Terminating transient chaos in spatially extended systems, Chaos: An Interdisciplinary Journal of Nonlinear Science 30 (5) (2020) 051108.

[352]. Coullet P, Gil L, Lega J, Defect-mediated turbulence, Physical Review Letters 62 (14) (1989) 1619. [PubMed: 10039721]

[353]. Rehberg I, Rasenat S, Steinberg V, Traveling waves and defect-initiated turbulence in electrocon-vecting nematics, Physical Review Letters 62 (7) (1989) 756. [PubMed: 10040325]

[354]. Ecke RE, Hu Y, Mainieri R, Ahlers G, Excitation of spirals and chiral symmetry breaking in Rayleigh-Bénard convection, Science 269 (5231) (1995) 1704–1707. [PubMed: 17821641]

[355]. Hildebrand M, Bär M, Eiswirth M, Statistics of topological defects and spatiotemporal chaos in a reaction-diffusion system, Physical Review Letters 75 (8) (1995) 1503. [PubMed: 10060314]

[356]. Ouyang Q, Flesselles J-M, Transition from spirals to defect turbulence driven by a convective instability, Nature 379 (6561) (1996) 143.

[357]. Egolf DA, Melnikov IV, Pesch W, Ecke RE, Mechanisms of extensive spatiotemporal chaos in Rayleigh–Bénard convection, Nature 404 (6779) (2000) 733–736. [PubMed: 10783880]

[358]. Daniels KE, Bodenschatz E, Defect turbulence in inclined layer convection, Physical Review Letters 88 (3) (2002) 034501. [PubMed: 11801064]

[359]. Varela H, Beta C, Bonnefont A, Krischer K, Transitions to electrochemical turbulence, Physical Review Letters 94 (17) (2005) 174104. [PubMed: 15904297]

[360]. Beta C, Mikhailov AS, Rotermund HH, Ertl G, Defect-mediated turbulence in a catalytic surface reaction, EPL (Europhysics Letters) 75 (6) (2006) 868.

[361]. Rotter M, Dang L, Jacquemet V, Virag N, Kappenberger L, Haissaguerre M, Impact of varying ablation patterns in a simulation model of persistent atrial fibrillation, Pacing and clinical electrophysiology 30 (3) (2007) 314–321. [PubMed: 17367350]

[362]. Vidmar D, Rappel W-J, Extinction dynamics of spiral defect chaos, Physical Review E 99 (1) (2019) 012407. [PubMed: 30780268]

[363]. Dharmaprani D, Schopp M, Kuklik P, Chapman D, Lahiri A, Dykes L, Xiong F, Aguilar M, Strauss B, Mitchell L, et al. , Renewal theory as a universal quantitative framework to characterize phase singularity regeneration in mammalian cardiac fibrillation, Circulation: Arrhythmia and Electrophysiology 12 (12) (2019) e007569. [PubMed: 31813270]

[364]. Sinha S, Pande A, Pandit R, Defibrillation via the elimination of spiral turbulence in a model for ventricular fibrillation, Physical Review Letters 86 (2001) 3678. [PubMed: 11328052]

[365]. Qu Z, Critical mass hypothesis revisited: role of dynamical wave stability in spontaneous termination of cardiac fibrillation, American Journal of Physiology-Heart and Circulatory Physiology 290 (1) (2006) H255–H263. [PubMed: 16113075]

[366]. Dykman M, Mori E, Ross J, Hunt P, Large fluctuations and optimal paths in chemical kinetics, The Journal of chemical physics 100 (8) (1994) 5735–5750.

[367]. Assaf M, Meerson B, Extinction of metastable stochastic populations, Physical Review E 81 (2) (2010) 021116.

[368]. Newman M, Networks; an introduction, Oxford University, Oxford, 2010.

[369]. Gardiner C, Stochastic Methods: A Handbook for the Natural and Social Sciences, Springer-Verlag, Berlin Heidelberg, 2009.

[370]. Kubo R, Matsuo K, Kitahara K, Fluctuation and relaxation of macrovariables, Journal of Statistical Physics 9 (1) (1973) 51–96.

[371]. Garrey WE, The nature of fibrillary contraction of the heart.-Its relation to tissue mass and form, American Journal of Physiology–Legacy Content 33 (3) (1914) 397–414.

[372]. Byrd GD, Prasad SM, Ripplinger CM, Cassilly TR, Schuessler RB, Boineau JP, Damiano RJ Jr, Importance of geometry and refractory period in sustaining atrial fibrillation: testing the critical mass hypothesis, Circulation 112 (9_supplement) (2005) I–7.

[373]. Cox JL, Schuessler RB, D'Agostino HJ Jr, Stone CM, Chang B-C, Cain ME, Corr PB, Boineau JP, The surgical treatment of atrial fibrillation: III. Development of a definitive surgical procedure, The Journal of thoracic and cardiovascular surgery 101 (4) (1991) 569–583. [PubMed: 2008095]

[374]. Gaynor SL, Schuessler RB, Bailey MS, Ishii Y, Boineau JP, Gleva MJ, Cox JL, Damiano RJ Jr, Surgical treatment of atrial fibrillation: predictors of late recurrence, The Journal of thoracic and cardiovascular surgery 129 (1) (2005) 104–111. [PubMed: 15632831]

[375]. Gray RA, Pathmanathan P, Patient-specific cardiovascular computational modeling: diversity of personalization and challenges, Journal of cardiovascular translational research 11 (2) (2018) 80–88. [PubMed: 29512059]

[376]. Feeny AK, Chung MK, Madabhushi A, Attia ZI, Cikes M, Firouznia M, Friedman PA, Kalscheur MM, Kapa S, Narayan SM, et al. , Artificial intelligence and machine learning in arrhythmias and cardiac electrophysiology, Circulation: Arrhythmia and Electrophysiology 13 (8) (2020) e007952. [PubMed: 32628863]

[377]. Trayanova NA, Popescu DM, Shade JK, Machine learning in arrhythmia and electrophysiology, Circulation Research 128 (4) (2021) 544–566. [PubMed: 33600229]

[378]. Rogers AJ, Selvalingam A, Alhusseini MI, Krummen DE, Corrado C, Abuzaid F, Baykaner T, Meyer B, Clopton P, Giles W, et al. , Machine learned cellular phenotypes in cardiomyopathy predict sudden death, Circulation Research 128 (2) (2021) 172–184. [PubMed: 33167779]

[379]. Corral-Acero J, Margara F, Marciniak M, Rodero C, Loncaric F, Feng Y, Gilbert A, Fernandes JF, Bukhari HA, Wajdan A, et al. , The digital twino enable the vision of precision cardiology, European heart journal 41 (48) (2020) 4556–4564. [PubMed: 32128588]
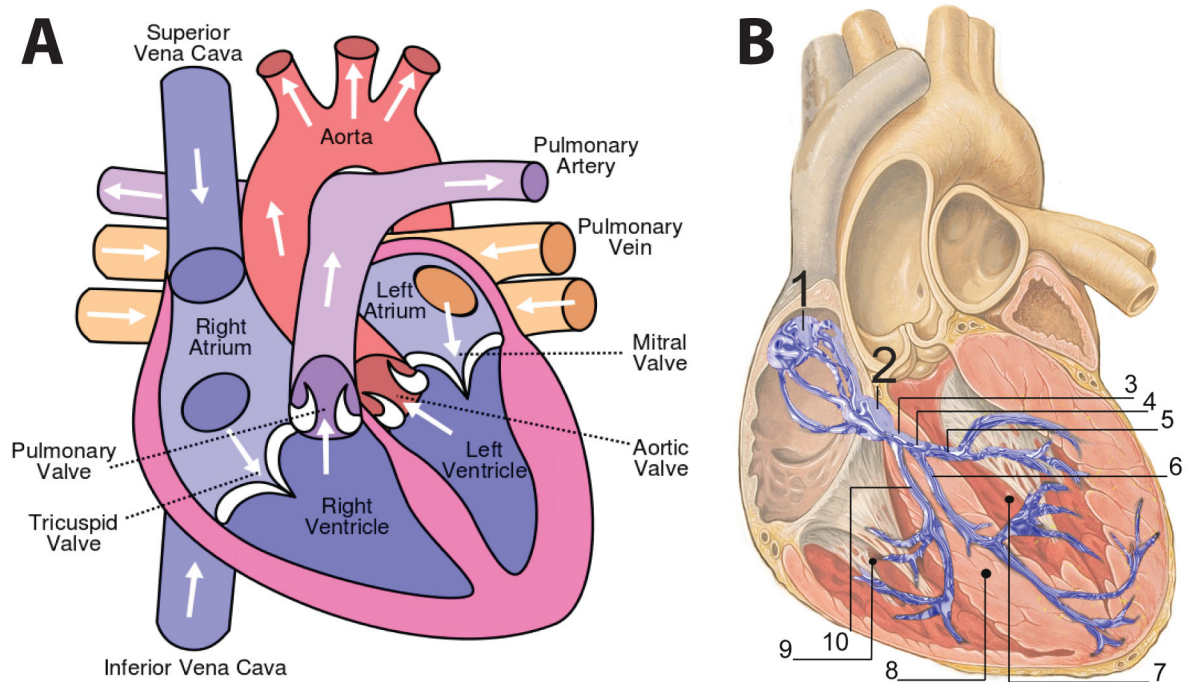
Figure 1:

Schematic representations of the heart. A. The relevant anatomical parts with arrows indicating direction of blood flow: deoxygenated blood enters the right atrium through the venae cavae and is pumped by the right ventricle to the lungs through the pulmonary artery. Oxygenated blood returns to the heart through the pulmonary veins and is circulated to the rest of the body through the aorta. B. Schematic representation of the electric system of the heart, shown here in blue. 1. Sinoatrial node 2. Atrioventricular node 3. Bundle of His 4. Left bundle branch 5. Left posterior fascicle 6. Left-anterior fascicle 7. Left ventricle 8. Ventricular septum 9. Right ventricle 10. Right bundle branch (By J. Heuser - self made, based upon Image:Heart anterior view coronal section.jpg by Patrick J. Lynch).
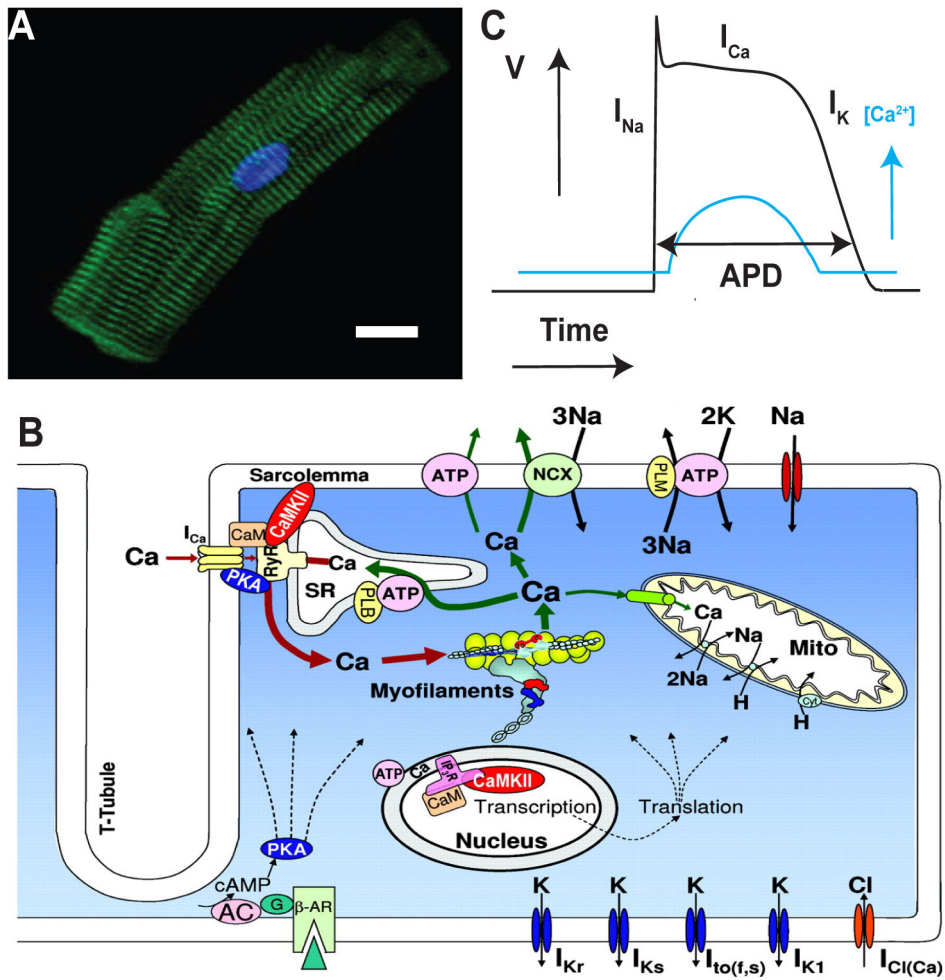
Figure 2:

Electrophysiology of a myocyte. A. Fluorescent image of a human cardiac myocyte where a-actinin is labeled in green and the nucleus is stained in blue. Scale bar: 10 μm. (From [24]). B. Schematic representation of a ventricular cardiac myocyte and some of its ion channels, ion transporters, signaling cascades, and structure. RyR indicates ryanodine receptors; SR, sarcoplasmic reticulum; Mito, mitochondria; CaMK, calcium-calmodulindependent protein kinase; NCX, Na/Ca exchanger; PLM, phospholemman; PLB, phospholamban; ATP, ATPase; PKA, protein kinase A; β-AR, β-adrenergic receptor; IKr, IKs, IK1, potassium channels; and ICl(Ca), a calcium-activated Cl current. (From [25]) C. Typical action potential shape, along with the most important currents during each phase of the action potential.
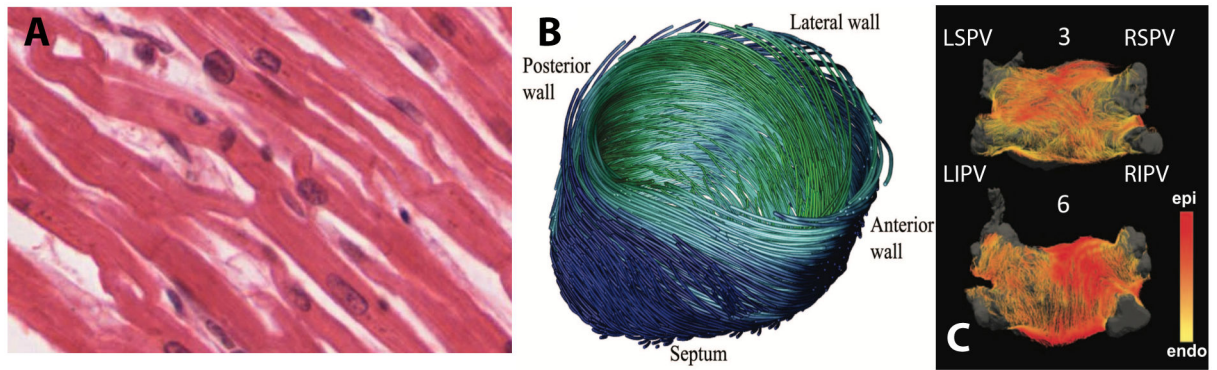
Figure 3:

Cell arrangement and fiber orientation in human hearts. A. A micrograph showing the orientation of cardiac myocytes in a slice of the ventricular right wall. The dark regions represent the nuclei of the cells and the cytoplasm is red (Regents of University of Michigan Medical School (§2012). B. Fiber orientation in the left ventricle of an *ex vivo* human heart obtained using DTMRI and a color coding representing the local fiber angle. Left-handed (right-handed) spiraling fibers are shown in blue (green) and darker values correspond to larger local angles. (From [43]). C. Fiber orientations in the LA in 2 different hearts, viewed posteriorly over the roof. The distance of the fiber relative to the endocardial shell is indicated using the color bar so that endocardial (epicardial) fibers are colored yellow (red). LIPV: left inferior pulmonary vein; LSPV: left superior pulmonary vein; RIPV: right inferior pulmonary vein; and RSPV: right superior pulmonary vein. (From [44]).
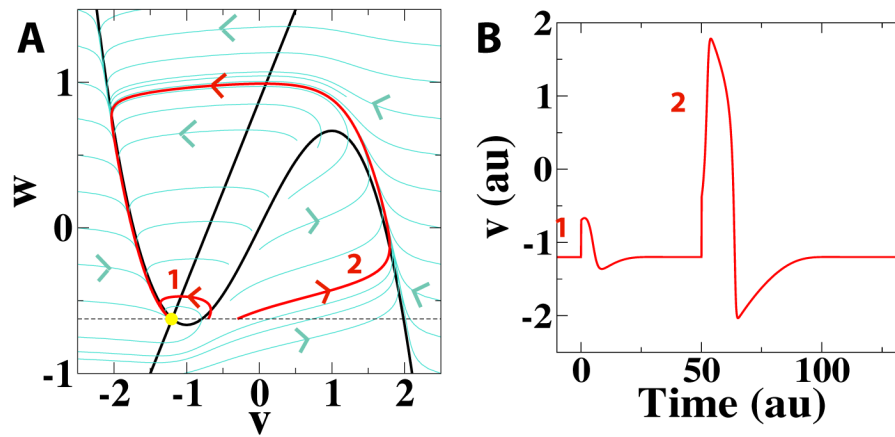
Figure 4:

The FHN model. A: Nullclines (black) of the FHN model, along with the the streamlines of the phase portrait and the equilibrium point (yellow dot). A small stimulus initiates the red decay trajectory, marked by 1, whereas a large stimulus initiates the red excitation trajectory, marked by 2. Parameter values of the model (see text): $\epsilon = 0.08$, a = 0.7, and b = 0.8, resulting in a fixed point located at $v = -1.2$ and $w = -0.625$. B: Time trace of the variable v corresponding to the trajectory #1 and #2 in A.
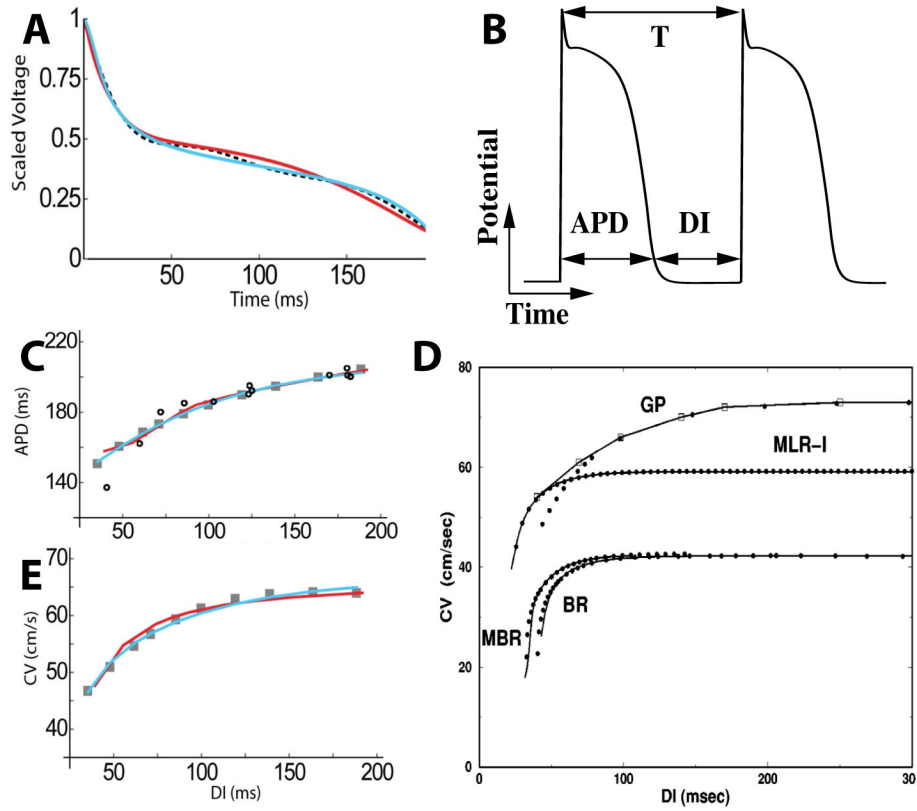
Figure 5:
Model fitting. A: Clinical AP morphology from an AF patient compared to model AP morphologies obtained by fitting the model parameters for an AF patient. The average clinical AP morphology is shown as a dashed line while the FK model is shown in blue and the KKT model is in red (From [73]). B: Schematic representation of a cardiac cell activated by stimuli with period *T*. As a result, the membrane potential increases rapidly, followed by a gradual return to the resting potential. The APD (action potential duration) measures the time at which the potential is above a certain threshold while the DI (diastolic interval) measures the time interval between the end of one and the start of another action potential. C: Clinically determined APD and its polynomial fit for an AF patient (open and closed symbols, respectively) and the results from a fitting procedure for the FK (blue) and KKT (red) model. D: CV restitution curves of several ionic models and of measurements in a guinea pig (solid lines) together with those obtained from the fitted FK model (From [70]). (BR: Beeler Reuter [76], MBR: modified Beeler Reuter with speed-up calcium, MLR-I: Luo-Rudy with speed-up calcium [77], GP: Guinea pig [78]). E: As in C, but now for the clinically determined CV restitution curve.
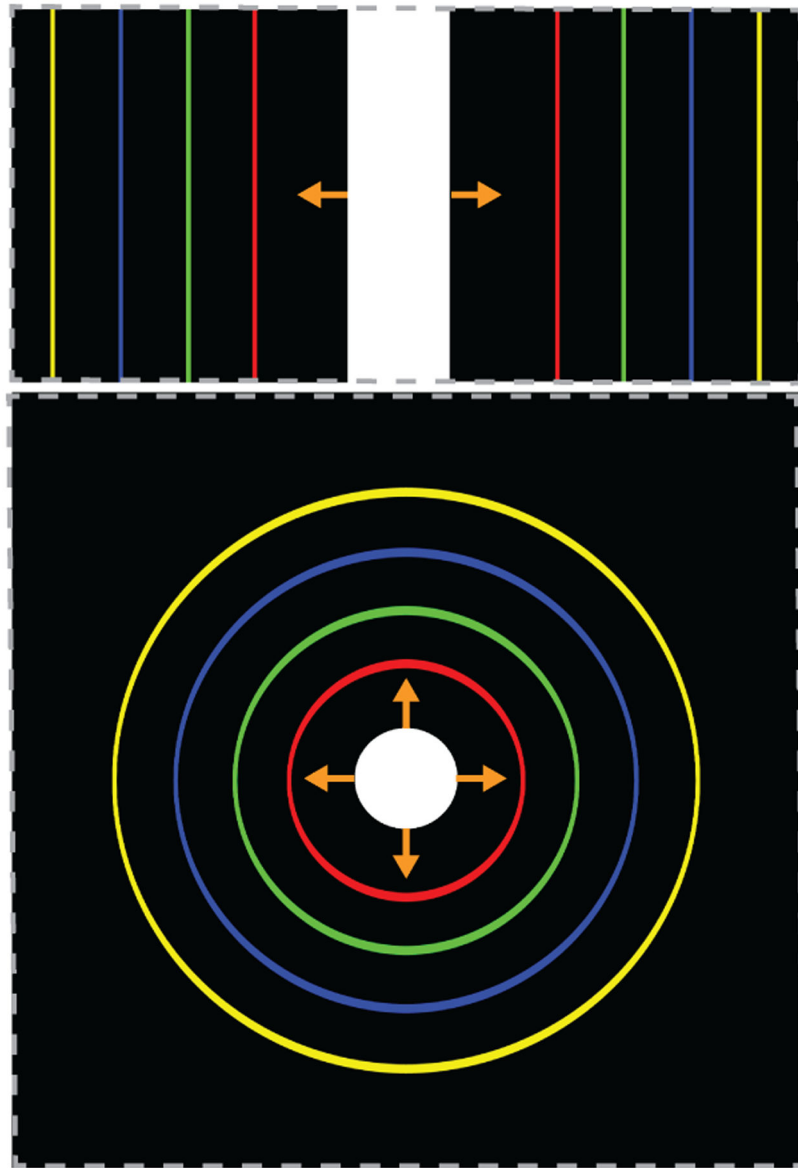
Figure 6:
Comparison of propagation speed for planar and curved fronts. A: Activation fronts plotted every 50ms following line stimulus in the middle of the rectangular domain using the FK model (parameter set #8) [87]. B: As in A, but now following a point stimulus. Due to the curvature of the wavefront, the propagation velocity is smaller than for the planar front in A.
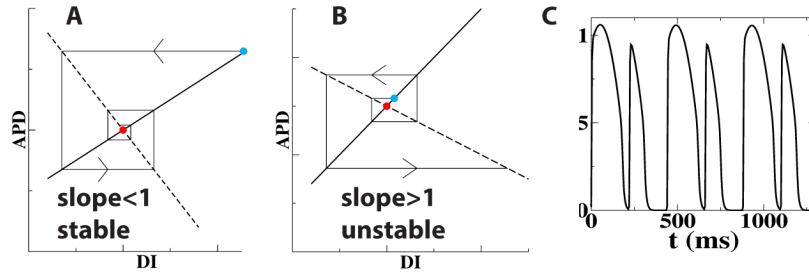
Figure 7:

Alternans in cardiac myocytes. A: Cobweb diagram illustrating a stable fixed point, shown in red, on a APD restitution curve with slope < 1. The dynamics of a small perturbation in *DI*, corresponding to the blue point, can be followed using the restitution curve $APD_{n+1} = f(DI_n)$ and the relationship $APD_n + DI_n = T$ (dashed line) and is shown to approach the fixed point, indicating stability. B: As in (C) but now for a restitution curve with a slope larger than 1. In this case, a point on the curve is unstable, as can be seen by following the path of the perturbation. C: Example of alternans in a single cell. Shown here is the response of the FK model (parameter set #4 from Ref. [87]) to periodic pacing with a period of 220 ms. The resulting APD oscillates between long and short.
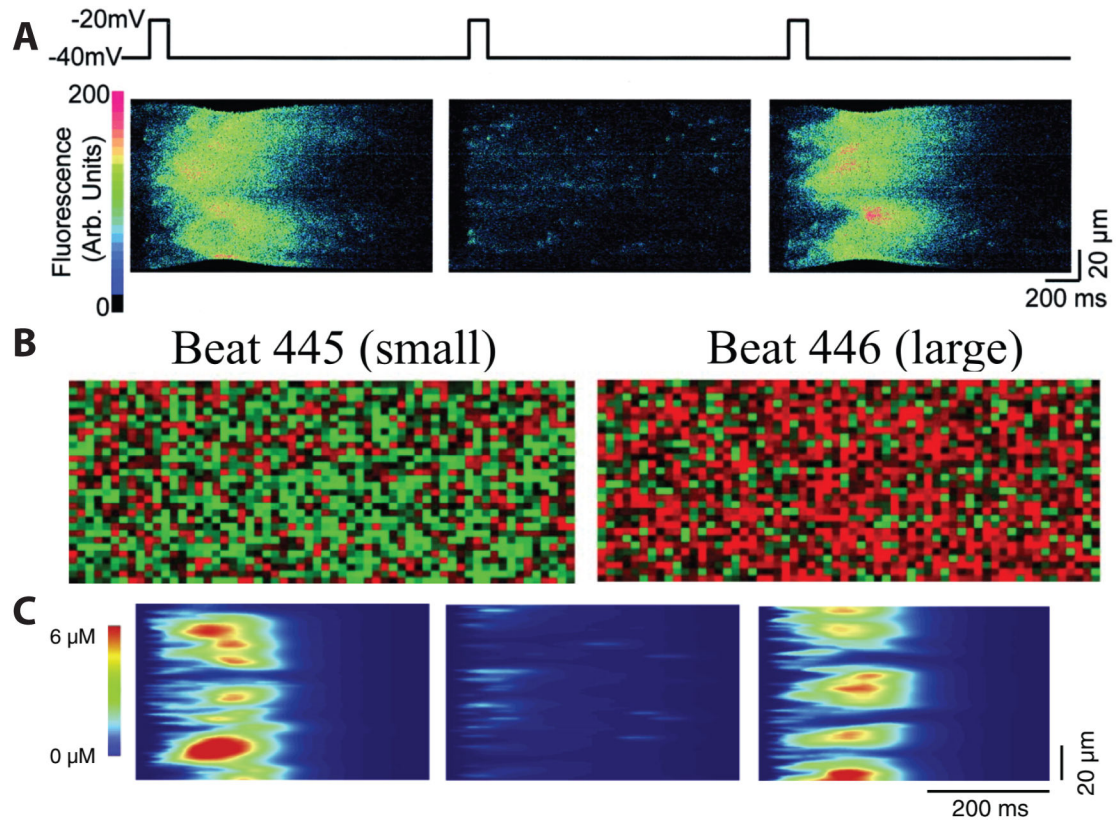
Figure 8:

Calcium alternans in experiments and simulations. A: Linescans in a rat ventricular myocyte in response to 3 consecutive voltage pulses, visualizing Ca^{2+} using a fluorescent indicator. From [147]. B: Normalized Ca^{2+} release in a 2D slice of a simulated cell, with green/red indicating minimal/maximal Ca^{2+} release. The pattern shows alternans, with a small release in beat 445 and a large release in beat 446. From [154]. C: A line scan plot of cytoplasmic Ca^{2+} from a simulation of coupled CRU networks, illustrating miniwaves during the release beats. From [148].
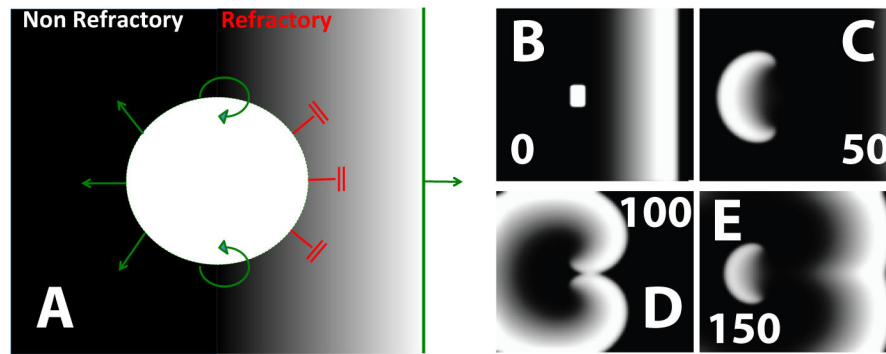
Figure 9:
Initiation of spiral waves using a premature stimulus. A: Schematic drawing of a stimulus (white circle) that follows a planar wave that propagated from left to right. Proper timing of this stimulus results in wave block to the right, indicated by the red symbol, but not to the left, as indicated by the green arrows. As the newly created wave propagates in the retrograde direction, tissue in the right-half of the domain continues to recover, eventually leading to reentry and spiral wave formation. B-E: Snapshots of a simulation showing the formation of a figure-of-eight reentry pattern as the result of a properly timed extra stimulus. Panel B shows the premature stimulus along with the planar wave propagating from left to right. Panel C demonstrates that only propagation in the retrograde direction is possible while panel D illustrates the ensuing reentry into the recovered tissue. Panel E shows the figure-of-eight reentry pattern. Snapshots were created using the FK model and numbers correspond to time in ms.
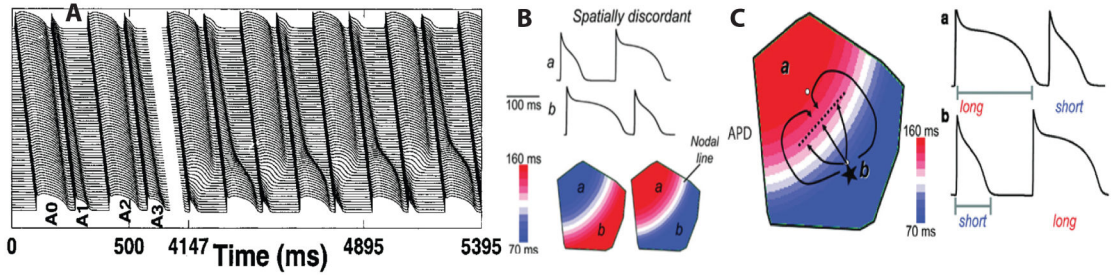
Figure 10:

Alternans in spatially extended domains. A: Initiation of discordant alternans in an 8 cm long computational cable using the Beeler-Reuter model (vertical axis denotes space and horizontal axis denotes time). All stimuli were applied at the top end of the cable, using constant 310 ms intervals. After multiple stimuli, the top and bottom of the cable are alternating out of phase. From [175]. B: Spatially discordant APD alternans in simulated 2D cardiac tissue using the Luo-Rudy model and a pacing cycle of 220 ms. The top panel displays the action potential at sites a and b, showing a long-short pattern. The lower panel shows that the spatial APD distribution, color-coded with blue for short and red for long, for two consecutive beats. The white line represents the nodal line, which separates the out of phase domains and where alternans is absent. C: Sequence of events following a premature ectopic beat (asterisk) that can result in reentry. The beat is initially blocked when it attempts to propagate into the region with long APD. It can reenter this region, however, after it has propagated along the nodal line, resulting in a figure-eight re-entry. B&C from [173].
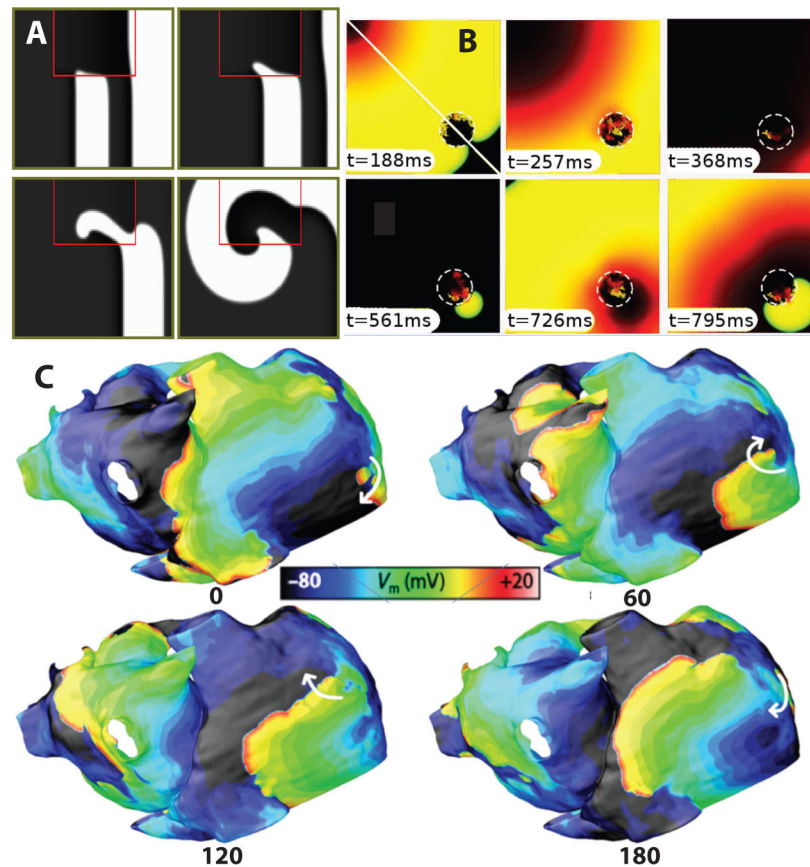
Figure 11:
Examples of wave breakup in models with heterogeneities. A: Snapshots showing successive times in a simulation of the FHN in a domain that contains which a heterogeneous zone of refractoriness, indicated by the red lines. Due the heterogeneity, the wave is originally blocked but then reenters the heterogeneous zone, after which a spiral wave is formed. After [180]. B: Reentry by interaction of an activation wave with a circular and fibrotic region in a computational model using the modified Beeler-Reuter model. Total area 77 cm^2. From [186]. C: Initiation of reentry in a patient-specific model shown in 4 snapshots, 60ms apart. Reentry is shown using white arrows and is due to fibrosis in that region. From [187].
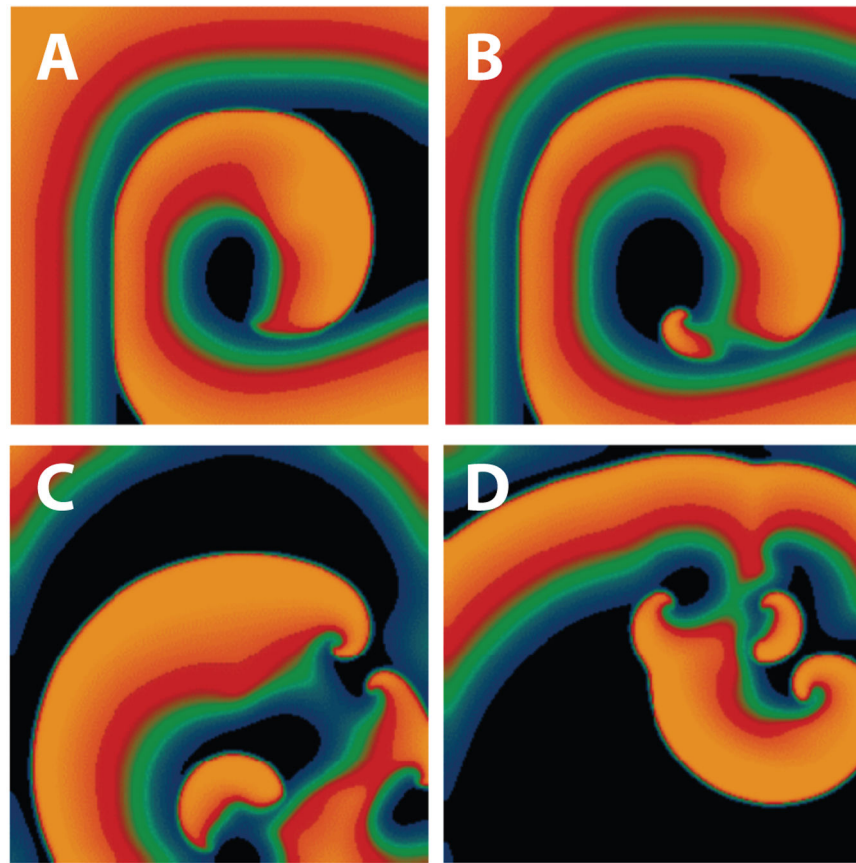
Figure 12:
Spiral wave breakup. A-D: Snapshot of a simulation of the FK model in which a spiral wave breaks up due to the Doppler shift that is induced by the meandering tip. This shift results in wave block (B) and spiral wave breakup (C-D). The voltage is displayed using a color map with orange/black corresponding to polarized/depolarized tissue, respectively. From [87].
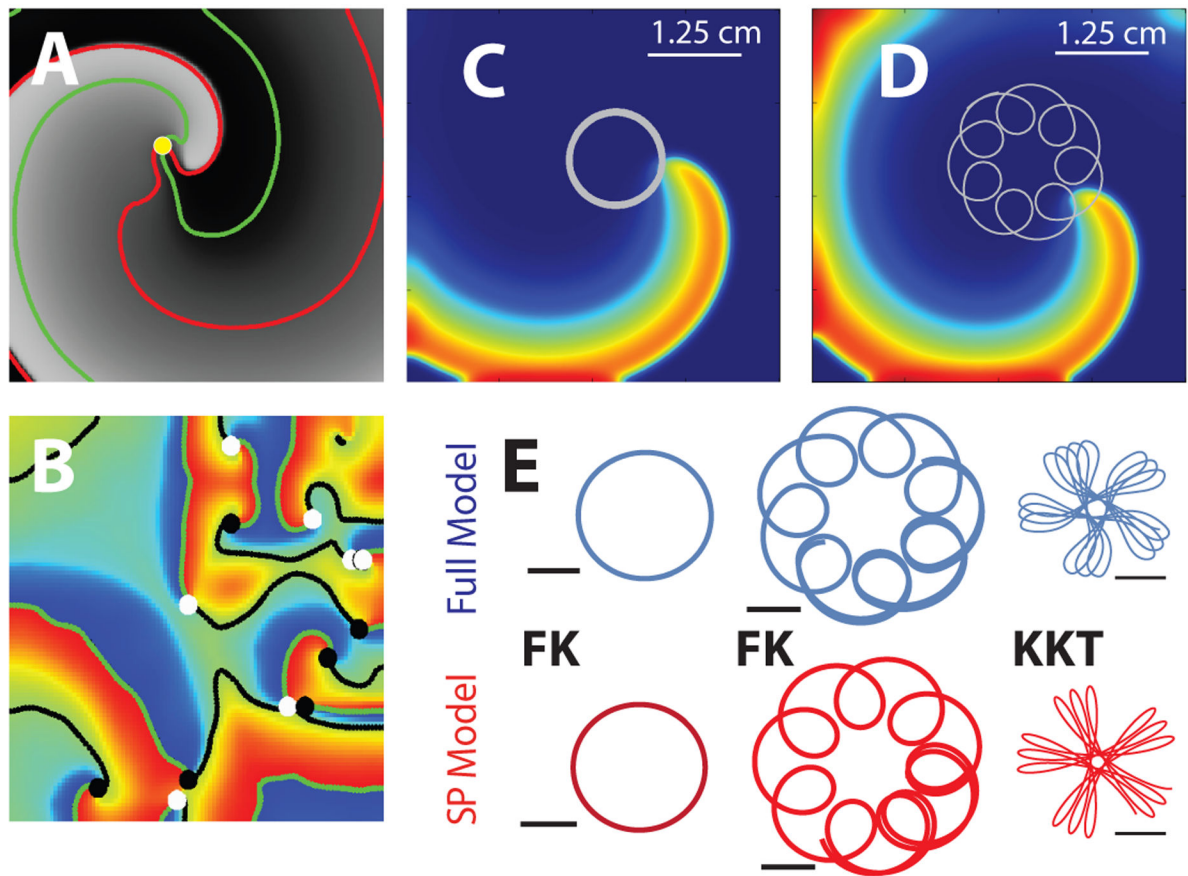
Figure 13:

Spiral tip dynamics A: Snapshot of a simulation of a single spiral with the voltage shown using a gray scale with white (black) corresponding to depolarized (repolarized) tissue. The intersection of the red and green lines is marked by a yellow dot and represents a phase singularity and can be identified as the spiral wave tip. B: Example of spiral wave breakup in a simulation, with voltage shown using a color scale, activation fronts shown as green line, recovery lines shown as black lines, tips of clockwise rotating spiral waves as black dots and tips of counter clockwise rotating spiral waves as white dots. C&D: Snapshots of counterclockwise rotating spiral waves for two different parameter sets of the FK model. In these snapshots, the voltage is color-coded with red corresponding to high and low corresponding to low values, and the tip trajectory is shown in white. E: Comparison of tip trajectories obtained using the full models (upper row) and the single particle model (lower row). The left and middle column correspond to the trajectories from the FK model shown in C&D while the right column corresponds to a tip trajectory from the KKT model. Scale bars are 0.5 cm. From [221].
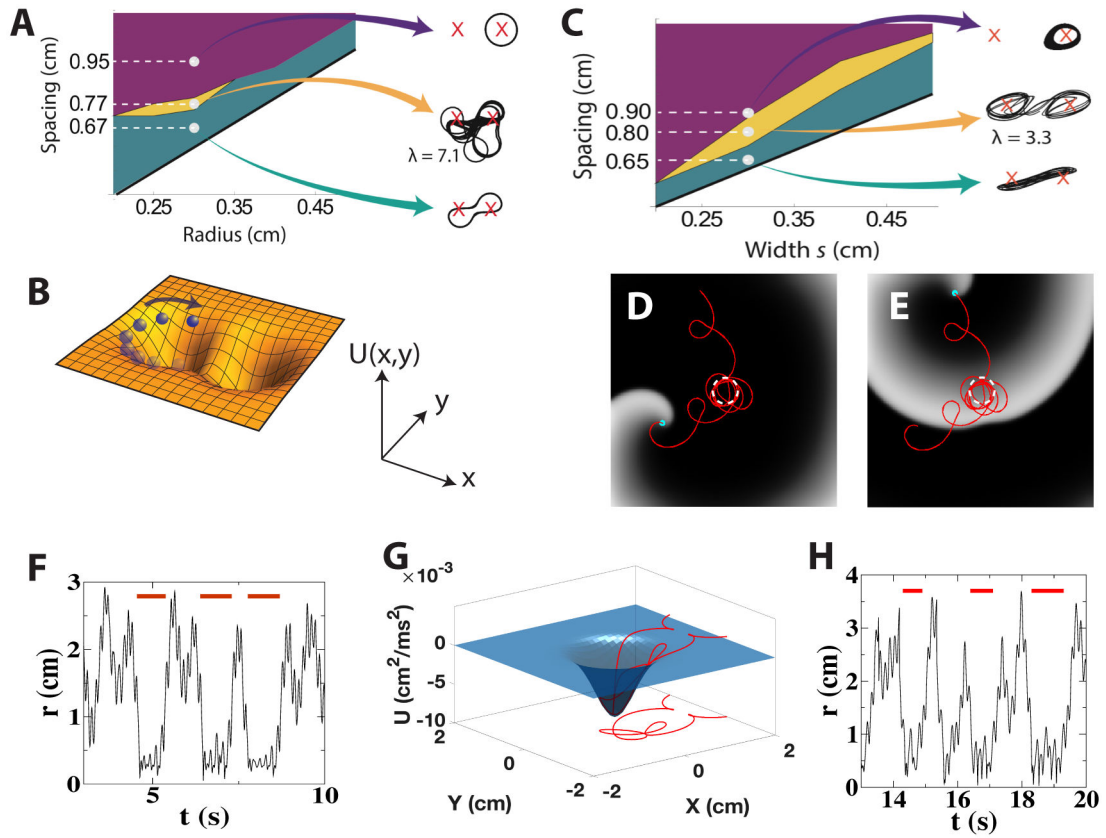
Figure 14:

Complex spiral tip dynamics. A: Phase diagram of the spiral wave dynamics in the FK model in the presence of two identical heterogeneities. Representative tip trajectories, corresponding to the three dots, are shown as black lines, with the location of the heterogeneities indicated as red crosses. The tip dynamics in the yellow region has a positive Lyapunov exponent ($\lambda = 7.1$) and is thus chaotic. B: Schematic representation of a particle moving in a potential landscape with two wells, representing tissue heterogeneities. C: Phase diagram of the single particle model in the presence of the potential landscape shown in panel B. The phase diagram is qualitatively similar to the one of the full model, presented in panel A. D-E: Snapshots of a simulation of the FK model in the presence of a circular heterogeneity with a radius of 0.275 cm, plotted by the dashed white line. Snapshot D represents the start of the simulation interval while snapshot E represents its end. The trajectory of the spiral tip (cyan dot) is plotted in red and shows that the spiral wave is temporarily trapped by the heterogeneity. F: Distance r from the tip to the center of the heterogeneity as a function of time. Trapped intervals are indicated by the red bars. G: Trajectory of an intermittently trapped particle, moving on a potential surface with a single well. H: Distance r of the particle to the minimum of the potential well as a function of time. Trapped intervals during are indicated by the red bars. Panel A-C from [221]; panel D-H from [228].
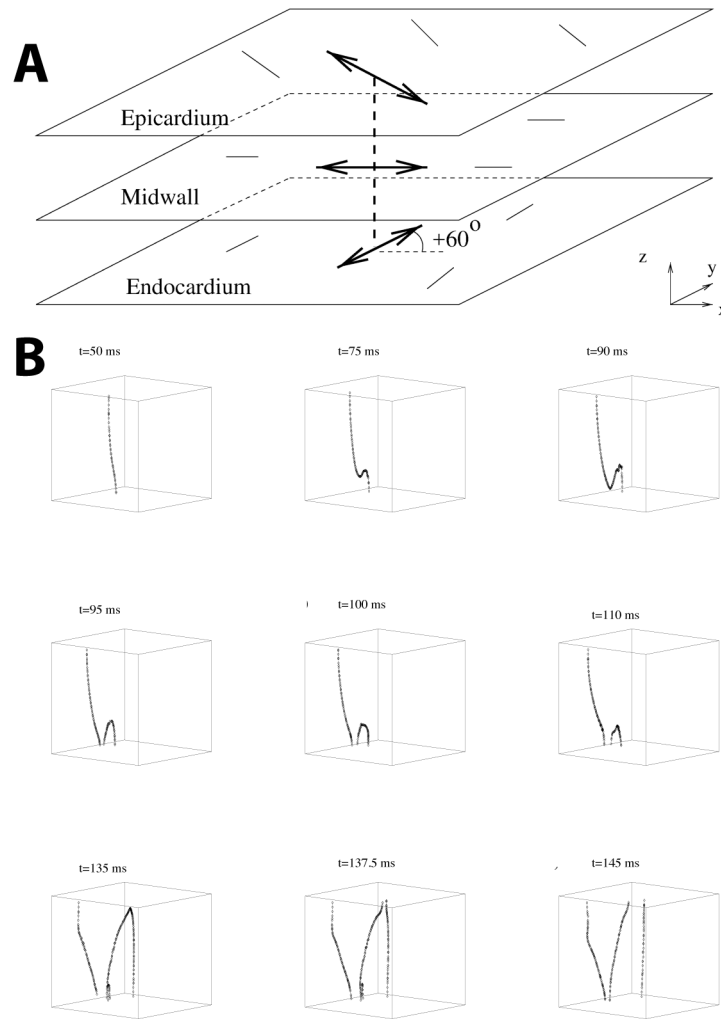
Figure 15:

Filament stability and fiber twist. A: Simplified three-dimensional wedge geometry with rotating anisotropy. B: Break up of filaments for a slab of dimension 5cmxcm and with a thickness of 0.9 cm. The rotation rate in this simulation was taken to be 12 °/mm. From [88].
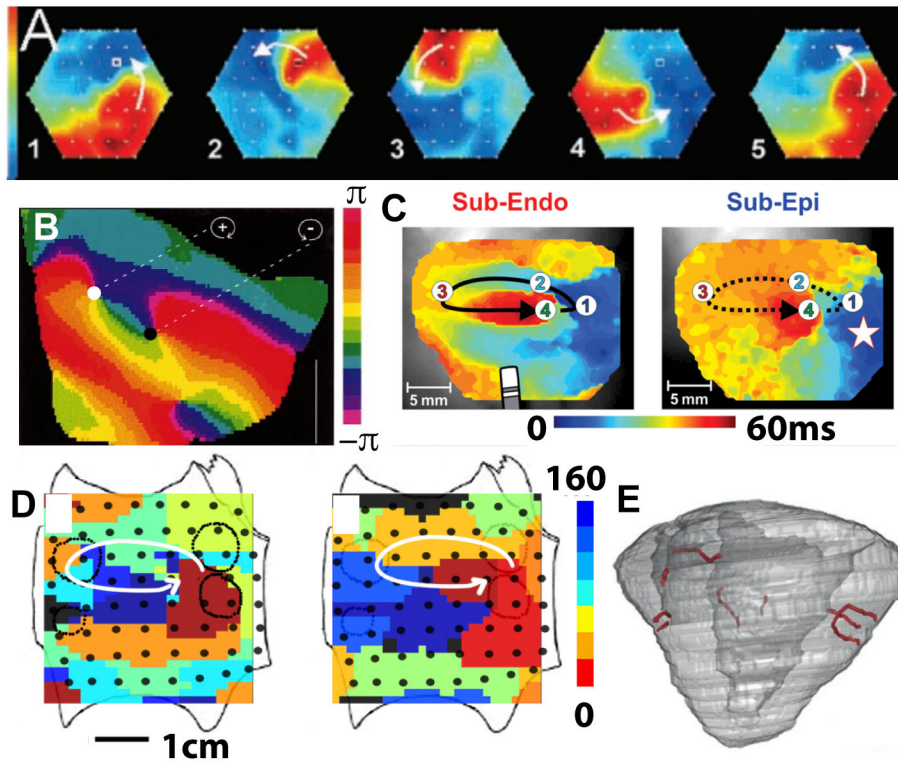
Figure 16:

Experimental and clinical mapping of spiral wave patterns. A: Voltage sensitive dye recordings of reentry in in a cultured monolayer of neonatal rat cardiac cells. The colors indicate the normalized voltage level, with blue being the resting state (0%) and red the peak action potential (100%). From [260]. One full rotation of the reentry is illustrated, with frames 20 ms apart. B: Snapshot of the phase map on a rabbit heart surface during sustained fibrillation, obtained using a voltage sensitive dye. The phase map reveals two counter-rotating spiral waves, indicated by the white and black dots. From [213]. C: Activation maps during sustained atrial fibrillation in the RA of a human explanted heart, recorded using a voltage sensitive dye. The activation is simultaneously measured on the endo- and epicardial surface and reveals a reentry pathway on both surfaces. From [261]. D: Isochronal maps of the LA, separated by 237 days and obtained using a basket electrode, demonstrate temporal conservation of a spiral wave in human AF. Time in ms. Targeted ablation at the spiral tip eliminated AF. From [262]. E: Mechanical filaments (red) inside pig ventricles (grey shaded) between endocardial (endo) and epicardial (epi) heart surface during ventricular fibrillation imaged using 4D ultrasound. From [263].
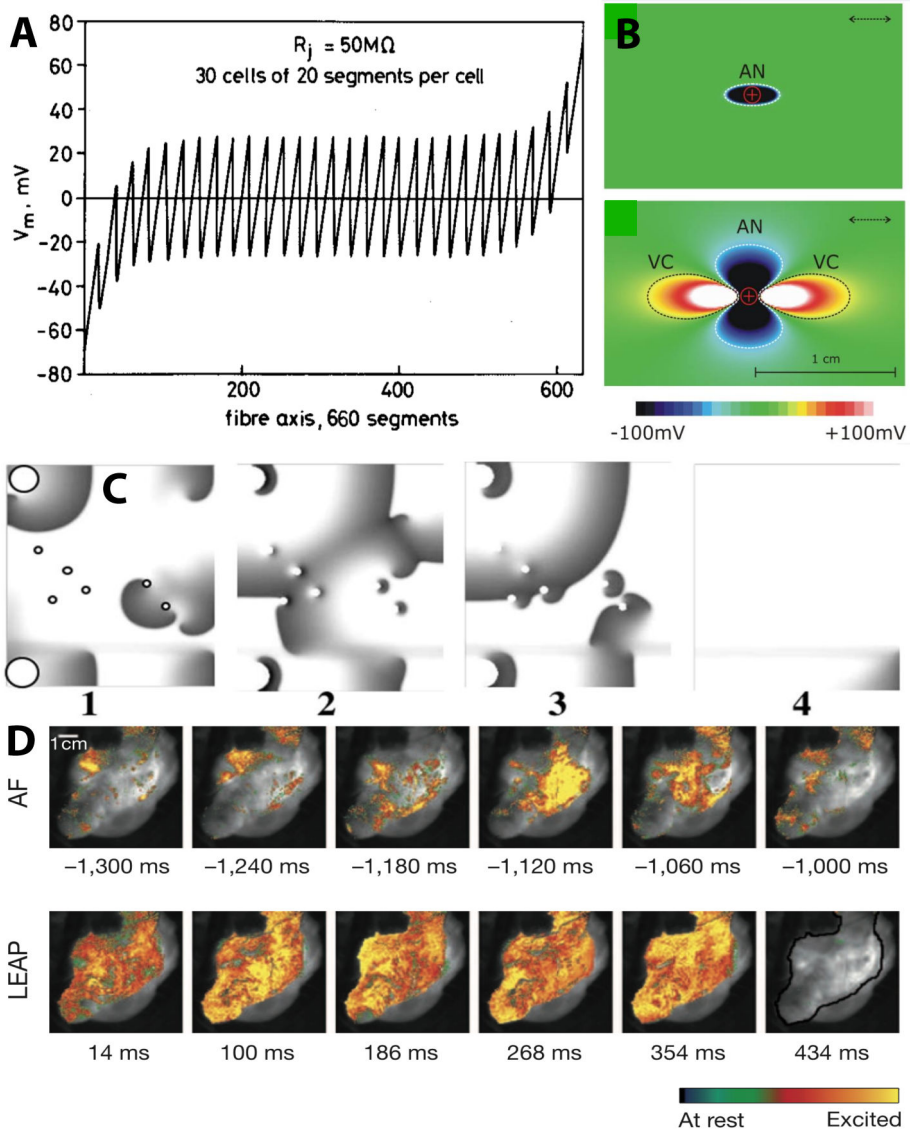
Figure 17:
Low-energy defibrillation. A: Sawtooth potential in a simulation of a strand of 30 cells and an intracellular junction resistance of 50 MΩ (From [290]). B: Upper panel: Unipolar anodal stimulation at the center of a thin computational sheet with equal intra- and extracellular anisotropy ratios. In this case, the changes in V_m have identical sign, with a shape that is given by the the fiber orientation (taken here to be along the horizontal direction, as indicated by the arrow). Lower panel: Identical stimulus but now with unequal intra- and extracellular anisotropy ratio. Changes in V_m are both positive and negative, with tear-drop shaped regions of depolarization (called virtual cathodes). (From [122].) C: Example of termination of spiral waves by wave emission from heterogeneities in a simulation using the Luo-Rudy model. Electric field pulses initiated waves from the obstacles, resulting in the termination of the rotating waves. (From [303].) D: Snapshots of the electrical activation of a dog's atrium, visualized using optical mapping, during low-energy defibrillation (From [304]). The upper row visualizes AF while the lower row corresponds to the activation

maps after each low energy pulse (LEAP). The last panel shows the removal of fibrillation, resulting in tissue that is at rest.
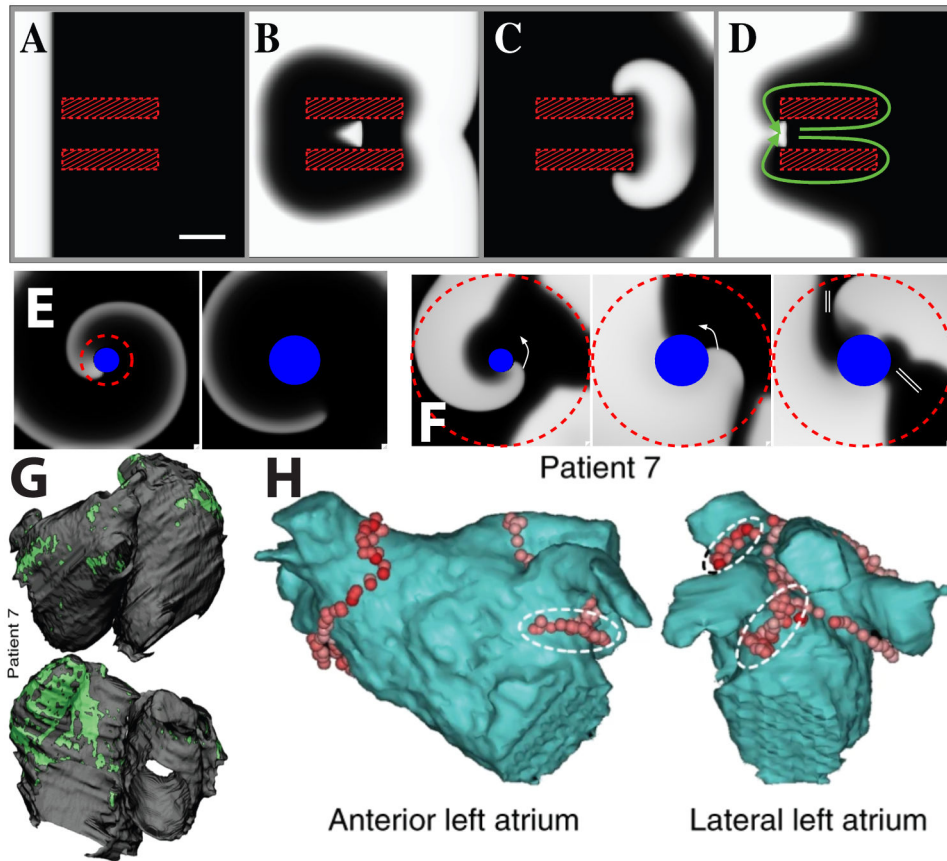
Figure 18:

Modeling ablation of fibrillation. A-F: Examples of ablation mechanisms that lead to acute termination of atrial fibrillation (Adapted from [316]). In (AD), a slow-conducting zone is sandwiched between nonconducting regions (hatches). The resulting figure-of-eight reentry can be abruptly terminated by ablating the slow-conducting isthmus. E: Simulation of termination in a high excitability region, indicated by the dashed circle, that is surrounded by low excitability tissue. The excitability is a linear function of the radial direction. Before ablation (left panel), a wave is attached to a circular obstacle. After ablation, the wavefront finds itself in a region of low excitability, detaches from the obstacle, and migrates towards the edge of the computational domain, resulting in the termination of reentry (right panel). F: Simulation of termination in a region of low excitability. Within the dashed circle, the tissue excitability is a linear function of the radius and is lowest at the obstacle. Before ablation, a counter clockwise rotating activation front is attached to a nonconducting zone (left panel). After ablation (middle and left panels), the wavefront encounters the wave back, resulting in block (double bars in right panel). The wavefront detaches from the ablation lesion and terminates. Scale bars, 1 cm. (G-H) Targeted ablation based on fibrotic tissue regions (From [211]). (G) Posterior (top) and anterior (bottom) views of a patient-specific atrial mode as reconstructed from segmented LGE-MRI scans, including the distribution of fibrotic tissue shown in green. (H) Sites of ablation delivery shown as red dots in the left atrium of the patient in (G). The dashed ellipse indicates the locations ablated based on the locations of persistent reentry circuits, identified by computational analysis.
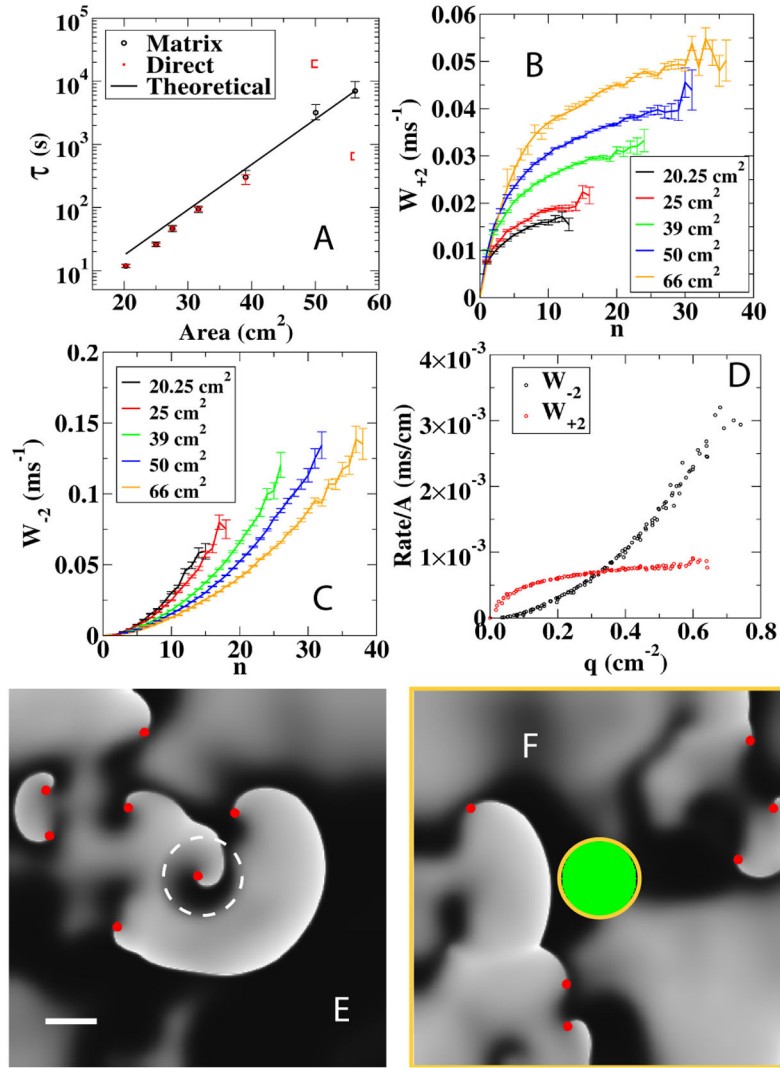
Figure 19:

Termination statistics in cardiac models. A: Termination times as a function of the system size for the FK model with periodic boundary conditions plotted as red symbols. Also shown are the results from the master equation approach (black symbols) and from the closed-form expression obtained using the WKB analysis (solid line). B&C: Transition rates for the FK model computed using direct simulations with periodic boundary conditions. Shown are the birth and death rates for $n \rightarrow n + 2$ (B) and $n \rightarrow n - 2$ (C) computed in a square geometry of various sizes. Error bars represent standard deviation of the mean value. D: The $W_{\pm 2}$ rates, normalized by the area of the domain, as a function of the density of tips. The rates collapse onto a single curve for all computational domain sizes. E: Simulation of spiral wave break up in a 7.5cmx7.5cm domain. The potential is shown using a gray scale and spiral wave tips are indicated by red symbols. The central portion, with radius 0.75 cm, inside the white circle has reduced excitability, which results in a stable spiral wave source. Scale bar: 1cm. F: Snapshot of the activation pattern after the ablation of the heterogeneous circular region in A. The virtual ablation lesion, shown in green, results in the removal of the spiral wave

from the central region. All non-conducting boundaries are shown as orange lines. Panels
A-D from [362], Panels E&F from [314].

Table 1:

Commonly used abbreviations in this review.

LV	Left ventricle	AF	Atrial fibrillation
RV	Right ventricle	VF	Ventricular fibrillation
VT	Ventricular tachycardia	LA	Left atrium
RA	Right atrium	AT	Atrial tachycardia
AP	Action potential	APD	Action potential duration
CV	Conduction velocity	DI	Diastolic interval
AV	Atrioventricular	RyR	Ryanodine receptor
CRU	Calcium release unit	SR	Sarcoplasmic reticulum
CICR	Calcium induced calcium release	LCC	voltage-gate L-type Ca^{2+} channel

Table 2:

Relevant physiological parameters of the human heart. The anatomical parts are illustrated in Fig. 1.

Mass	250-300 g (female); 300-350 grams (male) [14]
Conduction velocity atria	0.5 m/s [6]
Conduction velocity AV node	0.05 m/s [6]
Conduction velocity His bundle	1.5 m/s [15]
Conduction velocity Purkinje fibers	1.5 m/s [6]
Conduction velocity ventricles	0.5 m/s [6]
Ventricular wall thickness	1-2 mm (apex) 12-15 mm (base) [16]
Atrial wall thickness	1-4 mm [17]
Myocyte size	120 μm (length) 20-30 μm (diameter) [16]